DIFFERENTIAL MICRORNA REGULATION BY PDE5 AND PDE9 IN THE HEART AND THEIR INTRA-MYOCYTE COMPARTMENTATION

by

Kristen Kokkonen-Simon

A dissertation submitted to Johns Hopkins University in conformity with the requirements

for the degree of Doctor of Philosophy.

Baltimore, Maryland

March, 2019

ABSTRACT

Protein kinase G (PKG) activation is protective in various cardiovascular diseases, including ischemia, hypertrophy, and heart failure. PKG is activated by cyclic guanosine monophosphate (cGMP), which is produced by guanylyl cyclases and degraded by phosphodiesterases (PDEs). In the heart, there are two cGMP-selective PDEs, PDE5 and PDE9. Inhibition of either PDE is protective in a mouse pressure-overload-induced model of cardiac hypertrophy and failure, improving function and decreasing maladaptive remodeling and pathological molecular signaling. However, despite these similarities, there is still much to be understood about the differential signaling afforded by these two enzymes, including their effects on transcriptional regulation and nano-compartment protein partnering.

This thesis reports two primary studies. The first study tested the hypothesis that microRNA and mRNA regulation by PDE5 and PDE9 reveals different transcriptomic signatures reflecting their nanodomain control of cGMP. To examine this, mRNA and miRNA sequencing was performed on myocardium from mice subjected to pressure-overload and treated with either a PDE5 or PDE9 inhibitor. Inhibition of either PDE significantly altered mRNA transcription, with similar pathways engaged by each treatment. By contrast, each inhibitor had a dramatically different impact on miRNA expression. PDE5 inhibition broadly reduced miRNA expression, while PDE9 inhibition had essentially no impact on miRNAs relative to pressure-overload. Notably, even if a similar stimulation pathway was engaged, as between PDE5 inhibition and sGC activation, the miRNA results were not fully replicative.

The second study examined where PDE5 and PDE9 reside in the cardiomyocyte, specifically identifying interacting proteins in their nanodomains through two approaches. In the first approach, I performed co-immunoprecipitation of PDE9 followed by mass spectrometry. This revealed a cluster of proteins bound to PDE9, including many in the mitochondrial membrane and a number of sarcoplasmic reticular proteins, which were largely unchanged under pro-hypertrophic growth conditions. The second approach utilized APEX2-PDE fusion proteins. Upon H_2O_2 stimulation, APEX2 biotinylates neighboring proteins, which can be pulled down and subjected to mass spectrometry. APEX2-tagged PDE constructs were verified and optimized, yet mass spectrometry analysis failed to identify biotinylated proteins. Ongoing efforts are re-examining these spectra to improve identification of proteins selectively biotinylated by PDE5 and PDE9.

Advisor: David Kass, MD

Reader: Brian O'Rourke, PhD

ACKNOWLEDGMENTS

I would first and foremost like to thank my advisor, Dr. David Kass. Without his support and mentorship over the past 5 years, I would never have become the scientist that I am now. From the day I first approached him about a rotation, he has been honest and insightful, always telling me his thoughts and giving advice on both science and life. I would also like to thank my committee members: Brian O'Rourke, Mark Anderson, and Brian Foster, as well as Jin Zhang and Ryuya Fukunaga (former committee members). I am grateful for their insight, as well as for David and Jin coming back to rescue me from the Dali Museum before the GRC bus left without me.

I would next like to express my gratitude to my lab mates both past and present in the Kass lab including: Grace Kim, Brian Lin, Brittany Dunkerly-Eyring, Dong Lee, Sumita Mishra, Christian Oeing, Virginia Hahn, Jonathan Kirk, Taishi Nakamura, and Steve Hsu. In particular I would like to thank Mark Ranek, who mentored me when I was a rotation student and is still someone from whom I frequently seek advice.

I would furthermore like to thank the Cellular and Molecular Medicine graduate program, without whom I would not be here at all. I particularly would like to acknowledge Colleen Graham and Leslie Lichter for their support over my years in the CMM program.

Finally, I would like to thank my family. I am immensely grateful to my parents for always encouraging me to pursue my passions, and supporting me every step of the way. And of course, I don't know what I would have done without my husband, Ben Simon, who tolerated many hours of scientific talk that was meaningless to him, and encouraged me whenever I felt frustrated or defeated.

The work in this dissertation was supported in part by a Ruth L. Kirschstein National Research Service Award Individual Predoctoral Fellowship from the National Lung, Heart, Blood and Lung Institute (F31-HL134196).

TABLE OF CONTENTS

PAGE

LIST OF TABLES

LIST OF FIGURES

PAGE

LIST OF FIGURES

CHAPTER 1: Introduction

Phosphodiesterases (PDEs) are members of an enzyme superfamily that hydrolyze cyclic adenosine or guanosine 3′,5′-monophosphate (cAMP or cGMP, respectively). In so doing, they provide finely tuned and localized regulation of these second messengers to control their roles in cell signaling. Since the discovery of PDEs just over half a century ago, research has uncovered a multiplicity of subgroups and isoforms, the diverse roles played by these enzymes, and the therapeutic value that can be gleaned by their selective inhibition. Some inhibitors are used widely to treat diseases such as pulmonary hypertension and erectile dysfunction, but others are being investigated actively with resurgent interest in their biology and regulation. Beyond well-recognized differences among the primary members of the PDE superfamily, recent studies have revealed major differences in their regulation stemming from the precise localization of these enzymes within cells. This nanodomain regulation depends on cell type, PDE subtype, and isoform and is yielding new ways to leverage their modulation to achieve various therapeutic goals. This review discusses new insights into compartmentation of PDE signaling with a focus on their role in the heart in both health and disease. We refer the reader to several excellent reviews on PDEs[1,2] that provide extensive and complementary information to what is presented here.

Cyclic Nucleotide PDEs: General Features: The PDE superfamily comprises 11 primary members transcribed from 21 genes that in turn generate nearly 100 different isoforms. Each member shares a similar structure but is functionally unique. The extensive number of isoforms arises from multiple transcription start sites and alternative splicing, and these features, along with tissue- or cell-specific expression and intracellular localization, result in individualized signaling roles[3]. Each PDE (and often isoform) has different affinities for the two cyclic nucleotides, favoring one or the other to some degree. PDE1, 2, 3, 10, and 11 hydrolyze both cAMP and cGMP, whereas PDE4, 7, and 8 are cAMP specific and PDE5A, 6, and 9A are cGMP specific. Of these, PDE1-5, PDE8, and PDE9 are expressed and functional in the heart.

Each PDE contains a conserved C-terminal catalytic region as well as a variable N terminus. The catalytic site consists of approximately 350 conserved amino acids. Of these, an invariant glutamine residue helps form bonds with both cyclic nucleotides and PDE inhibitors (false substrates), and a highly conserved phenylalanine residue aids particularly in bond formation to inhibitors[4, 5]. Together, these conserved hydrophobic residues act as clamps to lock inhibitors in the active site. The bonds formed determine the orientation of the inhibitor in the catalytic site, ultimately impacting how well it can inhibit the PDE. However, variable residues in the active site also provide subtype inhibitor specificity. For example, PDE9A has a Tyr424 residue, a site that is a Phe in all other isoforms, allowing for the design of highly specific PDE9A inhibitors[6, 7]. The variable N-terminal region of each PDE provides functional and localization differences. In addition, the N-terminal region can vary in posttranslational modifications (such as phosphorylation sites) that ultimately impact PDE activity and complexing with other proteins in signalosomes. **Figure 1.1** depicts the major molecular features that control PDEs, including allosteric regulation by cyclic nucleotides (e.g., PDE2A; **Figure 1.1a**), intracellular targeting by N-terminal region-localizing sequences (e.g., PDE4A1; **Figure 1.1b**), and substrate selectivity in the catalytic domain (e.g., PDE10A2; **Figure 1.1c, d**). **Figure 1.2** shows schematics for the general structure and regulatory modulation for all the PDEs found in heart.

Figure 1.1: Mechanisms of PDE regulation, localization, and substrate selectivity.

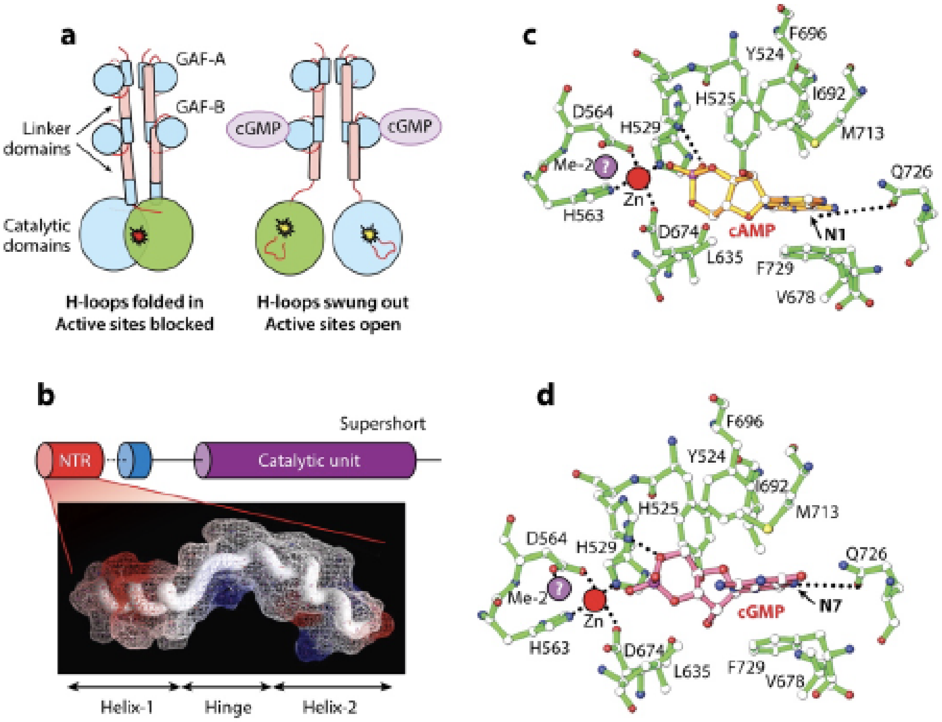

Figure 1.1: Mechanisms of PDE regulation, localization, and substrate selectivity. (*a*) Allosteric regulation of PDE2A. The dimeric protein shows an intermolecular interface along the entire length of the two monomers, including binding of the two catalytic domains that inhibit cyclic nucleotide hydrolysis. An H-loop domain (residues 702-723) folds in a position to block the active binding site. However, when cGMP binds to the GAF-B regulatory domain (These motifs are named 'GAF domains' for their presence in cGMP-regulated cyclic nucleotide PDEs, certain adenylyl cyclases and the bacterial transcription factor FhlA), the H-loops swing out, separating the catalytic domains and exposing the active sites. This results in enhanced cAMP hydrolysis. Panel adapted from Reference 8 with permission[8]. (*b*) N terminus targeting of PDE4A1. PDE4 isoforms contain NTRs in the first two exons that code for effective intracellular zip codes, targeting the protein to specific

locations in the cell. The example here is for the supershort form of PDE4A1, where the NTR contains two helix regions separated by a linker. Calcium interaction with an aspartate residue (Asp21) triggers a conformational change in helix-2, allowing two tryptophans (Trp19 and 20) and one leucine (Leu16) to insert into the Golgi membrane for specific targeting. Panel adapted from Reference 9 with permission[9]. (*c*) cAMP placement in the catalytic site of the dual-substrate esterase PDE10A2. Binding is in the *syn* conformation. Zinc (*red ball*) coordinates bonds between His529, His563, Asp564, and Asp674. The second, less clearly defined metal (Me-2) is shown by a purple ball. Hydrogen bonds are denoted by dotted lines. The invariant Gln726 makes two hydrogen bonds with N1 and N6 of cAMP, the adenine ring is embraced by the hydrophobic clamp formed by Phe729 on one side and Phe696 and Ile692 on the other side, and the cyclic phosphate group forms one hydrogen bond with His525 and three bonds with water molecules (not shown). (*d*) cGMP placement in the catalytic site of PDE10A2. cGMP binding involves an approximately 180° orientation flip as compared to cAMP, but the guanine is sandwiched in the same hydrophobic clamp and the phosphates occupy a similar location. In contrast to cAMP binding, the invariant Gln726 makes only one hydrogen bond with N7 of cGMP. Panels *c* and *d* adapted from Reference 2 with permission. Abbreviations: cAMP, cyclic adenosine 3′,5′-monophosphate; cGMP, cyclic guanosine 3′,5′-monophosphate; GAF domain; NTR, N-terminal region; PDE, phosphodiesterase.

Figure 1.2: Comparative structure and regulation of cardiac PDEs.

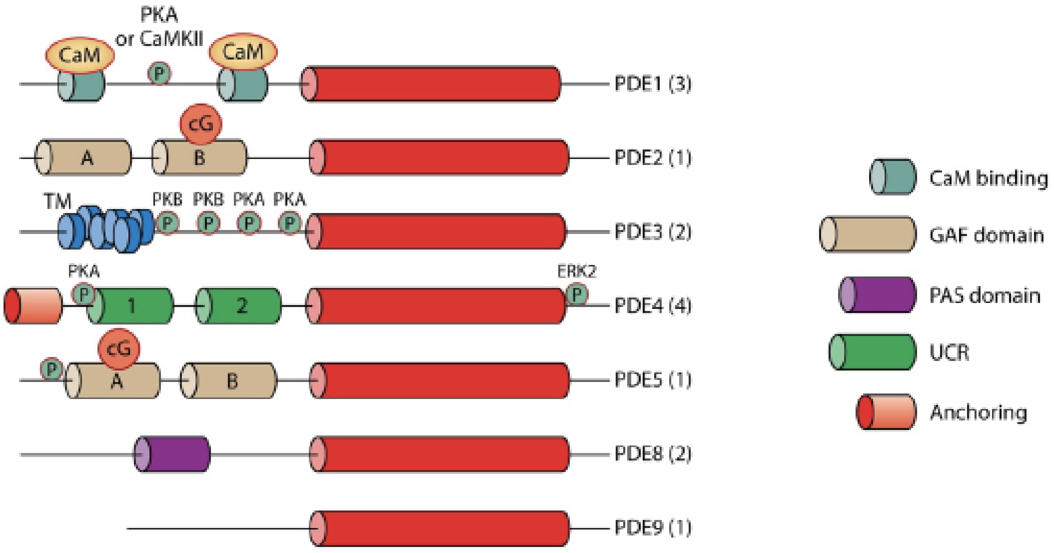

Figure 1.2: Comparative structure and regulation of cardiac PDEs.

Each PDE is shown with corresponding details pertaining to its regulatory N-terminal region. Phosphorylation sites and the associated kinases are shown, along with cyclic nucleotide--binding GAF domains, upstream conserved regions (UCRs), transmembrane domain (TMs), calmodulin (CaM) binding sites, and membrane anchoring domains. Other abbreviations: CaMKII, calcium-calmodulin dependent kinase-II; cG, cyclic guanosine 3′,5′-monophosphate; ERK2, extracellular signal-regulated kinase 2; GAF domain; PAS domain; PDE, phosphodiesterase; PKA, protein kinase A; PKB, protein kinase B.

Virtually all PDE inhibitors, whether identified by traditional small-molecule screening or designed from known structural chemistry, target the catalytic site. Broad-based inhibitors were discovered first, notably the xanthine derivatives such as theophylline, caffeine, and 3-isobutyl-1-methylxanthine (IBMX). Theophylline was the earliest PDE-inhibiting pharmaceutical to become a drug in the early twentieth century. It combined inotropic, diuretic, and bronchospasmolytic properties. However, it also induced arrhythmias, including tachycardia, and could cause nausea, vomiting, or worse, seizures. It was also fairly weak, and even low doses could produce serious adverse effects. This lack of potency and nonselective activity diminished its therapeutic use. IBMX was used widely in cellular and biochemistry studies, but it inhibited all PDEs except PDE8 and PDE9. Methods to better identify and separate PDE isoforms using anion exchange chromatography were reported in the 1970s, and with the report from Reeves et al. in 1987[10], the current system of PDE1-PDE5A was established. Subsequent work by Conti & Beavo[11] established the current superfamily classification. Selective PDE separation enabled identification of selective antagonists, such as amrinone for PDE3 and rolipram for PDE4. Newer efforts are taking advantage of molecular structural data to generate even more selective and potent inhibitors, with IC_{50} values in the nanomolar or picomolar range.

cAMP and cGMP are critical second messengers influencing many signaling pathways in the heart. cAMP is produced by 1 of 10 adenylyl cyclase (AC) isoforms (9 of which are transmembrane), with differential expression among cell types. In the heart, Ca^{2+}-inhibited AC5 and AC6 dominate, whereas Ca^{2+}-activated AC1 and AC7 are expressed in sinoatrial nodal cells[12]. cAMP can in turn activate protein kinase A (PKA) or the guanine-nucleotide exchange factor Epac[13], both capable of modifying cellular growth and function. PKA provides rapid response changes to stress by phosphorylating a broad variety of targets, including the voltage-gated L-type calcium channel (LTCC); the calcium cycling proteins phospholamban (PLB) and ryanodine receptor (RyR2); the myofilament proteins myosin binding protein C, titin, troponin I; and other proteins. Phosphorylation of these proteins enhances Ca^{2+} influx and cycling by the sarcoplasmic reticulum (SR) as well as sarcomere contractility, relaxation, and myocyte distensibility. Epac is associated with intracellular Ca^{2+} modulation by calcium-calmodulin dependent kinase-II (CaMKII), the phosphatase calcineurin, and GTP-binding proteins[14]. cAMP can also activate cAMP response-element binding protein (CREB) via PKA-mediated phosphorylation to promote gene expression[15]. Depending on the precise nature of cAMP stimulation and its corresponding downstream activators, chronic stimulation can be detrimental to both cardiac structure and function. In addition to contraction, cAMP also regulates heart rate by affecting hyperpolarization-activated cyclic nucleotide gated-channels (HCNs)[16]. In mice, gene deletion of the most prominent isoform, HCN4, results in marked slowing of heart rate and heart block[17]. However, channel gating of HCN4 is regulated not only by cAMP[18] but also by PKA phosphorylation via a parallel pathway[19].

cGMP is produced by one of two guanylyl cyclases (GCs)[20]. The first is a soluble GC (sGC), located both in the cytoplasm and at the plasma membrane[21, 22], that is activated by nitric oxide (NO) produced by NO synthase (NOS). In myocytes, β3-adrenergic receptors (β3-ARs) activate this enzyme[23-25]. The second GC is an intracellular membrane-localized enzyme that is coupled to the natriuretic peptide (NP) receptor (GC-A/B) and activated upon receptor agonism. cGMP in turn activates protein kinase G (PKG), which phosphorylates multiple intracellular targets.

PKG is expressed by two genes, *Prkg1* and *Prkg2*, the former existing as two splice variants---*Prkg1a* and *Prkg1b*. Of these, PKG1α protein is the most prominently expressed in the cardiovascular system. In myocytes, targets of phosphorylation by PKG include members of the transient receptor potential channels[26, 27], regulator of G protein signaling proteins[28-30], troponin I[25, 31], myosin binding protein C[32], PLB, PDE5A[33], the proteasome[34], and the mitochondrial K_{ATP} channel[35]. As these studies demonstrate, PKG acts as a brake that can counter physiological and pathological stress and provide cardioprotection in hypertrophied, ischemic, and failing hearts.

PDEs and the Compartmentation of Cyclic Nucleotide Signaling: All components of the cAMP and cGMP signalosome reside within distinct intracellular compartments, which include locally distributed PDEs. For cAMP-PKA, this complex coalesces around a family of proteins known as A-kinase-anchoring proteins[36]. There is no direct correlate for cGMP-PKG, although G-kinase-interacting proteins have been reported and are thought to bind to PKG via its N terminus coiled coil (leucine zipper) domain[37-39]. These systems for cAMP and cGMP enable each of the cyclic nucleotides to regulate cell signaling differently depending on how and where they were actuated.

Exploration of nanodomain control has developed rapidly with advances in genetically encoded fluorescent proteins that can detect regionally circumscribed cyclic nucleotides or kinase activity. Most of these rely on Förster resonance energy transfer (FRET), and several have been stably, genetically introduced into mice, allowing isolation of mature cells containing a cAMP- or cGMP-sensitive sensor[40-43]. So far, the greatest success has been with cAMP-PKA with excellent reporters for both. cGMP sensors have been more difficult to develop, in part because cGMP levels are often very low and thus require greater reporter sensitivity. A successful PKG-activity sensor has not yet been developed. Still, existing probes are providing in vitro and in vivo understanding of how compartmentation is regulated.

Studies with cAMP FRET biosensors targeted to the plasma membrane and the sarcoplasmic endoplasmic reticulum calcium (Ca^{2+}) ATPase 2a (SERCA2a) microdomains have revealed differential regulation of β1- and β2-ARs by PDEs in healthy cardiomyocytes, with PDE2, 3, and 4 controlling cAMP equally from the β1-ARs and PDE3 controlling cAMP primarily from the β2-ARs[43]. Other studies found that PDE3 and PDE4 are both responsible for controlling cAMP in the SERCA2a-containing microdomain and regulate PLB phosphorylation[40]. In addition, PDE3 and PDE4 act together to chaperone cAMP from its synthesis at the membrane to SERCA2a. cGMP FRET sensors are more limited in signal strength and are so far best suited to NP-pathway detection. A new probe (called cGES-DE5 by the authors) uses the PDE5A cGMP binding domain coupled to green (T-Sapphire) and red (Dimer2) fluorescence peptides and shows a better signal-to-noise ratio than prior versions while retaining cGMP selectivity[44, 45], whereas one that used a binding domain from *Plasmodium falciparum* PKG has provided adequate sensitivity even if targeted to specific cellular compartments[46]. Another non-FRET cGMP sensor, FlincG[47], has been useful for real-time cGMP dynamic imaging and detection of selective PDE regulation in neonatal myocytes[48]; however, the signal was not sufficient for detection of cGMP in adult cells. New variants of FlincG may improve upon this limitation[49].

FRET sensors for PKA isoforms have revealed differences in signaling coupled to PKA with regulatory subunit I or II (PKA-RI and RII). PKA-RI is activated in response to prostaglandin receptor (EP2 and EP4) activation, during which signaling via PKA-RII is shut down through the EP3 receptor and G_i-coupled mechanisms. By contrast, PKA-RII is activated selectively in response to β-AR stimulation[50]. Costimulation of cGMP with β-AR stimulation shifted activation to PKA-RI, providing a novel mechanism for regulating cAMP/cGMP crosstalk[51]. Another tool is a genetically targeted kinase inhibitor, such as one used to block PKA at the endoplasmic reticulum[52]. This intriguing approach remains to be developed for other microdomains or extended to PKG.

Several sensors have also been expressed stably in mice. cAMP-reporting mice have been used to show reduced PDE3 control of β2-AR signaling and relocalization of PDE2 from β1-AR to β2-AR after mild pressure overload[43]. Mice with cGMP sensors have been generated and appear most useful for studying the NP-signaling pathway[41, 42]. Plasma membrane cGMP compartments have also been detected using electrophysiological methods in combination with expression of cGMP-sensitive ion channels[53].

Understanding where PDEs reside in the cell in order to actuate their control of cyclic nucleotides is also critical. Studies to date have primarily focused on co-immunoprecipitation of PDEs in order to identify binding partners by mass spectrometry. A newer method of approaching nanodomain identification is proximity proteomics, which has not yet been applied to PDEs. With this method, a protein of interest is tagged with either a biotin ligase or a peroxidase and overexpressed in cells. Upon incubation with biotin and other appropriate reagents, the fusion protein will biotinylate its neighboring proteins within a small radius, facilitating pulldown of these biotinylated proteins and identification by mass spectrometry. Several biotin ligases have been engineered for this purpose (BioID[54], BioID2[55], TurboID[56], and miniTurbo[56]), as well as several peroxidases (APEX[57] and APEX2[58]). Notably, the peroxidases require H_2O_2 stimulation in addition to biotin in order to stimulate biotinylation, which may be a drawback for some studies; however, they can also be used for electron microscopy to acquire high resolution images of PDE localization without the need for an antibody, which cannot be done with the biotin ligase tags[58, 59].

PDE5: PDE5A is a cGMP-specific PDE with three isoforms, PDE5A1-3, all expressed in humans[60], although there is as yet no known difference in their function or localized signaling. PDE5A activity is modulated by cGMP binding to GAF regulatory domains and by PKG phosphorylation (S92 in mouse, S102 in human), both resulting in PDE activation[61, 62] (**Figure 1.3**). Of the two primary pathways generating cGMP (NO- and NP-dependent cascades), PDE5A regulates the former selectively in myocytes[48, 53, 63, 64]. Inhibiting PDE5A counters maladaptive cardiac structural and functional remodeling in both hypertrophic[65] and ischemic heart disease[66], blocking multiple pro-hypertrophic and fibrotic signaling pathways by PKG-dependent mechanisms[67]. During ischemia-reperfusion, PDE5A inhibitors reduce infarct size and cardiomyocyte apoptosis; cardioprotection requires opening of the mitochondrial K_{ATP} channel[68-70]. PDE5A normally localizes at the Z-disc of cardiomyocyte sarcomeres, but this localization shifts to a more diffuse pattern in failing hearts and late-stage hypertrophy and dilation, and if endothelial NOS (eNOS or NOS3) is pharmacologically inhibited or genetically deleted[64, 71, 72]. Normal PDE5A intracellular localization can be restored by directly stimulating sGC to generate cGMP even in the presence of NOS inhibition. This indicates that intramyocyte PDE5A localization itself depends on the availability of its favored substrate - sGC-derived cGMP. These localization changes are unrelated to PKG-targeted S92 phosphorylation of PDE5A[73].

Figure 1.3: Cardiac myocyte regulation by PDE5A and PDE9.

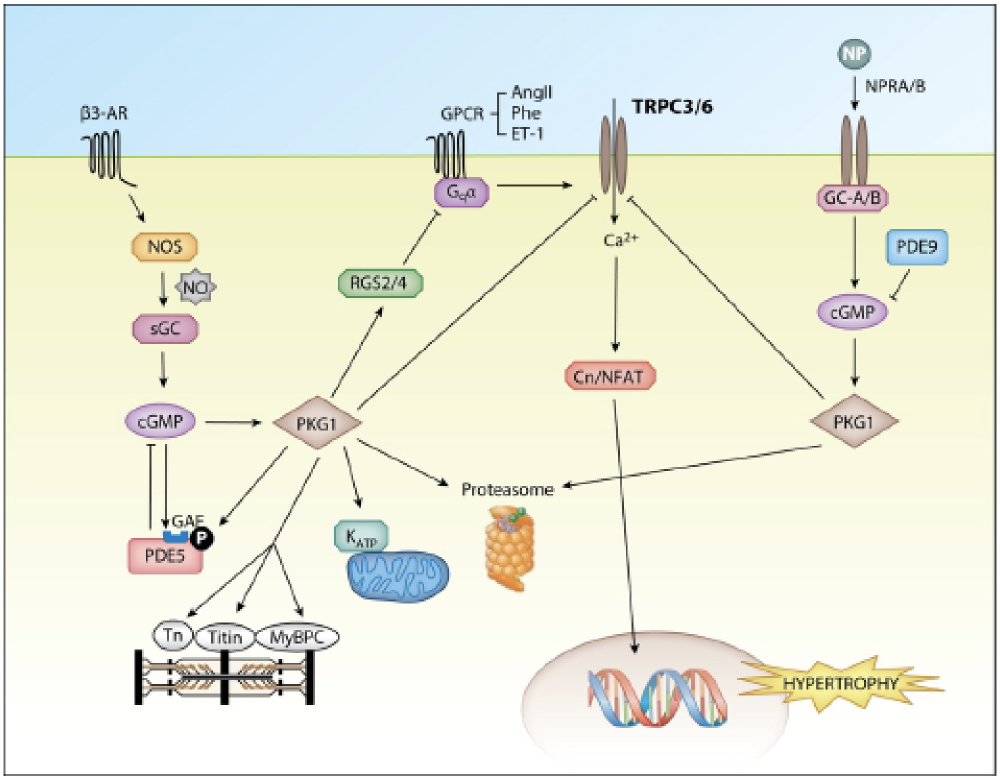

Figure 1.3: Cardiac myocyte regulation by PDE5A and PDE9.

Both of these PDEs regulate cGMP very selectively. As depicted, PDE5A controls NO-stimulated cGMP, and PDE9 controls NP-stimulated cGMP. Both pathways converge on PKG1; however, these are also likely different pools of the kinase (hence, two icons are shown) with some overlapping functionality but also some very signaling pathway-specific effects as well. The figure shows the impact of PKG1 in suppressing G_q-coupled protein receptors by RGS proteins; blocking TRPCs; stimulating mitochondrial protection via K_{ATP} channels; enhancing proteasome function; and modifying multiple proteins in the sarcomere, including Tn, titin, and MyBPC. Abbreviations: β-AR, β-adrenergic receptor; AngII, angiotensin-II; cGMP, cyclic guanosine 3′,5′-monophosphate; Cn, calcineurin; ET-1, endothelin-1; GAF domain; $G_q\alpha$, G-protein(αq); GPCR, G protein--coupled receptor;

MyBPC, myosin binding protein C; NFAT, nuclear factor of activated T cells; NO, nitric oxide; NOS, nitric oxide synthase; NP, natriuretic peptide; NPR, natriuretic peptide receptor; PDE, phosphodiesterase; GC-A/B, guanylyl cyclase-A/B; PKG, protein kinase G; RGS, regulator of G protein signaling; sGC, soluble guanylyl cyclase; Tn, troponin I; TRPC, transient receptor potential channel.

PDE5A inhibitors are used clinically to treat erectile dysfunction and pulmonary hypertension[3]. Although preclinical[65, 66, 74] and some small-scale clinical[75, 76] studies found PDE5A inhibition also ameliorates various forms of heart disease, other studies were neutral[77], and controversies and caveats regarding this strategy persist. One potential issue is that the selectivity of PDE5A for NO-stimulated cGMP could reduce its efficacy in syndromes such as heart failure, in which NO signaling is depressed by oxidant stress due to reduced NO synthesis[78, 79], sGC activation[21, 80], and cGMP generation[81, 82]. Another example in which reduced NO signaling occurs is in women with low estrogen levels. PDE5A inhibition in female mice ameliorates heart disease induced by excessive G_q-protein stimulation or mechanical overload. This treatment effect is lost following ovariectomy but restored if these animals receive estrogen replacement[83] - results that could have important implications for the use of PDE5A inhibitors in postmenopausal women. To date, the only multicenter trial of PDE5A inhibition and heart failure was in a group of patients with preserved ejection fraction (HFpEF), and the results were neutral[77]. However, this cohort has modest NP activation[84], and a majority in the study reportedly did not have ventricular hypertrophy. Left ventricular (LV) myocardium from HFpEF has low levels of cGMP and PKG activity[85], opposite to heart failure with reduced EF, and because PDE5A does not appear to be upregulated as the cause, this would limit effects from PDE5A inhibition. As discussed below, new data regarding another cGMP-targeting PDE, PDE9A[48], may shed further light into these issues and improve therapeutic targeting.

PDE9: PDE9A is a cGMP-specific PDE with the highest affinity for cGMP of any of the PDE superfamily members[86]. Until recently, nothing was known about the role of PDE9A in the heart, although it is expressed at the mRNA level in myocardium[86, 87]. However, a recent study determined that PDE9A is expressed at protein levels in human and other mammalian hearts, that it is functional, and that it specifically regulates cGMP resulting from NP stimulation of GC-A/B[48]. PDE9A protein expression is observed in a different subcellular location in myocytes, co-staining with the SR based on SERCA2a immunohistochemistry (**Figure 1.4A**). This differs from the Z-disk localization of PDE5A. Expression is very low in normal mouse and human myocardium but is upregulated by heart failure (**Figure 1.4B**) with or without reduced systolic function, suggesting that targeting these diseases with PDE9A inhibitors may be useful. PDE9A protein expression and activity are elevated in human heart failure, notably in both forms with reduced or preserved ejection fraction, the latter being a disease which has been particularly refractory to successful therapy and in which PDE5A inhibition was previously tested and did not improve clinical status[77, 88].

Figure 1.4: NO-independent PDE9A modulation of cardiac stress responses.

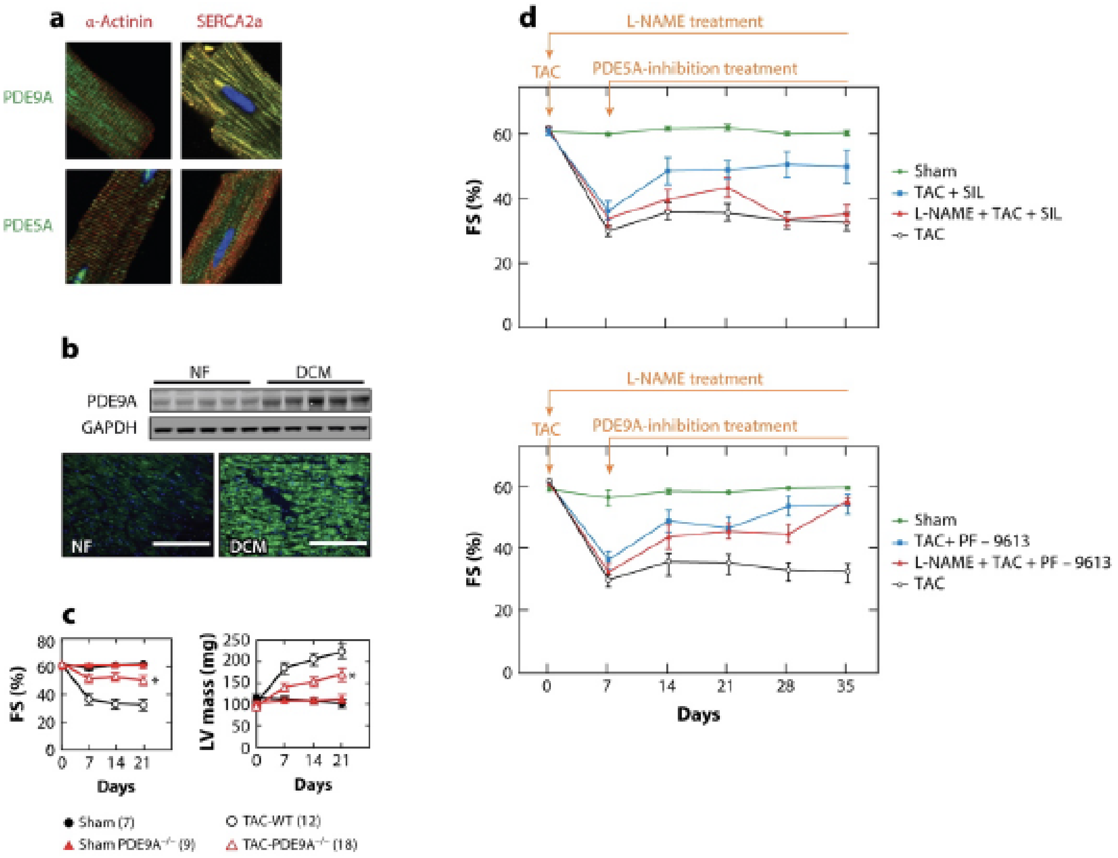

Figure 1.4: NO-independent PDE9A modulation of cardiac stress responses.

Unlike PDE5A, which hydrolyzes primarily cGMP generated by NO-stimulated sGC, recent work has shown PDE9A targets NP-GC-A/B--derived pools of this cyclic nucleotide. (*a*) Both PDEs are localized to different compartments in the cardiac myocyte, with PDE5A expression colocalizing to the Z-disk (costaining with α-actinin), whereas PDE9A colocalizes with T-tubular membranes (with SERCA2a). (*b*) Expression in the normal heart is very low but is increased in conditions such as human heart failure. (*c*) Mice globally lacking PDE9A display protection to sustained pressure overload-induced cardiac stress, with enhanced cardiac FS and reduced hypertrophy (LV mass). Asterisks indicate $P < 0.01$ as compared to WT TAC. (*d*) Unlike PDE5A inhibition, which does not improve cardiac function depressed by pressure overload if NOS is also inhibited (L-NAME), PDE9A inhibition is equally effective with or without concomitant NOS inhibition. Figure adapted with permission from Reference 48. Abbreviations: cGMP, cyclic guanosine 3′,5′-monophosphate; DCM, dilated cardiomyopathy; FS, fractional shortening; GAPDH, glyceraldehyde 3-phosphate dehydrogenase; GC-A/B, guanylyl cyclase-A/B; L-NAME, L-N^G-Nitroarginine methyl ester; LV, left ventricular; NF, non-failing,; NO, nitric oxide; NOS, nitric oxide synthase; NP, natriuretic peptide; PDE, phosphodiesterase; PF-9613 (PDE9 inhibitor); SIL, sildenafil, PDE5-inhibitor; TAC, trans-aortic constriction; WT, wild type.

PDE9A inhibition or gene deletion during murine cardiac hypertrophy induced by transaortic banding improved cardiac function and decreased fibrosis, cardiomyocyte size, and maladaptive signaling (**Figure 1.4C**). The functionality of PDE9A inhibition differs importantly from that due to PDE5A suppression. Phosphoproteomic analysis revealed that PKG activation by inhibition of PDE5A or PDE9A led to several overlaps but also many striking differences in protein phosphorylation and transcriptional regulation[48]. For example, whereas inhibiting either suppressed transcriptional activity linked to NFAT to trigger antihypertrophic effects[27], only PDE9A suppression augmented GATA binding protein 4, which is linked to angiogenesis[89]. Mice subjected to pressure overload and treated with a selective PDE9A inhibitor, but not a PDE5A inhibitor, were protected even when NOS was blocked by L-N^G-Nitroarginine methyl ester (L-NAME) administered in drinking water (**Figure 1.4D**). This confirmed at the whole heart level what isolated cell studies had revealed about the differential targeting of NP- versus NO-stimulated cGMP pools by the two PDEs.

Previous clinical studies of PDE9A inhibitors pursued their utility to improve neurocognitive function and were tested in schizophrenia, Huntington's disease, and Alzheimer's disease[90-92]. The inhibitors were well tolerated, and while many preclinical studies had reported positive cognitive effects in mouse models of these disorders[93, 94], benefits were not observed in the limited human data reported to date[95]. The new findings in the cardiovascular system reveal an entirely different potential use. Given the interaction of PDE9A and the NP signaling system, and the utility of valsartan/sacubitril, a combined angiotensin-2 receptor blocker and neprilysin inhibitor (the latter blocking NP proteolysis)[96], PDE9A inhibitors may be synergistic with these new drugs.

Clinical Translation, Future Issues, and Conclusions: One of the defining features of PDE pharmacology is that despite structural similarities of the catalytic site among the different species of PDEs, they are sufficiently unique to enable generation of highly specific inhibitors. Crystal structures have been obtained for many PDEs, which is facilitating drug design and discovery. Most of these new inhibitors are effective at nanomolar concentrations. Further, with the exception of PDE2, inhibitors are available for all known PDEs affecting heart function, and they have been found to be safe for and are being tested in humans. Other than PDE3 and PDE5A, these studies have not focused on cardiac indications, but this is a changing landscape. The major limitation with these agents has been the lack of greater isoform-selective inhibition, which some believe may be possible, although to date this has been elusive. The elegance of intracellular compartmentalized signaling is thus potentially lost when multiple forms are modulated at the same time. The clinical utility of PDE3 inhibitors likely suffered because of this, and improved selectivity may be able to alter the outcome from these agents for cardiac disorders. Another factor is that organ selectivity has been difficult, although this is helped to some extent by differential expression of various PDEs in the tissues. This has important clinical implications, as modifying the NO-signaling pathway by sGC activation, for example, will impact a broader variety of cell types than would occur by inhibiting PDE5A---whose tissue expression is more selective. PDEs with broader expression may be less druggable unless isoform selectivity and thus the ability to better target effects are possible.

Another evolving paradigm is the use of multiple PDE inhibitors in combination with cyclic nucleotide stimulation pathways---each at doses that alone have very modest impact but when combined yield greater cell-targeted signaling and alteration in function. This is a tactic used in anticancer therapy, in which multipronged attacks can produce synergistic effects. If one could provide some cyclase stimulation along with the selectivity of PDEs, the desired result could be enhanced signaling in the cell and nanodomain. This approach has yet to be developed as a clinical strategy, but with appropriate insight into which combinations are safe, there is much to be said for it. To date, small molecules that activate PDEs selectively (thereby degrading cAMP, cGMP, or both) have not been developed but might be modulators of the regulatory N terminus and may have clinical utility in certain settings.

It has been 18 years since the last PDE superfamily member (PDE11A) was identified[97]. All PDEs have been explored, and many have been targeted with inhibitors for their potential therapeutic value. Even so, rather than a field with most of its questions and problems solved, this area remains young and fresh, with active research and ongoing translational applications. The appreciation of PDE nanoregulation, the nuances this provides for molecular control, and how it might be leveraged to enhance the specificity and extent of drug responses are all active areas of inquiry. We expect this interest will surge further as newer and more effective approaches are developed to target a broad variety of diseases.

CHAPTER 2: Marked disparity of microRNA modulation by cGMP-selective PDE5 versus PDE9 inhibitors in heart disease

Modified from: Kokkonen-Simon KM et al. Marked Disparity of MicroRNA Modulation by cGMP-selective PDE5 versus PDE9 Inhibitors in Heart Disease. JCI Insight. 2018. 3(15): e121739.

INTRODUCTION

MicroRNAs: MicroRNAs (miRNAs) are small ribonucleic acids that provide post-transcriptional control of messenger RNA translation and degradation [98]. First discovered in 1993, there are now over 24,000 identified miRNAs. Their primary role is repressing gene expression by facilitating mRNA degradation, inhibiting protein translation, or degrading polypeptides through complementary binding to the 3'UTR of target mRNAs. Each miRNA impacts around 1000 individual mRNAs, generally clustering around a thematically coherent set of signaling pathways. Importantly, their expression changes with disease and therapeutic interventions, which has spawned interest in their use as both diagnostic and therapeutic agents [99, 100].

From a systems biology perspective, the position of miRNAs is generally placed above gene translation. However, growing evidence demonstrating their modification by intracellular and environmental signaling have led to their exploration as markers of disease therapy, of particular interest to the efforts to better personalize medical treatment [101, 102].

However, such data remains fairly limited, and the sensitivity of miRNA signatures to treatments that share common signaling little explored.

miRNAs as Biomarkers and Therapeutics for Cardiovascular Disease: The first reports of the role of miRNAs in heart disease came in 2006 when the Olson lab reported enhancement of miR-208 in pathological hypertrophy and therapeutic benefits from its reversal [103-105]. Other similar examples followed, including suppressing miR-122/132 or increasing miR-1 or miR-133 [106-110], with now well over 2000 studies on various miRNAs and heart disease.

In the human heart, multiple miRNAs have been shown to be dysregulated in disease. Many circulating miRNAs have been proposed as heart failure biomarkers[111]. However, a consistent heart failure miRNA profile has yet to be identified, despite some overlap between independent studies. miRNAs have also been shown to have some prognostic value. In cardiac resynchronization therapy (CRT), patients who respond to therapy have demonstrated specific miRNA expression changes, including miR-26b-5p, 145-5p, 92a-3p, 30e-5p, and 29a-3p [112]. Additionally, specific miRNAs have been shown to change in DCM patients that respond to beta-blocker treatment versus non-responders, including miR-208a-3p, 208b-3p, 21-5p, 199a-5p, and 1a-3p [113]. Several miRNA-based therapeutics have been proposed; however, none of these therapies have progressed beyond animal models, likely due to the multiplicity of miRNA targets, concerns for off-targets of the therapy in other tissues, and difficulty of delivery to the heart.

Here, we tested the hypothesis that miRNA profiling may provide a useful tool to distinguish between mechanistically very similar therapeutic interventions. To do this, we contrasted the effects of pharmacologically inhibiting either cGMP-selective phosphodiesterase type 5 or type 9 (PDE5-I, PDE9-I). Both activate protein kinase G, though they do so by modulating different cGMP pools, the former coupled to nitric oxide (NO) stimulation of guanylyl cyclase-1 (GC-1) and the latter to natriuretic peptide (NP) stimulation of guanylyl cyclase-2A [114]. Importantly, both drugs potently and very similarly improve heart disease stimulated by sustained pathological hemodynamic stress [114]. Despite this, the miRNA profiles were dramatically and surprisingly different, with PDE5-I reducing a very broad array of miRNAs associated with the disease state, whereas PDE9-I had virtually no impact.

METHODS

Cardiac pressure-overload (PO) model: Pressure overload was induced by trans-aortic constriction, performed as previously described[114]. Size-, age- and sex-matched (male) C57BL/6J mice (Jackson Labs) were used for all drug intervention studies. Sham controls underwent similar surgery without ligature placement. Mice were followed for up to 6 weeks after PO, and were co-treated with PDE5-I (Sildenafil, Sil, Pfizer, 200 mg/kg/day in Bioserv soft diet), PDE9-I (PF-04449613, Pfizer, 30 mg/kg twice daily by oral gavage), BAY 60-2770 (Bayer, 0.3 mg/kg/day once daily by oral gavage), or appropriate matched vehicle. Treatment started 1 week after PO. For the drug intervention studies, animals dying prior to drug assignment or who failed to develop disease after PO were excluded from analysis. The GC-2A overexpressor mice were generated as previously described [115], and subjected to PO or sham surgery. Animals were followed for 3 weeks after PO.

Conscious mouse echocardiography: Intact heart morphology and function was determined in conscious mice by serial M-mode transthoracic echocardiography (VisualSonics Vevo 2100, 18-38 MHz linear array transducer; SanoSite Incorporated). Images were obtained and analyzed by an individual blinded to the animal condition.

miRNA sequencing: Total RNA was isolated from left ventricular myocardium using Qiazol Reagent and the miRNeasy kit (Qiagen) according to manufacturer protocol. RNA was analyzed on an Agilent Bioanalyzer for RIN values and concentrations. Only samples with RIN>7 were used for sequencing. Libraries were prepared using the Illumina TruSeq Small RNA Sample Prep Kit. Sequencing was performed on an Illumina HiSeq 2500. Illumina's CASAVA 1.8.4 was used to convert BCL files to FASTQ files. Sequencing read filtering and adapter trimming, read alignment, and generation of count data and RPM data were done using the miRge program v1.0 [116], which incorporates Cutadapt v1.18 and Bowtie v1.1.1. Differential expression analysis was performed using Bioconductor's DESeq package (v1.26.0) [117]. miRNAs were filtered according to the following: more than 50% of mice had reads for a given miRNA, and the miRNA was present in the *Mus musculus* miRgeneDB database [118]. Heatmaps were generated using the Morpheus program (Broad Institute). Clustering was performed by the one minus Spearman rank correlation. The data discussed in this publication have been deposited in NCBI's Gene Expression Omnibus [119], and are accessible through GEO Series accession number GSE112056 (https://www.ncbi.nlm.nih.gov/geo/query/acc.cgi?acc=GSE112056).

RNA sequencing: RNA samples were prepared and analyzed as described for miRNA-seq. Libraries were generated using the TruSeq Stranded Total RNA sample preparation kit

(Illumina), and sequenced on an Illumina HiSeq 2500. Illumina's CASAVA was used to convert BCL files to FASTQ files. RNA-seq reads were trimmed and mapped to the Ensembl mouse reference genome (mm10) using HISAT2 version 2.0.5 [120]. Transcript counts were quantified using RSEM v1.3.0 with default parameters [121]. Differential expression (DE) analysis of genes between different treatments was performed using R package DESeq2 v1.18.1[122]. Pathway enrichment analysis was done using the Kyoto Encyclopedia of Genes and Genomes (KEGG) database and R package KEGG.db v3.2.3) [123]. The data discussed in this publication have been deposited in NCBI's Gene Expression Omnibus [119], and are accessible through GEO Series accession number GSE112056 (https://www.ncbi.nlm.nih.gov/geo/query/acc.cgi?acc=GSE112056).

Gene expression – qRT-PCR: Total RNA was isolated from left ventricular myocardium, lung, or cultured cells using Qiazol Reagent and the miRNeasy kit (Qiagen) according to manufacturer protocol. Reverse transcription to cDNA was performed using the miScript II RT kit (Qiagen). cDNA underwent PCR amplification for mRNA expression using TaqMan probes for atrial natriuretic peptide (ANP) (mouse #Mm01255747_g1), brain or B-type natriuretic peptide (BNP) (mouse #Mm01255770_g1), Argonaute 2 (Ago2) (mouse #Mm00838341_m1), DGCR8 (mouse #Mm01146851_m1), Dicer1 (mouse #Mm00521722_m1), Drosha (mouse #Mm01310009_m1), or glyceraldehyde-3-phosphate dehydrogenase (GAPDH) (mouse #99999915_g1) (Applied Biosystems). For mature miRNA expression, Qiagen miScript probes were used for miR-1a (mouse MS00011004), miR-101a (mouse MS00011011), miR-133a (mouse MS00032305), miR-145 (mouse MS00001631), miR-195 (mouse MS00001792), miR-199 (mouse MS00032529), miR-208b (mouse MS00011466), miR-21 (mouse MS00011487), mir-214 (mouse MS00032571), miR-

26b (mouse MS00001344), mir-27b (mouse MS00001358), miR-29 (mouse MS00001372), miR-29c (mouse MS00001379), miR-30b (mouse MS00001386), miR-30d (mouse MS00011746), miR-34c (mouse MS00001422), miR-451a (mouse MS00002408), and RNU6-2 (human, MS00033740). For pre-miRNA expression, Qiagen probes were used for pre-miR-1a (mouse MP00003990), pre-miR-199 (mouse MP00004970), pre-miR-208b (mouse MP00005082), pre-miR-21a (mouse MP00005103), and pre-miR-34c (mouse MP00005628). For pri-miRNA expression, Taqman probes were used for pri-miR-1a (mouse #Mm03306163_pri), pri-miR-199 (mouse #03306505_pri), pri-miR-208b (mouse #Mm03308667_pri), pri-miR-21a (mouse #Mm03306822_pri), and pri-miR-34c (mouse #Mm03306660_pri). The threshold cycle value was determined using the crossing point method. Samples were normalized to the GAPDH value for each Taqman run, and RNU6-2 for each miScript run.

Statistical Analysis: All values are presented as mean ± SEM. For analysis of multiple independent groups, a 1-way ANOVA or Kruskal Wallis test was used with a post hoc Tukey (or Dunns) multiple comparisons test to assess group differences. Post hoc testing was only performed if the 1W-ANOVA was significant ($p<0.001$ in all cases). For analysis of only two independent groups, an unpaired two-tailed T-test was performed. Analysis was performed using Graphpad Prism software (Ver. 7a, 2016).

Study approval: All animal studies performed in this paper were approved by either the Johns Hopkins Medical Institutions Animal Care and Use Committee (Baltimore, MD, USA) or the University of Würzburg animal care committee (Würzburg, Germany).

RESULTS

PDE5-I and PDE9-I applied to PO heart yield very disparate miRNA profiles

Mice were subjected to sustained pressure-overload (PO) for 5 weeks and further randomized to receive either the PDE5 inhibitor (sildenafil) or PDE9 inhibitor (PF-04449613), each initiated one week after PO. Reported hemodynamic and morphological data from these mice documents similar reduction of hypertrophy and cardiac dilation, as well as reversal of abnormal molecular signaling and fibrosis, and improved heart function [65, 114]. Salient data are provided in **Figure 2.1**.

Figure 2.2 displays miRNA-seq results as volcano and heat-map plots for three group comparisons: PO+vehicle versus sham-control, PO+PDE5-I versus PO+vehicle, and PO+PDE9-I versus PO+Vehicle. Each analysis was derived from whole myocardial tissue isolates obtained at terminal study (5 weeks after PO). With PO, 63 miRNAs significantly increased and 48 declined **(Figure 2.2A, Table 2.1)**. Many miRNAs reported to be either enhanced (miR-208b, 199, 199b, 21a, 34b, and 34c) or diminished (miR-133a, 133b, and 1a) by PO were observed in this analysis. PDE5-I reduced miRNA expression broadly (**Figure 2.2B, Table** 2.2) as seen in the volcano plot with the vast majority of changes in the negative log-fold region. This either reversed or further diminished expression of many of the miRNAs altered by PO, and lowered others unchanged by PO. In stark contrast, PDE9-I minimally altered miRNAs associated with PO, impacting only 9, 5 of which reversed PO changes (**Figure 2.2C, Table 2.3**). The magnitude of the change of even these 9 was modest. A heat map using hierarchical clustering aggregated PO and PO+PDE9-I together, each being quite different from either Sham or PO+PDE5-I groups (**Figure 2.2D**). The miRNA names for each row are provided in **Table 2.4**.

Figure 2.1: Phenotypic improvement in PO mice after PDE5-I and PDE9-I.

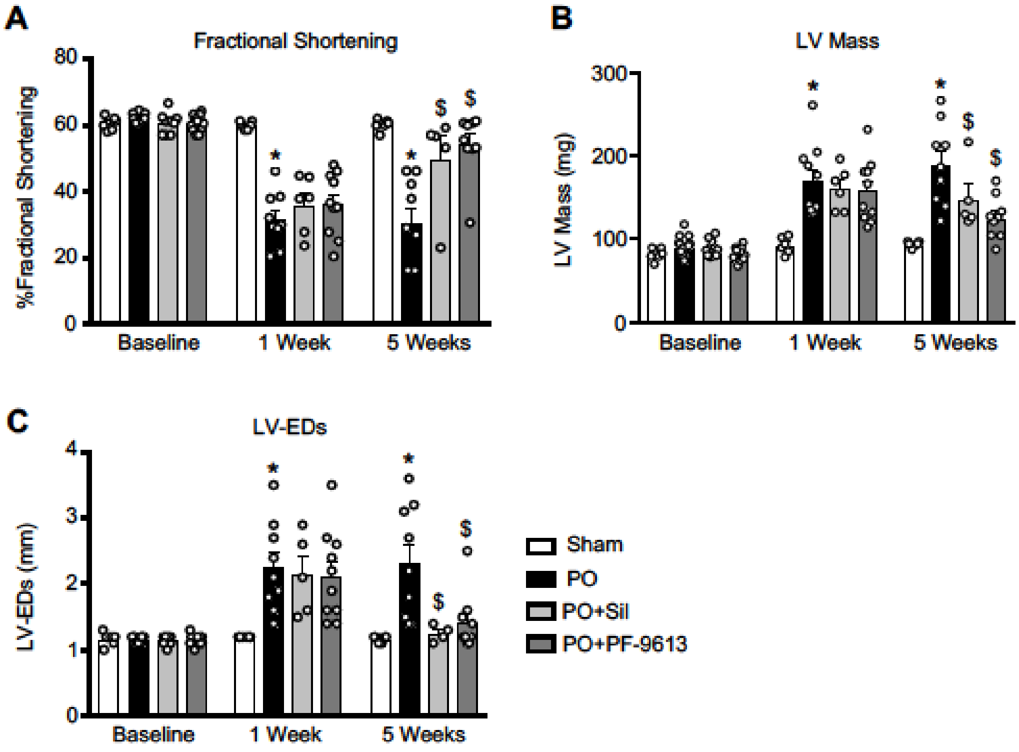

Figure 2.1: Phenotypic improvement in PO mice after PDE5-I and PDE9-I.

C57Bl6/J mice were studied as previously described [114]. Left ventricular tissue was subsequently used for miRNA-seq analysis. A) Fractional shortening. B) Left ventricular mass. C) Left ventricular end-systolic dimension as a measure of dilation. All parameters were significantly improved by treatment with either Sil (PDE5-I) or PF-9613 (PDE9-I). * $p<0.05$ versus PO group baseline measurements. $ $p<0.05$ versus PO measurement as same time point. N=5-9 per group. Data is presented as mean ± SEM. Data were analyzed using multiple t-tests.

Figure 2.2: PDE5-I and PDE9-I applied to PO heart yield disparate miRNA profiles.

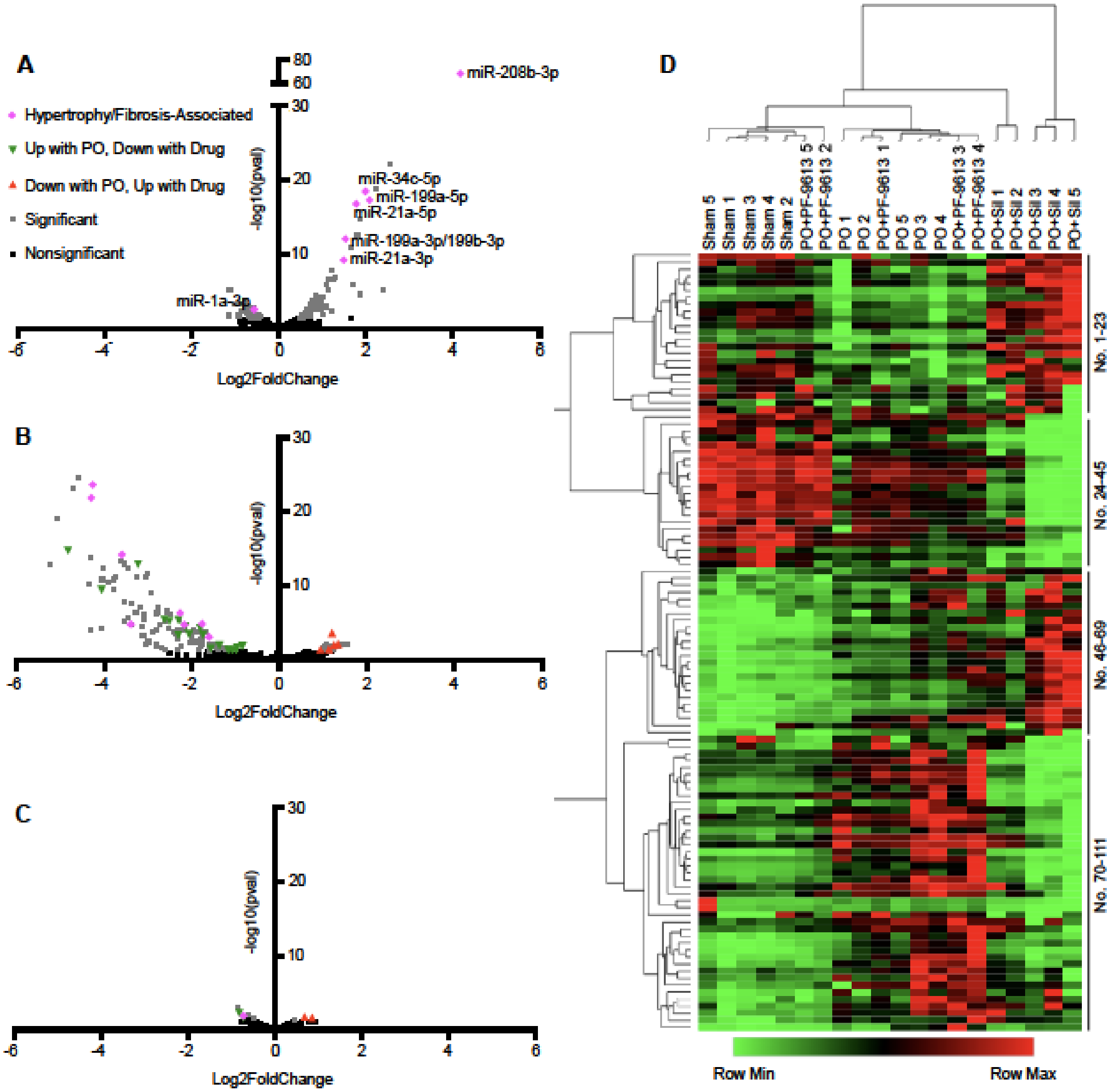

Figure 2.2: PDE5-I and PDE9-I applied to PO heart yield disparate miRNA profiles.

Left ventricle myocardium from mice subjected to sham or PO surgery and subsequently given either vehicle, PDE5-I (Sil), or PDE9-I (PF-9613) were subjected to miRNA sequencing and subsequent differential expression analysis (n=5 per group). **A)** Volcano plot of miRNAs altered in PO versus sham, with miRNAs relevant to cardiac hypertrophy/fibrosis labeled. **B)** Volcano plot of miRNAs altered in PO+Sil versus PO. **C)** Volcano plot of miRNAs altered in PO+PF-9613 versus PO. For all volcano plots, dark gray dots indicate differentially expressed miRNAs; green triangles indicate miRNAs increased with PO, and decreased with drug treatment; red triangles indicate miRNAs decreased with PO, and increased with drug treatment; and pink diamonds indicate miRNAs labeled in panel A that are associated with cardiac hypertrophy and fibrosis (legend can be found in panel 1C). **D)** Heatmap of all miRNAs changed significantly with PO for all treatment groups, clustered by both rows (miRNAs) and columns (samples). Row labels (i.e. miRNA names) can be found in **Table 2.4**.

Transcriptome for each treatment shows many changes but few are overlapping

Given the role of miRNAs, these results might predict minimal transcriptome changes from PDE9-I whereas PDE5-I treatment would be expected to more broadly alter mRNA expression. This was tested by RNA-seq on the same samples. To our surprise, more than twice as many genes were significantly altered by PDE9-I (1756) as compared to PDE5-I (868) (**Figure 2.3A**), 87% and 73% of them being unique to PDE5-I or PDE9-I treatment, respectively. Among the shared genes, all but one changed in the same direction and magnitude (**Figure 2.3B**), the one exception being *Cdh20* encoding cadherin-20 precursor.

KEGG pathway analysis for the PO condition revealed typical changes, increasing extracellular matrix, cytoskeletal, and hypertrophy and heart failure-related genes, and decreasing metabolic pathway related genes. While the specific genes altered by each treatment mostly differed, pathway analysis yielded similar clusters, with the number of genes altered declining relative to PO in cases to levels similar to Sham control (**Figure 2.3C and D**). Thus, despite targeting a similar kinase pathway, PDE5 and PDE9 inhibitors impacted genes very differently, while still converging on similar signaling pathways altered by pressure-overload stress.

Figure 2.3: Transcriptome for PDE5-I and PDE9-I shows many changes but few overlapping ones

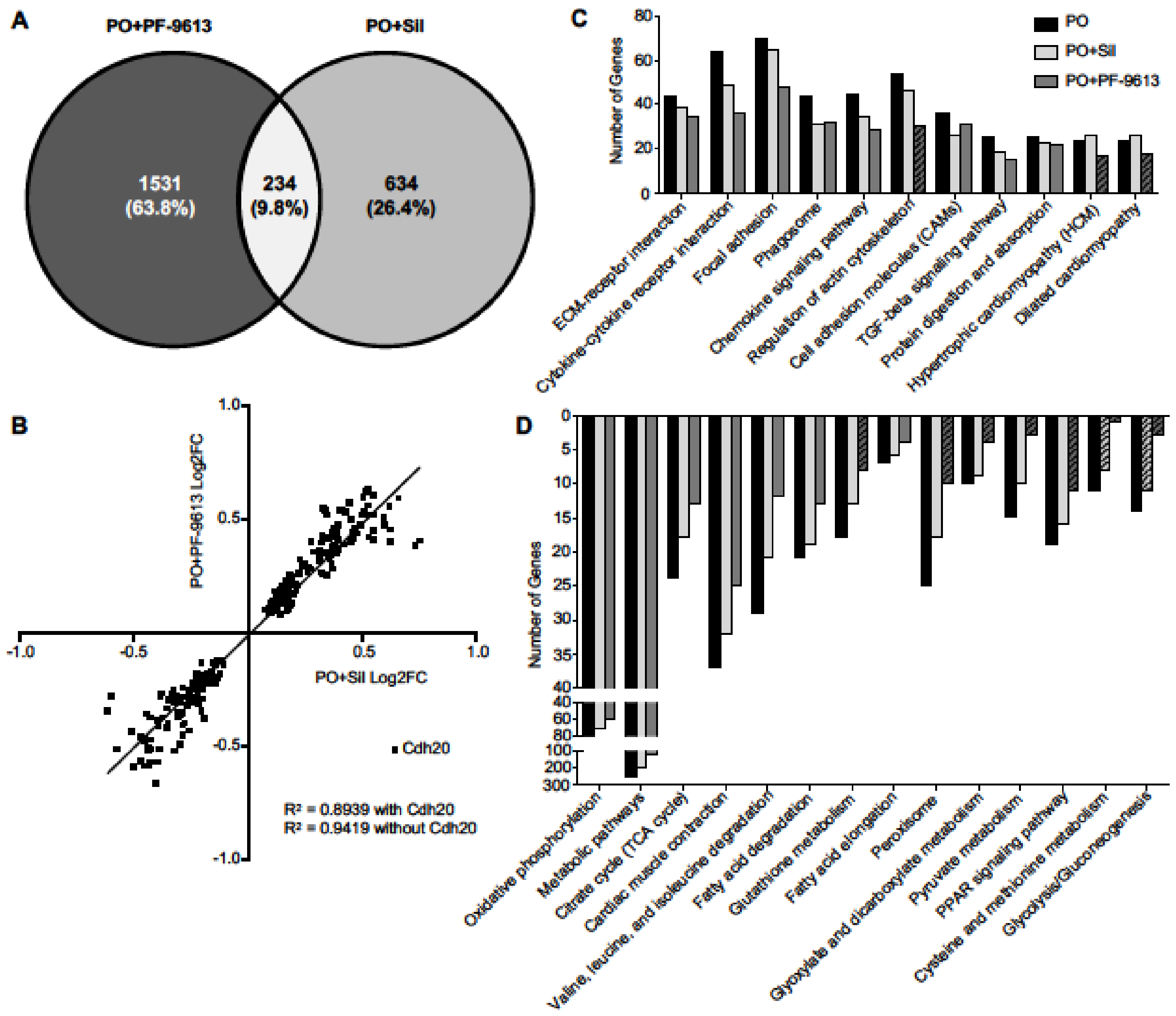

Figure 2.3: Transcriptome for PDE5-I and PDE9-I shows many changes but few overlapping ones

Samples from the same cohort of mice from Figure 1.1 were subjected to RNA-sequencing. **A)** RNA-seq analysis revealed 234 shared genes between PDE5-I (Sil) and PDE9-I (PF-9613), with more genes changed overall by PDE9-I (1756) than PDE5-I (868). **B)** Correlation analysis of fold changes of the genes shared between PDE5-I and PDE9-I. **C)** Gene numbers in KEGG pathways identified to be upregulated in PO compared to sham for PO, PO+PDE5-I, and PO+PDE9-I. **D)** Gene numbers in KEGG pathways identified to be downregulated in PO compared to sham for PO, PO+PDE5-I, and PO+PDE9-I. Striped bars in the KEGG pathways graphs indicate pathways that are not significantly different from sham.

PDE5-I and PDE9-I mediated miRNA disparities occur at late-stage processing

MicroRNAs are transcribed from the genome and processed from a *pri* to *pre* form in the nucleus by Drosha and DGCR8. The *pre*-miRNA is then exported to the cytosol, and converted to its mature form by Dicer and its partner TRBP, and growing evidence supports kinase signaling control over this process [124]. No study has reported a specific influence of PKG, so we tested whether different miRNA profiles evolve from nuclear or cytosol processing. We focused on a subset of relevant miRNAs (miR-1, 199, 208b, 21a, and 34c), each known to be involved with cardiac hypertrophy and/or fibrosis, and all expressed in cardiomyocytes [104, 125, 126]. *Pre* and *pri*-miRNA levels were similar between treatments (**Figure 2.4A, 2.4B**), whereas differences in expression appeared in the mature miRNA as found by miRNA-seq (**Figure 1.4C**). Thus, the disparity in miRNA profiles from PDE5-I versus PDE9-I in the PO-heart occurred at the level of cytosolic processing.

We further tested if either PDE5 or PDE9 inhibition modifies gene expression of the primary miRNA processing proteins, Argonaute (Ago2), microprocessor complex sub-unit - DGCR8, Dicer1, and Drosha. There were no significant differences in expression for any of these genes between the groups (**Figure 2.4D**).

Figure 2.4: miRNA disparities from different PDE inhibitors occur at late-stage processing

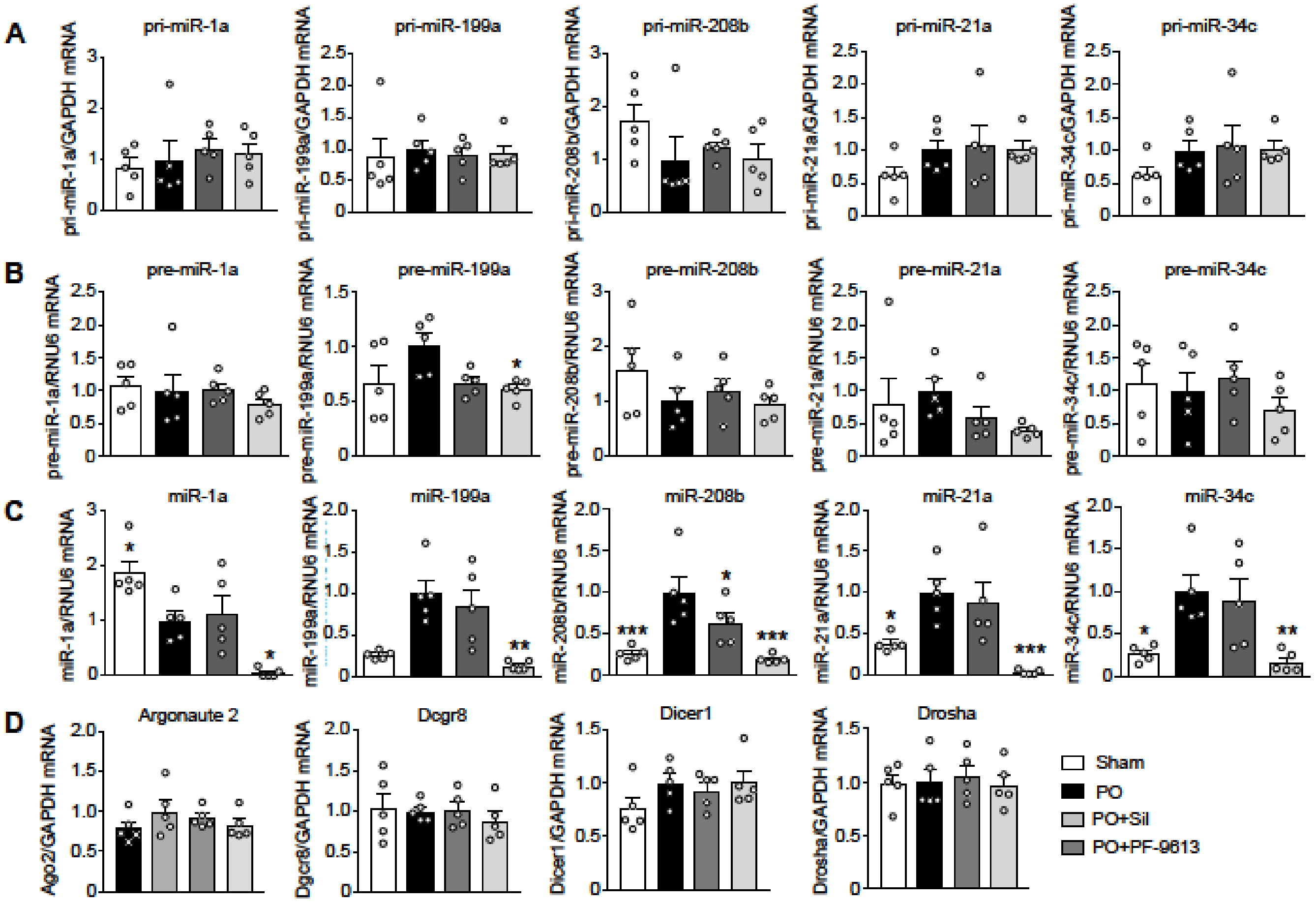

Figure 2.4: miRNA disparities from different PDE inhibitors occur at late-stage processing

A-C) qRT-PCR analysis for **A)** pri-miRNAs, **B)** pre-miRNAs, and **C)** mature miRNAs for a panel of miRNAs selected from the larger sequencing data set that are associated with cardiac hypertrophy and fibrosis (pink diamond miRNAs from Figures 2A, B, and C). **D)** qRT-PCR analysis for miRNA processing genes. Analysis was performed on the same samples used for sequencing analysis (n=5 per group). * $p<0.05$, ** $p<0.01$, *** $p<0.001$, **** $p<0.0001$ as compared to PO. Data is presented as mean ± SEM. Data was analyzed using a one-way ANOVA with a Dunnett post hoc test, or a Kruskal-Wallis test with Dunn's post hoc test.

Effect on miRNAs from alternative stimulation of GC-1 or GC-2A signaling

PDE5-I primarily regulates cGMP generated from GC-1, which is activated by NO. To further test if this pathway is important for broad suppression of miRNAs by PDE5-I, we studied mice exposed to PO and treated with a direct GC-1 activator, BAY 60-2770. BAY 60-2770 treatment also reduces cardiac hypertrophy, fibrosis, and improves function similar to PDE5-I (**Figure 2.5**)[127]. Thirteen miRNAs were assayed, each known to be relevant to pro- or anti-hypertrophic signaling[105-107, 128-139] and divided them into those significantly increased or decreased by PO. Both PDE5-I and GC-1 activation displayed similar reductions of miRNAs that were increased by PO, (p=NS, **Figure 2.6A**). However, among those that declined with PO (anti-hypertrophic miRNAs), PDE5-I further reduced 6 out of 7, whereas GC-1 activation impacted none ($p<0.05$ by Fisher's exact test, **Figure 2.6B**). Thus, triggering PKG by enhancing cGMP synthesis via GC-1 activation or by impeding its hydrolysis by PDE5-I had similar effects on miRNAs positively associated with hypertrophy, but only PDE5-I impacted miRNAs that were anti-hypertrophic. Thus, even different ways of stimulating the same pathway do not guarantee identical miRNA modulation.

As myocardial PDE9 primarily hydrolyzes cGMP coupled to GC-2A [114], an alternative to PDE9-I is to sustain stimulation of this NP-receptor coupled cyclase. We used a genetic model with cardiomyocyte-targeted overexpression of GC-2A, which is also protective against PO induced cardiac hypertrophy [115]. As with PDE9-I, there were minimal changes in pro- or anti-hypertrophic miRNAs in PO-myocardium from GC-2A overexpressors as compared to littermate controls (**Figure 2.6C**).

Figure 2.5: Phenotypic improvement in PO mice following GC-1 activation.

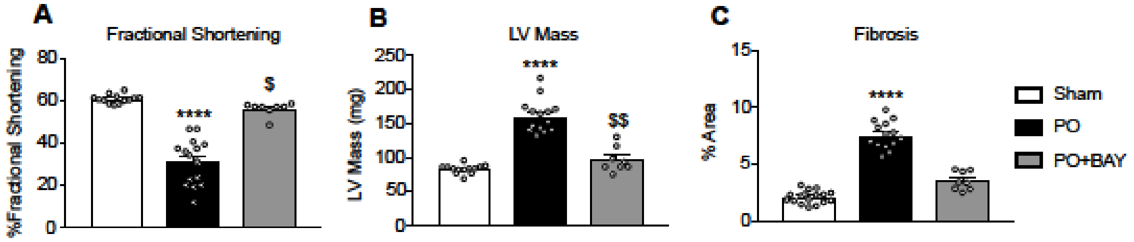

Figure 2.5: Phenotypic improvement in PO mice following GC-1 activation.

C57Bl6/J mice were subjected to sham or PO surgeries. PO mice were subsequently treated with either vehicle or BAY 60-2770 (GC-1 activator) and followed for 3 weeks [127]. **A)** Left ventricular mass. **B)** Fractional shortening. **C)** Fibrosis as quantified by Masson's trichrome stain. All parameters were significantly improved by treatment with BAY 60-2770. **** $p<0.0001$ versus sham. \$ $p<0.05$ versus PO, \$\$ $p<0.01$ versus PO. N=8-15 per group. Data is presented as mean ± SEM. Data was analyzed using a Kruskal-Wallis test with Dunn's post hoc test.

Figure 2.6: Effect on miRNAs from alternative stimulation of GC-1 or GC-2A signaling

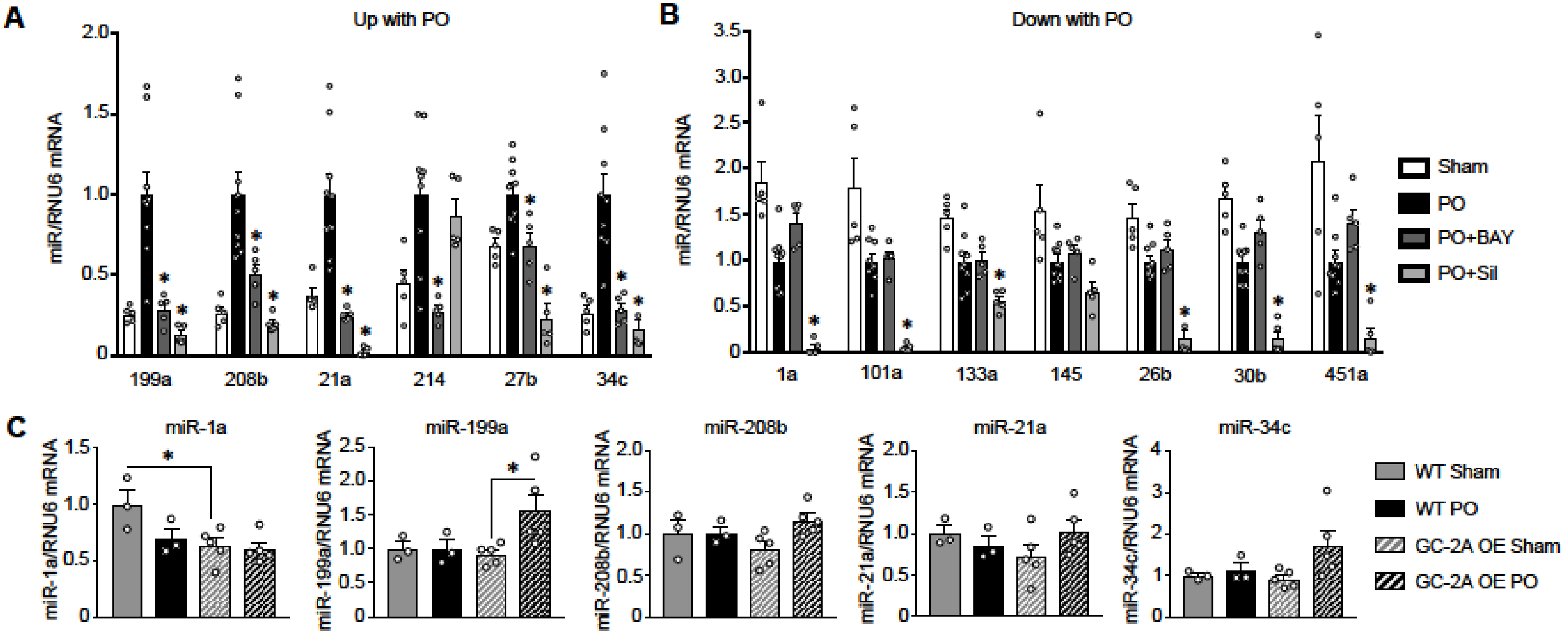

Figure 2.6: Effect on miRNAs from alternative stimulation of GC-1 or GC-2A signaling

A and B) Left ventricle myocardium from mice subjected to sham or PO surgery and subsequently given either vehicle, PDE5-I (Sil), or an sGC activator (BAY 60-2770) were subjected to qRT-PCR analysis for **A)** pro-hypertrophic miRNAs and **B)** anti-hypertrophic miRNAs. Sil downregulates both categories of miRNAs, whereas BAY downregulates only pro-hypertrophic miRNAs. N=4-11 per group. * $p<0.05$ compared to PO for Sil and BAY analysis (smaller p-values are not differentiated by different symbols, though some comparisons were very significant). **C)** Mice overexpressing GC-2A and WT littermate controls were subjected to sham or PO surgery (n=3-5 per group). Myocardial tissue was used for qRT-PCR analysis of miRNAs. * $p<0.05$, ** $p<0.01$, *** $p<0.001$ as compared to indicated group for GC-2A analysis. All data is presented as mean ± SEM. Data was analyzed using a one-way ANOVA with a Dunnett post hoc test, or a Kruskal-Wallis test with Dunn's post hoc test.

PDE5 inhibition in the normal heart and lung does not have the same effect as in diseased hearts

Given the broad impact of PDE5-I on miRNA expression, we wondered if similar effects would be observed under normal conditions or if a stressed or disease state was required. To test this, we exposed C57Bl/6J mice to PDE5-I (sildenafil) for 5 weeks and then assessed a representative panel of 11 miRNAs that all declined with this therapy in the PO heart. Of these, 6 showed significant changes (miR-1a, miR-21a, miR-26b, and miR-27b declined; miR-133a and miR-208b increased), so a majority (64%) were discordant with PO-induced changes (p=0.0039 by Fisher's exact test, **Figure 2.7**).

PDE5-I impacts the enzyme globally, including in the lung where PDE5 expression is prominent [140]. To test if its effects on miRNA expression were organ independent, we examined lungs from normal and PO mice, assaying those known to be highly expressed in lung [141, 142]. All were confirmed as being reduced in PO+PDE5-I myocardium by qPCR and/or miRNA-seq, yet none were altered in lungs by PDE5-I under either condition (**Figure 2.7B, Figure 2.8**). This indicates that PDE5-I does not trigger a pathway broadly suppressing miRNA maturation machinery, as expected if Dicer or associated proteins were inhibited, and its effects are more prominent in the heart and largely depend on the existence of underlying disease.

Figure 2.7: PDE5 inhibition in the normal heart and stressed lung

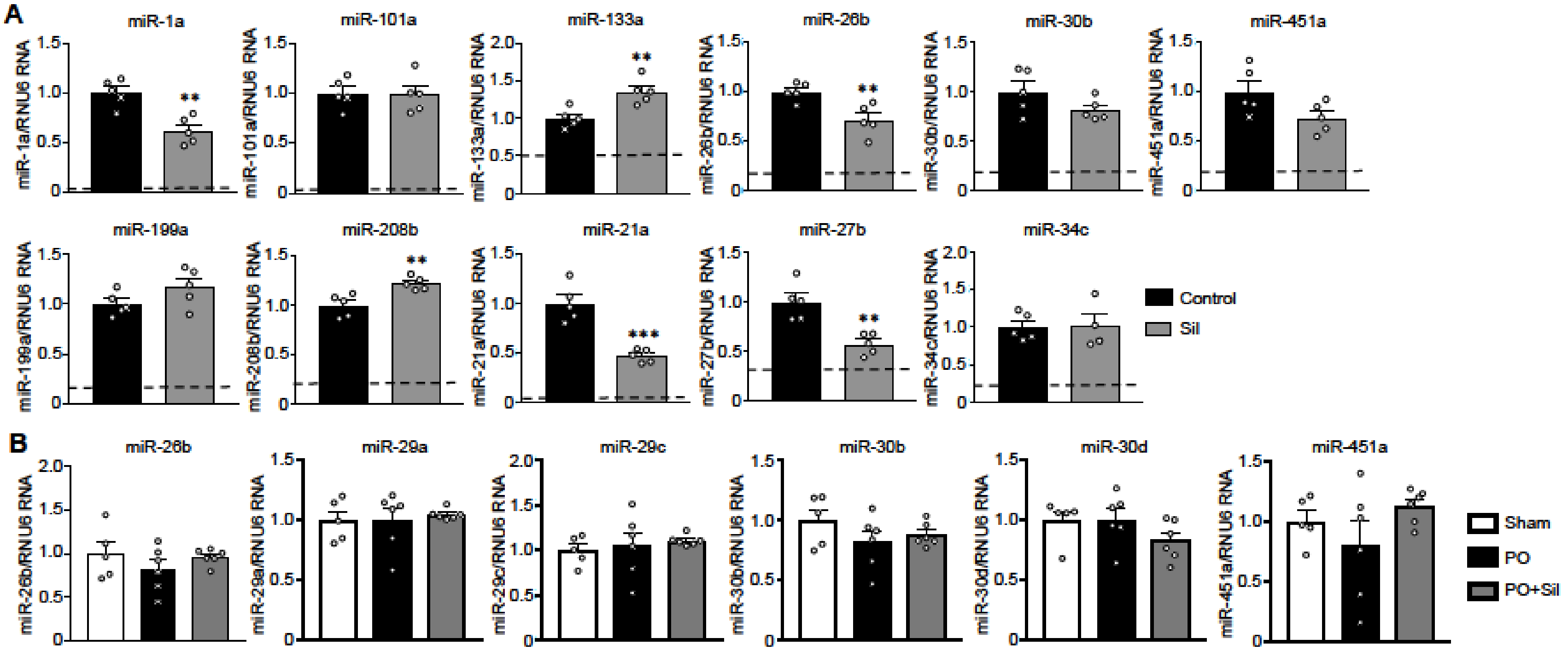

Figure 2.7: PDE5 inhibition in the normal heart and stressed lung

A) qRT-PCR was performed for various miRNAs in tissue from normal, non-stressed C57Bl6/J mice treated with PDE5-I (Sil) for 5 weeks (n=5 per group). Cardiac miRNAs that normally decrease with PO (top row) and increase with PO (bottom row) assessed from left ventricular tissue. Only miRNAs that were significantly decreased by Sil in Figure 4 were assayed. The dashed line on each graph represents the level to which Sil reduced miR expression in the PO model. **B)** Lung tissue from C57Bl6/J mice subjected to PO, PO+PDE5-I (Sil), or sham surgeries was subjected to qRT-PCR for lung miRNAs (n=5-6 per group). * $p<0.05$, ** $p<0.01$, *** $p<0.001$, **** $p<0.0001$ as compared to control for sham Sil heart analysis. Data is presented as mean ± SEM. For A, data was analyzed using two-tailed unpaired t-tests. For B, data was analyzed using a one-way ANOVA with a Dunnett post hoc test, or a Kruskal-Wallis test with Dunn's post hoc test.

Figure 2.8: PDE5-I treatment does not alter miRNA expression in normal mouse lung.

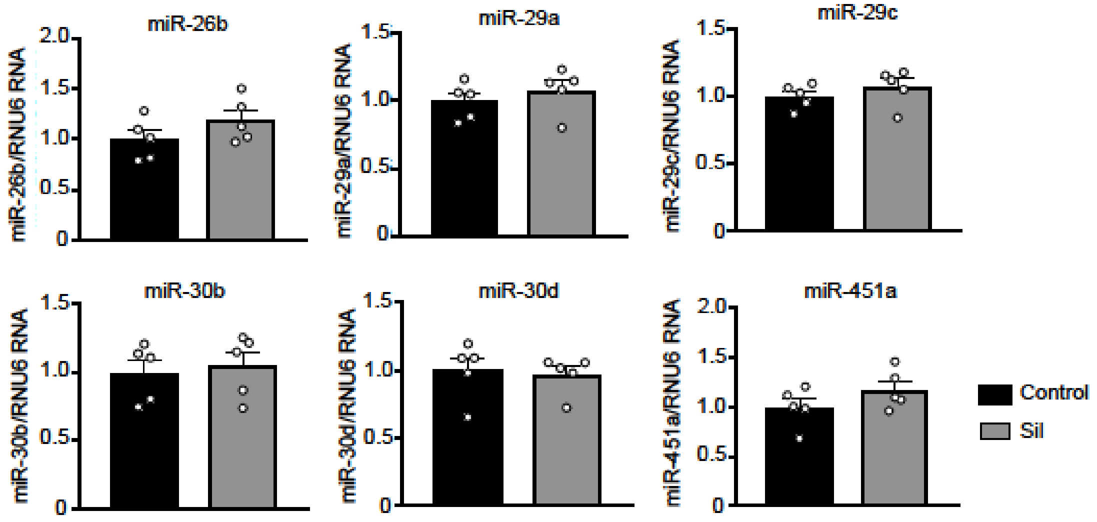

Figure 2.8: PDE5-I treatment does not alter miRNA expression in normal mouse lung.

qRT-PCR was performed for various miRNAs in lung tissue from normal, non-stressed C57Bl6/J mice treated with PDE5-I (Sil) for 5 weeks (n=5 per group). No significant changes were seen with PDE5-I treatment. Data is presented as mean ± SEM. Data was analyzed using two-tailed unpaired t-tests.

DISCUSSION

To our knowledge, this study is the first to directly compare miRNA signatures from very closely related and phenotypically similar therapies (PDE5 and PDE9 inhibition) that both effectively counter the same pathological hypertrophic heart disease by ultimately activating the same protein kinase (PKG). The difference between them lies primarily in the sub-cellular localization of the two PDEs, and this ultimately defines where the effect is actuated. Despite strikingly similar improvement in pressure-overload induced heart disease and many common features of both PDE5-I and PDE9-I, we found nearly opposite effects on miRNA expression, the former suppressing most of them while the latter had virtually no impact.

This study reveals several surprising aspects of miRNAs. First, it shows that their expression can be broadly and potently modified by a clinically widely used pharmaceutical, simultaneously reversing many miRNA changes pathophysiologically relevant to pressure-overload induced heart disease. Importantly, this effect requires pharmaceutical biology in the appropriate intracellular compartment, and cannot be predicted purely based on the protein it affects. Secondly, it dramatically demonstrates that biological conditions that appear phenotypically very similar can have markedly disparate miRNA expression profiles. Lastly, it shows that miRNAs altered by disease do not need to be reversed for a treatment to effectively counter tissue and organ-level pathology and pathophysiology. This poses some quandaries for their use as biomarkers for therapeutic responses.

Both PDE5 and PDE9 inhibition augment cGMP and activate PKG. This kinase activation confers anti-fibrotic and anti-hypertrophic effects by blocking Gq-protein receptor coupled activation [28], and inhibiting transient receptor potential canonical ion channel (type 6) to blunt nuclear factor of activated T-cells and serum response factor regulated gene expression [65, 114, 143]. The pools of PKG activated by either PDE5 or PDE9 inhibition share these properties, but also display downstream phosphorylation profiles unique to each intervention [114]. We found only two prior studies reporting miRNAs altered by PDE5-I. Each involved very different models and did not assess miRNA expression broadly. For example, pig hearts subjected to cardiac arrest and resuscitation had reduced miR-1 and increased miR-133a with sildenafil treatment [144]. Sildenafil reduced miR-1 in the current model as well. The second study examined adipose tissue miRNA expression in type 2 diabetic patients treated with chronic high dose PDE5-I, and found PDE5-I decreased miR-22-3p expression [145]. Again, the model and tissue examined are very different to the present work, and only selective analysis was provided. Our observation that PDE5-I does not simply suppress miRNA levels in normal mice or other non-cardiac tissue from PO mice shows this is not a blanket effect, but more specific to the tissue and condition. We find no reports of miRNA changes with PDE9-I. Furthermore, the results with PDE9-I are unusual in that we also found no reports of a therapy conferring substantial benefits against disease yet with virtually no impact on miRNA signaling coupled with the disease. This does not mean gene transcription is unaltered, just that it is dissociated from miRNA regulation.

PDE5 and PDE9 each preferentially regulate different cGMP pools linked to either NO or NP signaling, respectively. However, we found even targeting presumably the same cGMP pool but by different strategies – e.g. GC-1 activation versus PDE5-I –that miRNA expression profiles consistently differed while organ and tissue level improvement of underlying heart disease was very similar [127]. The specific differences were intriguing, as unlike PDE9-I, or upregulation of the NP-associated GC-2A cyclase, GC-1 activation and PDE5-I both consistently reduce expression of pro-hypertrophic miRNAs that are otherwise increased by PO. However, miRNAs that decline with PO are unaltered by GC-1 activation, but reduced further by PDE5-I. Statistically, this consistent pattern was unlikely due to chance, and shows that regional kinase signaling within the cytosol can yield directionally cohesive changes in miRNA expression. This too may relate to compartment differences between PDE5 and GC-1, with GC-1 residing in both the cytosol and at the plasma membrane [21], whereas PDE5 normally localizes to the sarcomere [64, 114]. PDE5-I can only alter cGMP in the nano-domain in which it is expressed; while GC-1 stimulation generates cGMP that can also be regulated by other PDEs besides PDE5 [146], so their impact is not identical.

The mechanism by which PDE5-I broadly alters miRNA expression in the PO heart remains unknown. Given that *pri-* and *pre-* miRNAs are similar between PDE5-I and PDE9-I, the disparity seems likely to reside at the level of cytosolic Dicer/Argonaute miRNA processing and/or ribonucleases [124]. While gene expression of the relevant proteins was unchanged, this does not preclude their post-translational modification. Our phospho-kinome analysis of both PDE5-I and PDE9-I treatment in PO did not find changes in miRNA processing proteins from either [114], though lack of detection does not mean they do not exist. An example where kinase modulation of miRNA processing occurs is Argonaute 2 phosphorylation by casein kinase-1 alpha1 that broadly impacts miRNA-gene suppression [147]. This study utilized a genomic CRISPR/Cas9 knock-out strategy to identify proteins that blunt miRNA processing. Of note, PKG was not identified in this screen. Furthermore, if PKG had a general effect on Dicer/Argonaute processing, one would expect PDE5-I to suppress miRNA expression in other tissues and conditions (e.g. with or without disease), but this was not observed. Whatever changes PDE5 can induce also appear tissue and condition specific, as similar broad-suppression was not observed in normal hearts or the lung. It is also unlikely that PDE5-I would necessarily ameliorate diseases generated by artificial overexpression of a pathogenic miRNA, or that its expression/activity is altered by such models. Unfortunately, the obvious reductionist model system - isolated cultured myocytes - proved inadequate for replicating miRNA signatures found in vivo. This is likely due to the absence of required environmental cues and stresses present in intact hearts. Mechanistic dissection of the current signaling would appear to require more complex in vivo genetic models where viability is often a limitation.

With respect to why PDE9 inhibitors do not affect miRNA expression in the PO model, this too may relate to where its cGMP modulation occurs. PDE9 functional interaction with natriuretic peptide receptor-coupled cGMP and co-localization with sarcoplasmic reticular membranes suggest compartments removed from cytosolic miRNA processing. It is not due to a failure to get the inhibitor into the myocyte, as we reported potent in vivo and in vitro effects on cGMP signaling from PDE9 inhibition, including effects on anti-fibrotic gene expression and hypertrophy markers, that are absent when the gene for the protein is silenced [114]. As shown here, PDE9-I also has marked effects on gene expression - it just does so without altering miRNAs, and like PDE5-I inhibition, impacts post-translational protein phosphorylation.

In summary, we have shown how dramatically different miRNA expression profiles can be associated with similarly targeted kinase activation strategies that successfully treat the identical heart disease – one broadly suppressing expression while the other leaving it virtually unchanged. The results indicate that improving myocardial and chamber disease phenotype can be achieved without engaging miRNAs, and that with or without this engagement, gene expression impacting similar signaling pathways can still occur. Lastly, we reveal a barcode-like signature provided by miRNA profiles that can distinguish between treatments targeting the same overall pathway. This may provide a useful tool for drug development and precision therapy.

Table 2.1: miRNAs differentially expressed in PO as compared to sham.

Left ventricle myocardium from mice subjected to sham or PO surgery and subsequently given either vehicle, PDE5-I (Sil), or PDE9-I (PF-9613) was subjected to miRNA sequencing and subsequent differential expression analysis (n=5 per group). The log2 fold change and p value are provided for each miRNA, with table sorted by p value.

miRNA ID	log2FoldChange (vs. sham)	p value
mmu-miR-208b-3p	4.177277275	4.15E-69
mmu-miR-455-3p	2.566344072	6.01E-23
mmu-miR-1247-5p	2.245542141	1.16E-19
mmu-miR-199-5p	1.987698664	3.13E-19
mmu-miR-34c-5p	2.081491061	4.76E-18
mmu-miR-21a-5p	1.778120295	1.50E-17
mmu-miR-214-3p	1.846356429	1.62E-15
mmu-miR-214-5p	1.803377612	2.47E-13
mmu-miR-199-3p/mmu-miR-199b-3p	1.531757504	8.96E-13
mmu-miR-146b-5p	1.66286642	1.41E-11
mmu-miR-21a-3p	1.486612606	6.22E-10
mmu-miR-127-3p	1.228474661	1.78E-08
mmu-miR-224-5p	1.282069615	1.17E-07
mmu-miR-199b-5p	1.25544462	2.33E-07
mmu-miR-140-3p	1.149507292	2.39E-07
mmu-miR-34b-5p	1.713965516	1.26E-06
mmu-miR-411-5p	1.093259429	1.40E-06
mmu-miR-1247-3p	2.407271182	6.26E-06
mmu-miR-9-5p	-1.15246671	7.28E-06
mmu-miR-455-5p	-1.125269179	7.29E-06
mmu-miR-298-5p	1.121706324	7.94E-06
mmu-miR-501-5p	1.857763818	2.48E-05
mmu-miR-27b-3p	0.85679754	3.09E-05
mmu-miR-300-3p	0.985183431	4.55E-05
mmu-miR-499-5p	-0.777585635	0.000147302
mmu-miR-410-3p	0.89245254	0.000161098
mmu-miR-497a-5p	0.776615594	0.000174491
mmu-miR-379-5p	0.982619158	0.000271363
mmu-miR-541-5p	0.853822266	0.000285637
mmu-miR-133a-5p	-0.796649968	0.000305674
mmu-miR-92b-3p	0.883212541	0.000384535
mmu-miR-222-3p	0.744534001	0.000496055

mmu-miR-431-5p	0.882820558	0.000496317
mmu-miR-140-5p	0.883350398	0.000507314
mmu-miR-24-3p	0.76897668	0.000551962
mmu-miR-338-3p	-0.837017936	0.000575003
mmu-miR-574-3p	0.798361265	0.000606652
mmu-miR-125b-1-3p	0.812749712	0.000614638
mmu-miR-582-5p	-1.01850343	0.000615216
mmu-miR-135-5p	-0.950045305	0.000621182
mmu-miR-23b-3p	0.719158479	0.000643536
mmu-miR-195-5p	0.723228506	0.000698554
mmu-miR-10a-5p	-0.769965209	0.000984668
mmu-miR-29c-3p	-0.709761981	0.00102143
mmu-miR-329-3p	1.094665852	0.001190208
mmu-miR-30c-1-3p	-0.765860358	0.001248326
mmu-miR-30c-5p	-0.676552634	0.001334222
mmu-miR-874-3p	-0.793623431	0.001440808
mmu-miR-136-5p	0.792994603	0.001450841
mmu-miR-30e-5p	-0.599468785	0.001594309
mmu-miR-30e-3p	-0.605251844	0.001700235
mmu-miR-136-3p	0.863419406	0.002005438
mmu-miR-34b-3p	0.945263719	0.002109153
mmu-miR-99-3p	0.791626989	0.002221577
mmu-miR-10b-5p	0.651387841	0.00242168
mmu-miR-221-3p	0.668772841	0.002702869
mmu-miR-144-3p	-0.791623865	0.002710719
mmu-miR-149-5p	-0.647036271	0.002778003
mmu-miR-208a-3p	-0.658540111	0.002872092
mmu-miR-1a-3p	-0.57678815	0.002904741
mmu-miR-27b-5p	0.677970616	0.00345167
mmu-miR-30c-2-3p	-0.643612613	0.003849693
mmu-miR-1960	-0.875994383	0.003898051
mmu-miR-210-3p	0.64683885	0.004630607
mmu-miR-667-3p	1.204853494	0.004877288
mmu-miR-30b-5p	-0.612743013	0.004952484
mmu-miR-133b-3p	-0.595539655	0.006280098
mmu-miR-483-3p	-0.730210151	0.007147573
mmu-miR-582-3p	-0.601335273	0.008068592
mmu-miR-1964-3p	-0.641278554	0.008245143
mmu-miR-301a-3p	0.60618848	0.008330173
mmu-miR-139-3p	-0.697509549	0.008483423
mmu-miR-195-3p	0.640570655	0.00867885

mmu-miR-184-3p	0.718421494	0.00988326
mmu-miR-200c-3p	-1.144613357	0.010961819
mmu-miR-219-5p	-0.951127563	0.011887967
mmu-miR-154-5p	1.009780507	0.014955031
mmu-miR-132-3p	0.502716542	0.014970729
mmu-miR-99b-5p	0.519732556	0.01554761
mmu-miR-145-3p	-0.510560397	0.015906786
mmu-miR-26b-3p	-0.621098994	0.01596098
mmu-miR-181a-1-3p	-0.466649623	0.018218181
mmu-miR-3098-5p	-0.920489101	0.018330095
mmu-miR-3098-3p	-0.929468531	0.018787963
mmu-miR-501-3p	0.62960178	0.018971356
mmu-miR-328-3p	-0.511540878	0.019431341
mmu-miR-1198-5p	-0.54981481	0.020920779
mmu-miR-30a-3p	-0.441725334	0.02179809
mmu-miR-212-5p	0.593630296	0.0218344
mmu-miR-133a-3p	-0.449577112	0.021989004
mmu-miR-871-3p	-1.15694682	0.022021046
mmu-miR-99-5p	0.53007521	0.022479183
mmu-miR-341-3p	0.716012717	0.02354315
mmu-miR-378a-3p	-0.425598087	0.024202638
mmu-miR-486a-3p	-0.451965148	0.02424837
mmu-miR-134-5p	0.683384586	0.025274159
mmu-miR-331-5p	-0.71529655	0.025670549
mmu-miR-499-3p	-0.614728415	0.025868154
mmu-miR-574-5p	0.564633788	0.027924415
mmu-let-7d-5p	-0.482804262	0.029207826
mmu-miR-532-5p	0.529975705	0.034580381
mmu-miR-100-5p	0.494306994	0.034768324
mmu-miR-141-3p	-0.577602833	0.034852473
mmu-miR-24-1-5p	0.556695732	0.036921798
mmu-miR-152-5p	0.548148402	0.039963989
mmu-miR-409-3p	0.539785248	0.04177907
mmu-miR-187-3p	-0.549552419	0.043913063
mmu-miR-324-5p	0.522237481	0.044598747
mmu-miR-144-5p	-0.51562852	0.047280829
mmu-miR-874-5p	-0.663785168	0.04760991
mmu-miR-185-5p	-0.446271837	0.047679759

Table 2.2: miRNAs differentially expressed in PO+PDE5-I as compared to PO.

Left ventricle myocardium from mice subjected to sham or PO surgery and subsequently given either vehicle, PDE5-I (Sil), or PDE9-I (PF-9613) was subjected to miRNA sequencing and subsequent differential expression analysis (n=5 per group). The log2 fold change and p value are provided for each miRNA, with table sorted by p value.

miRNA ID	log2FoldChange (vs. PO)	p value
mmu-miR-101a-3p	-4.575787696	2.18E-25
mmu-miR-208b-3p	-4.259710819	1.93E-24
mmu-miR-142a-5p	-4.720138559	5.59E-24
mmu-miR-21a-5p	-4.292238301	1.29E-22
mmu-miR-144-3p	-5.079271251	7.17E-20
mmu-miR-136-5p	-4.821509198	1.39E-15
mmu-miR-1a-3p	-3.593613103	5.60E-15
mmu-let-7a-1-3p/mmu-let-7c-2-3p	-4.305815692	1.01E-14
mmu-miR-101b-3p	-3.606449179	4.26E-14
mmu-miR-208a-3p	-3.520515306	9.09E-14
mmu-miR-301a-3p	-3.226350129	1.01E-13
mmu-miR-153-3p	-5.244158568	1.37E-13
mmu-miR-32-5p	-4.019856028	2.90E-13
mmu-miR-126a-5p	-3.466656304	2.95E-13
mmu-miR-148a-3p	-2.994665951	1.62E-12
mmu-miR-190a-5p	-3.733256642	5.83E-12
mmu-miR-340-5p	-3.067304799	5.96E-12
mmu-miR-142a-3p	-3.265370345	5.96E-12
mmu-miR-215-5p	-4.043439658	1.25E-11
mmu-miR-98-3p	-3.786218782	1.30E-11
mmu-miR-455-5p	-3.88221935	2.60E-11
mmu-miR-19-3p	-4.331984183	5.15E-11
mmu-miR-136-3p	-4.061067822	2.93E-10
mmu-miR-450b-5p	-3.780780242	3.25E-10
mmu-miR-322-5p	-2.91301546	5.93E-10
mmu-miR-542-3p	-3.517618215	1.12E-08
mmu-miR-19b-3p	-3.37716808	1.71E-08
mmu-miR-144-5p	-3.185355157	5.68E-08
mmu-miR-145-3p	-2.782872281	7.21E-08
mmu-miR-499-5p	-2.570804953	1.93E-07
mmu-miR-143-3p	-2.574191179	3.80E-07

mmu-miR-29b-3p	-2.783979064	3.84E-07
mmu-miR-15b-3p	-3.274581748	4.08E-07
mmu-miR-199-3p/mmu-miR-199b-3p	-2.258928351	4.19E-07
mmu-miR-30d-3p	-2.819186253	4.36E-07
mmu-miR-335-5p	-3.073154998	4.91E-07
mmu-miR-192-5p	-2.478450318	6.64E-07
mmu-miR-147-3p	-3.445852507	1.61E-06
mmu-miR-329-3p	-2.619721833	2.86E-06
mmu-let-7f-1-3p	-3.073407632	3.04E-06
mmu-miR-29c-3p	-2.297479573	3.32E-06
mmu-miR-146b-5p	-2.297222027	3.65E-06
mmu-miR-201-5p	-3.550553371	4.15E-06
mmu-miR-223-3p	-2.615866479	4.39E-06
mmu-miR-199b-5p	-2.504635063	5.19E-06
mmu-miR-199-5p	-1.763126499	1.15E-05
mmu-miR-1a-1-5p	-3.39147674	1.29E-05
mmu-miR-582-5p	-3.364000211	1.49E-05
mmu-miR-21a-3p	-2.167642629	1.63E-05
mmu-miR-101a-5p	-2.733260511	2.03E-05
mmu-miR-195-5p	-2.148722392	2.58E-05
mmu-miR-135-5p	-3.142603222	2.66E-05
mmu-let-7c-1-3p	-2.510702219	3.54E-05
mmu-miR-411-5p	-1.80305691	4.03E-05
mmu-miR-15-5p	-2.146684268	5.18E-05
mmu-miR-26a-2-3p	-4.061562476	5.30E-05
mmu-miR-451a	-2.15864161	5.35E-05
mmu-miR-30e-5p	-2.153355798	6.19E-05
mmu-miR-3068-3p	-2.165959958	6.52E-05
mmu-miR-488-3p	-2.302146104	6.70E-05
mmu-miR-362-3p	-2.810144748	7.47E-05
mmu-miR-376c-3p	-4.311137398	9.59E-05
mmu-miR-30b-5p	-1.975135773	9.66E-05
mmu-miR-872-5p	-2.407065203	0.000119065
mmu-miR-335-3p	-2.422673274	0.000129716
mmu-miR-26b-5p	-1.940699675	0.00013046
mmu-miR-7a-1-3p	-2.877452256	0.000139076
mmu-miR-218-5p	-2.330485724	0.0001522
mmu-miR-27a-3p	-1.69596849	0.000156031
mmu-miR-24-2-5p	-1.830541263	0.000171641
mmu-miR-483-3p	1.205677818	0.000201253
mmu-miR-676-5p	-2.382599291	0.000254347

mmu-miR-140-5p	-2.06288526	0.000259883
mmu-miR-98-5p	-2.032506534	0.000287761
mmu-miR-16-1-3p	-3.109524923	0.0003418
mmu-miR-27b-3p	-1.742733471	0.0003486
mmu-miR-34b-5p	-2.304392315	0.000361079
mmu-miR-10b-5p	-1.767827241	0.000483953
mmu-miR-34c-5p	-1.607260613	0.000679358
mmu-miR-450a-5p	-2.017319595	0.00089246
mmu-miR-547-3p	-2.324212207	0.001522837
mmu-let-7f-5p	-1.74726319	0.001620898
mmu-miR-582-3p	-1.803396153	0.001629021
mmu-miR-152-3p	-1.798922482	0.001724373
mmu-miR-32-3p	-3.01248029	0.002335911
mmu-miR-376b-5p	-1.934067313	0.002376858
mmu-miR-299-3p	-2.983870311	0.002768105
mmu-miR-106b-5p	-1.856559443	0.003448093
mmu-miR-203-3p	-1.928163717	0.004164814
mmu-miR-3068-5p	-2.051851585	0.004832613
mmu-miR-423-5p	1.427573041	0.005622449
mmu-miR-598-3p	-2.790289114	0.005771312
mmu-miR-1247-3p	1.078058216	0.005816182
mmu-miR-328-3p	1.346733766	0.006049766
mmu-miR-30a-5p	-1.543528495	0.006297692
mmu-miR-148b-5p	-1.389338531	0.006305273
mmu-miR-219-5p	-3.034733728	0.007325161
mmu-miR-501-3p	1.546412839	0.007537389
mmu-miR-744-3p	-1.77447997	0.007649749
mmu-miR-182-5p	-1.465409276	0.007755117
mmu-miR-874-5p	1.249901366	0.008429325
mmu-miR-350-3p	-1.585452909	0.008543687
mmu-miR-152-5p	-1.365001436	0.008651479
mmu-miR-16-2-3p	-1.801419981	0.009177028
mmu-miR-381-3p	-1.521641225	0.009260401
mmu-miR-18a-5p	-2.235746329	0.00999135
mmu-miR-208a-5p	1.342510232	0.01018137
mmu-miR-455-3p	-0.839591689	0.010910983
mmu-miR-411-3p	-1.594941657	0.01213073
mmu-miR-380-3p	-2.819319513	0.013275558
mmu-miR-423-3p	1.263230963	0.013490059
mmu-miR-340-3p	-1.421705584	0.01514416
mmu-miR-150-5p	1.044478629	0.015674139

mmu-miR-125-5p	1.175742371	0.015696524
mmu-let-7d-3p	1.090460392	0.018232638
mmu-miR-26a-5p	-1.317301178	0.018334224
mmu-miR-7236-3p	-2.70124277	0.018645667
mmu-miR-214-5p	-0.967135919	0.018901065
mmu-miR-338-3p	-1.260644787	0.020013995
mmu-miR-148a-5p	-1.394021505	0.020430572
mmu-miR-9-5p	-1.231035575	0.021472458
mmu-miR-744-5p	1.255979317	0.02479594
mmu-miR-93-3p	0.985683796	0.025067739
mmu-miR-92a-3p	1.127560438	0.025076345
mmu-miR-379-5p	-1.558712488	0.025156207
mmu-miR-16-5p	-1.40711933	0.026162994
mmu-miR-490-5p	1.247672271	0.027533408
mmu-miR-7a-5p	-2.331704002	0.02844339
mmu-miR-200c-3p	1.13668089	0.030329734
mmu-let-7g-5p	-1.237526729	0.032344629
mmu-miR-149-5p	0.942728598	0.033806779
mmu-miR-99-3p	-1.167097642	0.034474809
mmu-miR-194-5p	-1.577767761	0.036915266
mmu-miR-141-3p	-1.849075308	0.037001253
mmu-miR-410-3p	-1.135707973	0.038459548
mmu-miR-1981-5p	1.093683482	0.039078004
mmu-miR-24-1-5p	-1.062738184	0.039385136
mmu-miR-31-3p	-2.613782686	0.039462493
mmu-miR-24-3p	-0.981127044	0.040437228
mmu-miR-125b-2-3p	-0.985936937	0.043431362
mmu-miR-330-3p	1.173939541	0.047306434
mmu-miR-15-3p	-1.582116176	0.047921565

Table 2.3: miRNAs differentially expressed in PO+PDE9-I as compared to PO. Left ventricle myocardium from mice subjected to sham or PO surgery and subsequently given either vehicle, PDE5-I (Sil), or PDE9-I (PF-9613) was subjected to miRNA sequencing and subsequent differential expression analysis (n=5 per group). The log2 fold change and p value are provided for each miRNA, with table sorted by p value.

miRNA ID	log2FoldChange (vs. PO)	p value
mmu-miR-486a-3p	-0.852288229	0.000759706
mmu-miR-1247-5p	-0.829164673	0.005017167
mmu-miR-133b-3p	-0.602267066	0.007479807
mmu-miR-208b-3p	-0.726931451	0.012992257
mmu-miR-483-3p	0.678439682	0.017241916
mmu-miR-3098-3p	0.853667319	0.021434169
mmu-miR-144-3p	-0.476077278	0.022872759
mmu-miR-146b-5p	-0.734020656	0.024039032
mmu-miR-501-3p	0.462887415	0.038742158

Table 2.4: Row legends (i.e. miRNA IDs) for the heatmap presented in Figure 1.2D. miRNAs differentially expressed in PO as compared to sham were clustered using Morpheus (Broad Institute) according to rows (miRNA) and columns (samples), or only rows (miRNA) by the one minus Spearman rank coefficient method.

Row Number	miRNA ID
1	mmu-miR-133b-3p
2	mmu-miR-187-3p
3	mmu-miR-1198-5p
4	mmu-miR-133a-3p
5	mmu-miR-149-5p
6	mmu-miR-328-3p
7	mmu-miR-139-3p
8	mmu-miR-874-3p
9	mmu-miR-30c-1-3p
10	mmu-miR-30c-2-3p
11	mmu-let-7d-5p
12	mmu-miR-874-5p
13	mmu-miR-1964-3p
14	mmu-miR-200c-3p
15	mmu-miR-331-5p
16	mmu-miR-1960
17	mmu-miR-378a-3p
18	mmu-miR-181a-1-3p
19	mmu-miR-486a-3p
20	mmu-miR-3098-3p
21	mmu-miR-3098-5p
22	mmu-miR-483-3p
23	mmu-miR-871-3p
24	mmu-miR-185-5p
25	mmu-miR-141-3p
26	mmu-miR-144-5p
27	mmu-miR-144-3p
28	mmu-miR-208a-3p
29	mmu-miR-219-5p
30	mmu-miR-133a-5p
31	mmu-miR-30c-5p
32	mmu-miR-145-3p

33	mmu-miR-30b-5p
34	mmu-miR-1a-3p
35	mmu-miR-135-5p
36	mmu-miR-29c-3p
37	mmu-miR-30e-5p
38	mmu-miR-499-5p
39	mmu-miR-499-3p
40	mmu-miR-26b-3p
41	mmu-miR-30a-3p
42	mmu-miR-30e-3p
43	mmu-miR-455-5p
44	mmu-miR-338-3p
45	mmu-miR-9-5p
46	mmu-miR-212-5p
47	mmu-miR-134-5p
48	mmu-miR-409-3p
49	mmu-miR-184-3p
50	mmu-miR-132-3p
51	mmu-miR-23b-3p
52	mmu-miR-1247-3p
53	mmu-miR-140-3p
54	mmu-miR-1247-5p
55	mmu-miR-298-5p
56	mmu-miR-221-3p
57	mmu-miR-222-3p
58	mmu-miR-127-3p
59	mmu-miR-125b-1-3p
60	mmu-miR-214-3p
61	mmu-miR-195-3p
62	mmu-miR-574-5p
63	mmu-miR-92b-3p
64	mmu-miR-324-5p
65	mmu-miR-501-3p
66	mmu-miR-99b-5p
67	mmu-miR-574-3p
68	mmu-miR-501-5p
69	mmu-miR-667-3p
70	mmu-miR-10a-5p
71	mmu-miR-10b-5p
72	mmu-miR-136-3p
73	mmu-miR-136-5p

74	mmu-miR-195-5p
75	mmu-miR-140-5p
76	mmu-miR-199b-5p
77	mmu-miR-21a-5p
78	mmu-miR-301a-3p
79	mmu-miR-21a-3p
80	mmu-miR-27b-5p
81	mmu-miR-152-5p
82	mmu-miR-27b-3p
83	mmu-miR-146b-5p
84	mmu-miR-24-3p
85	mmu-miR-99-5p
86	mmu-miR-208b-3p
87	mmu-miR-411-5p
88	mmu-miR-199-3p/mmu-miR-199b-3p
89	mmu-miR-99-3p
90	mmu-miR-34b-5p
91	mmu-miR-379-5p
92	mmu-miR-24-1-5p
93	mmu-miR-582-3p
94	mmu-miR-582-5p
95	mmu-miR-329-3p
96	mmu-miR-154-5p
97	mmu-miR-100-5p
98	mmu-miR-224-5p
99	mmu-miR-214-5p
100	mmu-miR-199-5p
101	mmu-miR-34c-5p
102	mmu-miR-300-3p
103	mmu-miR-34b-3p
104	mmu-miR-410-3p
105	mmu-miR-497a-5p
106	mmu-miR-341-3p
107	mmu-miR-210-3p
108	mmu-miR-431-5p
109	mmu-miR-541-5p
110	mmu-miR-532-5p
111	mmu-miR-455-3p

CHAPTER 3: Identification of PDE9 binding partners in cardiomyocytes via co-immunoprecipitation

INTRODUCTION

Phosphodiesterases are highly compartmentalized enzymes that tightly control cyclic nucleotide levels in local nanodomains. In cardiomyocytes, many different phosphodiesterase isoforms have been studied, with PDE3 and PDE4 primary among them. One of the normal functions of these two PDEs is to maintain a gradient of cAMP from the plasma membrane, where it is produced by adenylyl cyclase, to the sarcoplasmic reticulum, where it can interact with and activate PKA. It has been shown, however, that this shuttling is lost in heart failure due to relocalization of the PDEs and subsequent diffusion of cAMP away from the gradient, leading to a loss of signaling between the β-adrenergic receptor and the sarcoplasmic reticulum[40]. Similarly, our lab has shown that PDE5, which regulates cGMP, relocalizes from the sarcomere Z-disc to the cytoplasm in the presence of cardiac pressure-overload, dilated heart failure[72], or following pharmacological or genetic blockade of nitric oxide synthase, resulting in a switch of its normal control of nitric oxide-derived cGMP to that of natriuretic peptide-derived cGMP[71, 73]. PDE9 is also cGMP selective, which as recently reported[48, 148], confers functionally different control over cGMP and consequent PKG activation in the heart. In particular, PDE9 hydrolyzes natriuretic peptide derived cGMP, so the capacity to activate PKG upon its inhibition is independent of nitric oxide synthesis.

PDE5 and PDE9 are different in their preferred substrate pool and localization, as well as in their current clinical applications. Both PDEs are cGMP-specific, although PDE9 has a higher specificity for cGMP than does PDE5. Highly-specific inhibitors for both PDEs exist, with PDE5 inhibitors primarily being used to treat erectile dysfunction and pulmonary hypertension. PDE5 inhibitors have been tested in heart failure with preserved ejection fraction in the RELAX trial with neutral results. This outcome is hypothesized to be due to low cGMP and PKG activation without concomitant increases in PDE5 expression, thereby limiting the impact of PDE5 inhibitor treatment. PDE9 inhibitors have been tested in Alzheimer's, Parkinson's, and schizophrenia, although pre-clinical and early stage clinical trials for cardiac indications are underway. PDE5 regulates NO-derived cGMP, though it switches to regulation of NP-derived cGMP when it shifts to a cytoplasmic localization. PDE9 has recently been shown to specifically regulate NP-derived cGMP. In cardiomyocytes, PDE5 normally localizes to the Z-disk, whereas PDE9 localizes to the T-tubular membrane. Under some conditions, PDE5 relocalizes to become cytoplasmic; however, PDE9 is not currently known to change localization under differing conditions. However, beyond the limited confocal images available identifying different localization of PDE5 versus PDE9 in the cardiac myocyte, nothing is known about the cluster of proteins with which PDE9 interacts, how this differs from PDE5, and whether like PDE5, PDE9 undergoes intracellular redistribution following pathological stress.

One way to study protein compartmentalization is by co-immunoprecipitation followed by mass spectrometry, allowing for identification of PDE binding partners and complexes. This does require having either an excellent antibody or a tagged PDE for high efficiency pulldown, but can be performed with relative ease under multiple conditions (i.e. basal versus disease). Our lab has previously performed this experiment for PDE5 by pulling down FLAG-tagged PDE5 from myocardium derived from a cardiomyocyte-specific PDE5 overexpressor mouse. However, as a mouse expressing a tagged PDE9 does not currently exist, and there are few reliable antibodies for PDE9, we opted to take the approach of introducing adenovirus expressing FLAG-tagged PDE9 to isolated adult rabbit cardiomyocytes. By using this system variance can be reduced, as multiple conditions can be tested within cardiomyocytes from a single animal. Additionally, rabbit cardiomyocytes express relatively similar PDEs to those found in the human, making them an ideal model system. In this experiment, we aimed to identify the compartment within which PDE9 resided in both normal and hypertrophic conditions.

METHODS

Plasmids and adenovirus: pAdLox-PDE9-FLAG was constructed by Mike Sasaki. AdPDE9-FLAG and adFLAG were generated by Welgen, Inc (Worcester, MA).

Adult rabbit myocyte isolation and infection: Adult rabbit myocytes were isolated as previously described[149]. Myocytes were infected with adenovirus (10 MOI) at the time of plating in Medium 199 (Sigma). After 3-4 hours, media was changed to Medium 199 containing 2% FBS, penicillin-streptomycin (100 U/mL), L-glutamine (0.1 mg/mL), creatine (5 mM), taurine (5 mM), and L-carnitine (2 mM). After overnight incubation, cells were stimulated with endothelin-1 (100 nM, Sigma) or vehicle for 24 hours in Medium 199 containing penicillin-streptomycin, L-glutamine (0.1 mg/mL), creatine (5 mM), taurine (5 mM), and L-carnitine (2 mM).

Immunofluorescence: Cells were transduced as described. After 48 hours of viral construct expression, cells were fixed in 10% formalin in PBS, permeabilized with 0.5% saponin in PBS, and blocked with 3% BSA in PBS. Cells were then stained overnight in 3% BSA with

0.5% saponin in PBS at 4°C for FLAG (F1804, Sigma, 1:200 or 14793, Cell Signaling, 1:200) or SERCA2A (MA3919, ThermoFisher, 1:100). Cells were then counterstained with anti-rabbit Alexa 568 and anti-mouse Alexa 488-coupled secondary antibody (ThermoFisher) at a 1:500 dilution. Hard-mount Vectashield with DAPI (Vector Labs) was used to preserve fluorescence after staining was complete. Imaging was performed on a Leica TCS SPE confocal microscope using a 40X oil-immersion objective.

Immunoprecipitation of FLAG-tagged Proteins: Adult rabbit cardiomyocytes were infected as described. After samples were collected, they were sonicated to disrupt cell membranes and spun down. Protein concentration was measured using the Pierce bicinchoninic acid (BCA) protein assay (ThermoFisher). For immunoprecipitation, 100 µL of FLAG M2 magnetic beads (Sigma) were pre-washed twice with TBS and then incubated with 400 µg of protein. Beads were rotated with lysate overnight at 4°C. Following incubation, beads were washed three times with TBS. Elution was performed by rotating the beads with a 3X FLAG peptide solution twice for 30 minutes each at 4°C.

Western blotting: After immunoprecipitation was performed, both input and eluate samples were run under reducing and denaturing conditions on precast 4-20% Mini-PROTEAN Tris-Glycine TGX gels (Bio-Rad). Following semi-dry transfer to nitrocellulose membranes, blotting was performed for PDE9 (custom antibody, ProSci Inc, 1:1000), FLAG (F1804, Sigma, 1:1000), or VDAC2 (ab37985, Abcam, 1:1000). LI-COR secondary antibodies were used for detection at a 1:10,000 dilution, and membranes were imaged on a LI-COR Odyssey using Image Studio v5.0 software. Total protein staining for normalization was performed using the LI-COR REVERT staining kit.

Mass Spectrometry Experimental Design: For FLAG co-immunoprecipitation studies, adult rabbit cardiomyocytes were isolated and cells were infected with one of two viruses: adFLAG or adPDE9-FLAG. Within each virus group, samples were either with ET-1 (100 nM, Sigma) or vehicle, for a total of two samples per virus group. The experiment was repeated with n=3 rabbits for a total of three independent experiments. Tandem mass tag labels were shuffled between samples in different multiplexes to minimize peptide labeling bias (see below).

Mass Spectrometry Peptide Preparation: Following sample elution from FLAG magnetic beads, methanol-chloroform extraction was performed for all samples according to the methods of Wessel and Flugge[150]. After extraction was complete, samples were resuspended in 9M urea containing 10 mM Tris-HCl, and subsequently diluted 1:6 in 60 mM HEPES pH 7.5, and 0.6 mM DTT, to yield a final digestion buffer containing 50 mM HEPES, pH 7.5 1.5M urea, and 0.5 mM DTT. 1 μg of trypsin/Lys-C (Promega V5073) was added to each sample, and peptide digest proceeded overnight at 25°C (to reduce lysine carbamylation) with samples shaking at 1050 RPM. The next day, another 0.5 μg of trypsin was added along with 5 mM DTT, and digest continued for another 2 hours. 20 mM iodoacetamide was then added to alkylate the samples for 1 hour in the dark. 0.5% v/v TFA was added to acidify the peptides, which were then purified on C18 spin columns (Pierce) according to manufacturer's instructions and eluted using 0.1% formic acid in 60% acetonitrile. Finally, samples were evaporated to dryness in an Eppendorf Vacufuge. Distilled deionized H_2O was added after the first spin and samples were subjected to a second round of evaporation to remove trace levels of formic acid and acetonitrile.

Peptide Labeling and 2-Dimensional Liquid Chromatography Coupled to Tandem Mass Spectrometry (2D-LC-MS/MS): Samples were then resuspended in triethylammonium bicarbonate pH 8.5. Peptides were labeled with TMT (tandem mass tag) reagents (ThermoFisher), with labels shuffled between samples on different multiplexes to minimize labeling bias. TMT labeling was done with samples brought up in 100 µl TEAB and labels brought up in 41 µL anhydrous acetonitrile. Each label was added to its corresponding sample for 1 hour before being quenched with 8 µL of 5% hydroxyl amine for 15 minutes. Samples were then mixed and dried down and subsequently brought up in 2 mL of 10 mM TEAB and injected onto an Agilent LC running a 2.1 x 100 mm Waters BEH C18 column with 1.7 µM particles at 250 µL/minute. The first 12 fractions were flow-through, with the next 84 samples collected on an 85-minute gradient from 0-90% acetonitrile containing 10 mM TEAB. These 84 fractions were concatenated into 12 fractions for LC-MS/MS analysis.

LC-MS/MS was performed on an Orbitrap Fusion Lumos Tribrid Mass Spectrometer (ThermoFisher). Liquid chromatography was performed prior to MS/MS by bringing samples up in buffer A (2% acetonitrile, 0.1% formic acid 98% deionized water), and then injecting the sample onto a trapping column in buffer A for 5 minutes at 5 µL/min before switching to the analytical column (Reprosil C18 3 µM particles with 100 angstrom pore size, packed approximately 20 cm with 75 µM internal diameter fused silica PicoFrits from New Objective (Woburn, MA)) at 300 nL/min. The solution was then switched to 10% buffer B (90% acetonitrile/10% deionized water and 0.1% formic acid). The gradient then went from 10% to 20% buffer B over 45 minutes and then to 35% at 77 minutes before jumping to 100% buffer B at 80 minutes, holding for 2 minutes, then returning to 2% buffer B in another 2 minutes before the liquid chromatography run ended at 90 minutes. The fractions were injected consecutively following this gradient scheme.

MS was conducted with the following instrument settings. MS1 resolution was set to 120,000 with a target ion count of 400,000. The precursor ion isolation width was 0.7 Daltons. For MS2, resolution was set to 50,000 with a target ion count of 100,000. Collision energy was set to 38. Easy IC internal calibration was used on the precursors which uses the ETD ion for mass correction on-the-fly for MS.

Protein Identification: Peak list files (.RAW) were searched against a rabbit database of predicted protein sequences (NCBI RefSeq, taxonomy: Oryctolagus cuniculus, 2018, FASTA format, 38559 sequences; RefSeq83_Oryctolagus_cuniculus_180413_1.fasta;), using Mascot Version: 2.2.0 (Matrix Science) interfaced through Proteome Discoverer 1.4 (Thermo). Peaks were filtered at a signal to noise ratio of 1.5, deisotoped, and searched with a parent ion mass tolerance of 10 ppm and an MS2 mass tolerance of 0.02 Da. Trypsin was specified as the enzyme and 1 missed cleavage was allowed. Cysteine carbamidomethylation and N-terminal amine labeling with TMT 10-plex reagent were specified as fixed modifications for the database search. Dynamic modifications included N-pyroglutamine, oxidized methionine, phosphorylation of serine, threonine, and tyrosine, and TMT labeling of lysine. All searches were conducted with the reversed database search mode engaged. Percolator software was used for peptide FDR (q-value) calculations. Mascot output files (.dat) tabulated were in Proteome Discoverer. Of the high confidence peptides ($q < 0.01$), 2% of unique spectra had intensities missing from one or more channels, indicative of efficient TMT labeling and fragmentation. Spectra for which peptide co-isolation interference was >51% were omitted from analysis. Proteins identified by single spectra were likewise omitted.

Protein Quantification by TMT and Statistical Analysis: TMT reporter ion intensities were integrated over 30 ppm using the most confident centroid method and corrected for purity in Proteome Discoverer 1.4 (Thermo). Missing labeled channel intensities (<2% of spectra) were inversely proportional to the untransformed median ion intensities across the channels. For individual spectra for which missing data was <50%, the missing value was replaced by the median value of the lowest intensities in each channel. Following missing value imputation, these signals were quantified using the median sweep algorithm originally described by Herbrich et al[151] essentially as implemented recently by Foster et al[152] with a minor modification. TMT reporter ion intensities were 1) logarithmically-transformed (base 2), 2) quantile-normalized for each channel, 3) median-centered for each individual spectrum across channels, 4) protein abundance determined by taking the median value of the logarithmically-transformed median-centered intensities for all spectra belonging to that protein in a given channel, and finally, 5) re-centered for each channel by subtracting the median protein abundance. Following the median sweep, differential protein abundance between experimental groups was assessed by means of an empirical Bayesian method, specifically, linear modeling of microarrays (LIMMA)[153, 154] with multi-group comparison, as implemented in Omics Explorer (Qlucore, Lund, Sweden). Resulting p-values were corrected for multiple comparisons using the false discovery rate (q-value) method of Benjamini-Hochberg[155].

Pathways analysis: Pathways analysis for mass spectrometry data was performed using DAVID Bioinformatics Resources[156]. For DAVID analysis, KEGG pathways were used with default analysis parameters. Pathways analysis was also performed with Ingenuity Pathways Analysis software (Qiagen) using default parameters.

RESULTS

PDE9 is enriched in samples overexpressing PDE9-FLAG, seen both by Western blotting and mass spectrometry

After rabbit myocyte lysates from cells transduced with either adFLAG or adPDE9-FLAG underwent immunoprecipitation, both inputs and eluates were run on SDS-PAGE gels to evaluate the effectiveness of overexpression and pulldown. Results show that PDE9 is overexpressed in input samples and enriched in immunoprecipitated samples (**Figure 3.1**). Furthermore, when mass spectrometry data was analyzed, PDE9 was found to be significantly enriched in the adPDE9-FLAG samples as compared to adFLAG controls, with approximately 4-fold increase (**Table 3.1**).

Figure 3.1: PDE9 is enriched in adPDE9-FLAG transduced adult rabbit cardiomyocytes

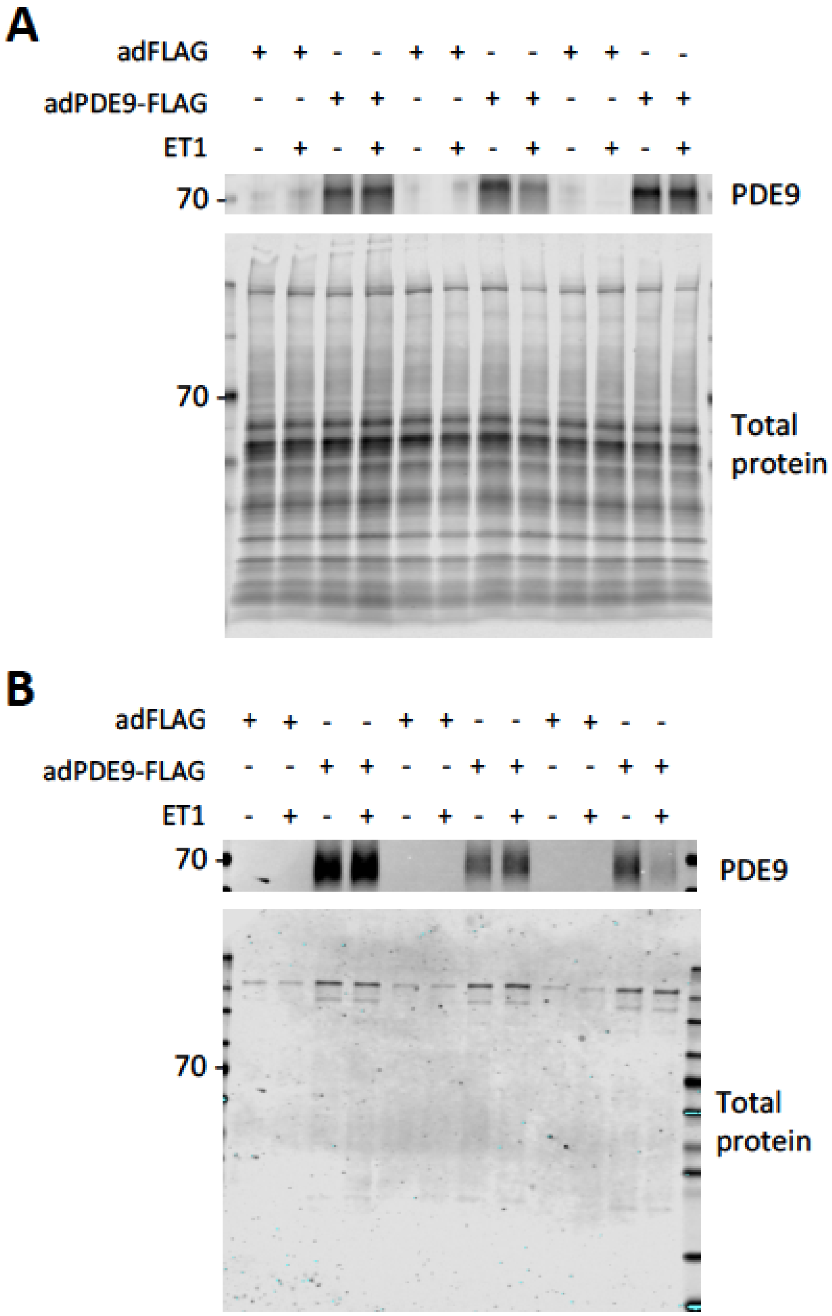

Figure 3.1: PDE9 is enriched in adPDE9-FLAG transduced adult rabbit cardiomyocytes

Adult rabbit cardiomyocytes were transduced with either adFLAG or adPDE9-FLAG, then stimulated with 100 nM ET-1 or vehicle for 24 hours. Samples underwent immunoprecipitation for FLAG, and after elution, both inputs and eluates were subjected to SDS-PAGE and subsequent Western blotting for FLAG and total protein. A) Input samples, and B) eluate samples. Abbreviations: ET-1, endothelin-1.

PDE9 associates primarily with mitochondrial proteins, but also sarcoplasmic reticulum proteins

Mass spectrometry data was analyzed by comparing adPDE9-FLAG samples to adFLAG samples (**Table 3.1**). From this analysis, 155 proteins were found to be significantly enriched in the PDE9-FLAG samples ($p<0.05$). These proteins were then subjected to DAVID KEGG pathways analysis. The enriched pathways were predominantly mitochondrial in nature, including oxidative phosphorylation, citric acid cycle, and fatty acid metabolism (**Table 3.2**). These findings were confirmed by IPA pathways analysis as well (**Figure 3.2**). Sarcoplasmic reticulum and sarcomeric proteins were also significant among the proteins enriched with PDE9, noted as calcium signaling and cardiac muscle contraction pathways in the DAVID analysis.

Figure 3.2: IPA pathways analysis of proteins significantly enriched in PDE9-FLAG samples shows many mitochondrial proteins

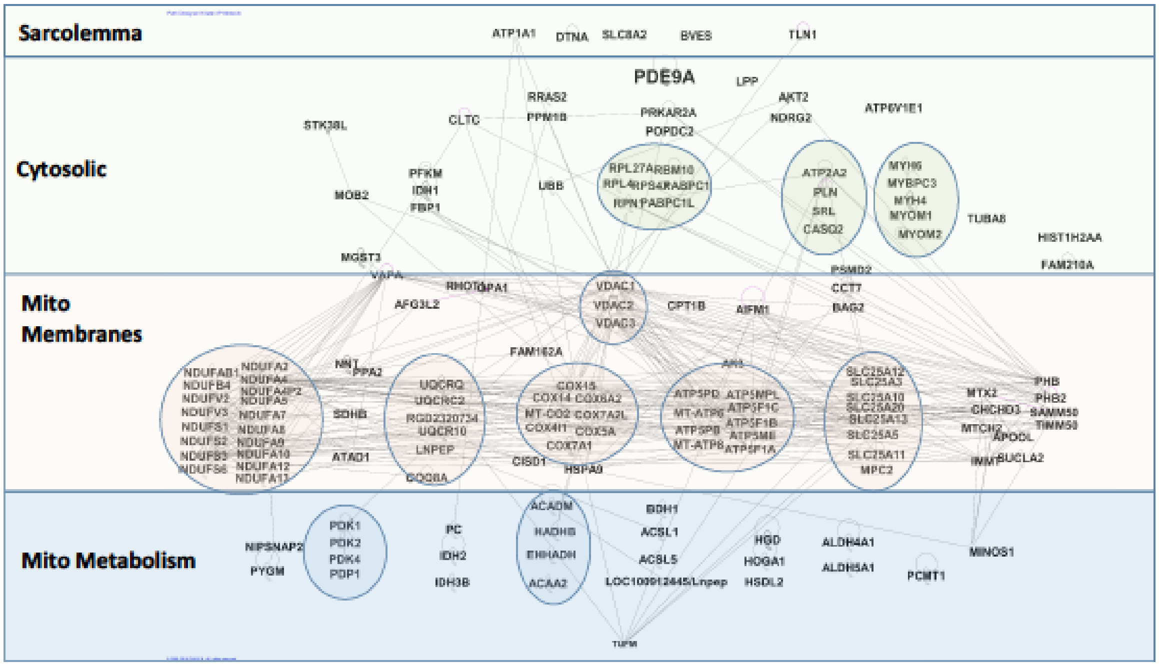

Figure 3.2: Mitochondrial proteins are enriched in PDE9-FLAG pulldowns

Proteins that were significantly enriched ($p<0.05$) in adPDE9-FLAG mass spectrometry samples as compared to adFLAG were subjected to IPA pathways analysis. The resulting protein interaction network is shown here.

PDE9 does not relocalize following ET-1-stimulated hypertrophy

After initial analysis of the mass spectrometry data, we next wanted to determine whether or not PDE9 relocalizes following cardiac hypertrophy. Rabbit myocytes were stimulated to hypertrophy by applying 100 nM ET-1 for 24 hours in serum-free media. After comparison of adPDE9-FLAG to adPDE9-FLAG+ET-1 groups, a total of 97 proteins were identified as significant. When the 46 proteins that were significantly decreased with ET-1 treatment (**Table 3.3**) were subjected to DAVID pathways analysis, oxidative phosphorylation and metabolic pathways were identified (p values of 2.44E-18 and 2.06E-9, respectively); however, many other mitochondrial proteins were still identified in the ET-1 treatment group. This indicates there is likely no significant relocalization of PDE9 following induction of hypertrophy, although there may be some dissociation from oxidative phosphorylation complexes. Of the 51 proteins that were enriched with ET-1 treatment (**Table 3.4**), no significant pathways were identified. All of these proteins were novel to the PDE9-FLAG+ET-1 group (i.e. were not significant when PDE9-FLAG was compared to FLAG control samples).

PDE9 colocalizes with SERCA2a

Rabbit myocytes were transduced with adPDE9-FLAG and subsequently subjected to immunofluorescent staining with SERCA2A and FLAG antibodies. Confocal imaging showed that PDE9 colocalizes with SERCA2A under both normal and ET-1-stimulated conditions (**Figure 3.3**), validating the mass spectrometry finding. We similarly showed in 2015 that PDE9 colocalizes with SERCA2A in isolated adult mouse cardiomyocytes[48].

Figure 3.3: PDE9 colocalizes with SERCA2a in adult rabbit cardiomyocytes

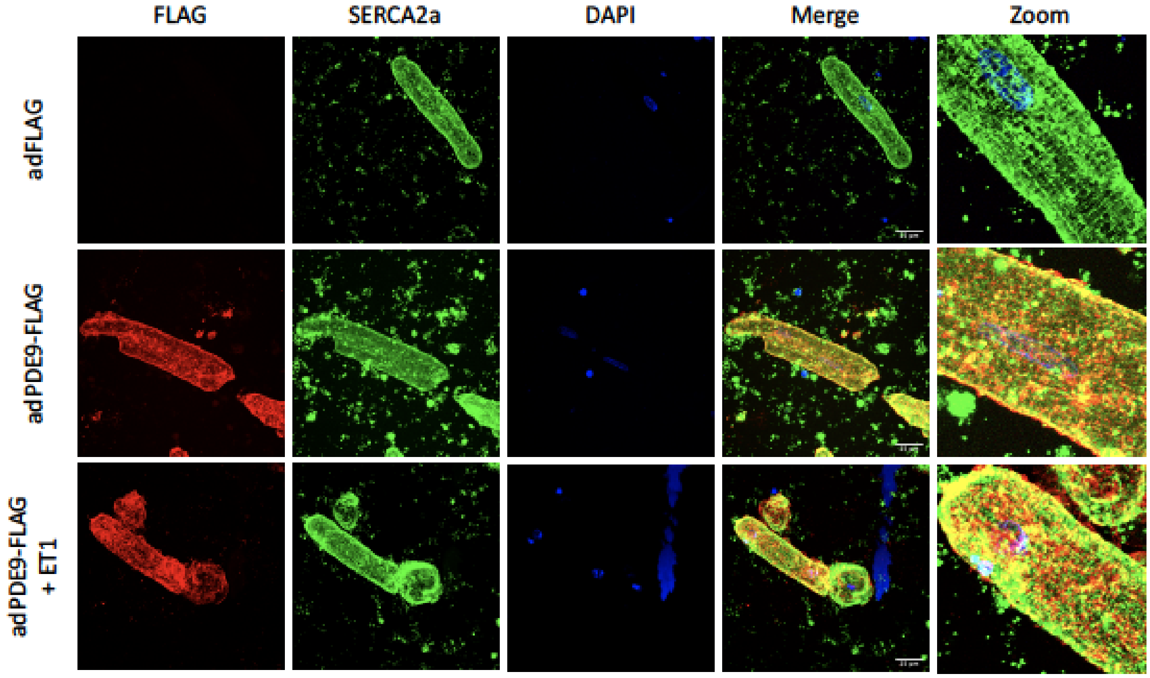

Figure 3.3: PDE9 colocalizes with SERCA2a under basal and hypertrophic conditions

Adult rabbit cardiomyocytes were transduced with adFLAG or adPDE9-FLAG, and then treated with 100 nM ET-1 or vehicle. Cells were fixed and stained for FLAG and SERCA2a, and subjected to confocal microscopy. PDE9 colocalizes with SERCA2a under both hypertrophic and basal conditions.

PDE9 co-immunoprecipitates with VDAC2

VDAC2 is a mitochondrial outer membrane pore protein that was highly enriched in the PDE9-FLAG samples (3.78 fold). To validate this finding, rabbit myocytes transduced with either adPDE9-FLAG or adFLAG and treated with either vehicle or ET-1 were subjected to immunoprecipitation for FLAG and subsequent Western blotting for VDAC2. Both adPDE9-FLAG groups showed enrichment of VDAC2 (**Figure 3.4**), which aligned with our mass spectrometry data showing that VDAC2 bound to PDE9 under both basal and hypertrophic conditions (**Tables 3.1, 3.3, and 3.4**).

Figure 3.4: PDE9 binds to VDAC2 in adult rabbit cardiomyocytes

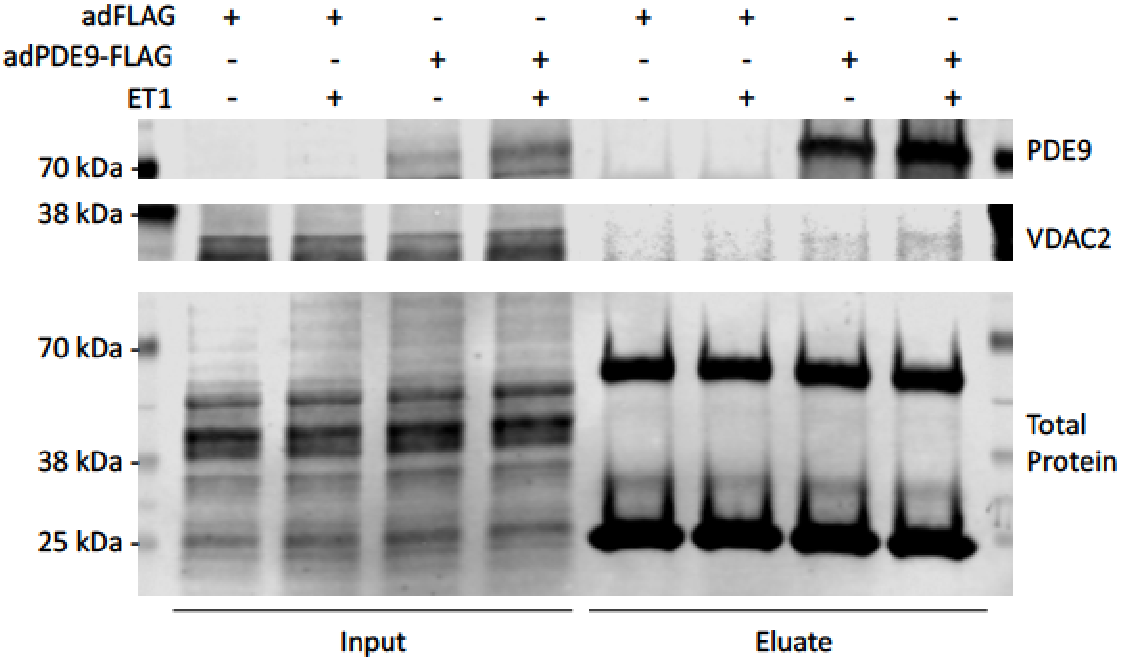

Figure 3.4: PDE9 binds VDAC2 under both basal and hypertrophic conditions
Adult rabbit cardiomyocytes were transduced with adFLAG or adPDE9-FLAG, and then treated with either vehicle or 100 nM ET-1. Samples were collected and underwent immunoprecipitation for FLAG, followed by Western blotting for FLAG, VDAC2, and total protein. Input samples are on the left, and eluates are on the right.

DISCUSSION

This study represents the first in-depth exploration of PDE9 compartmentation in cardiac myocytes. Initial studies from our lab indicated PDE9 was likely localized to mitochondria, which this mass spectrometry data set has confirmed. We also previously showed colocalization with SERCA2a in mouse adult myocytes, which was also seen in this co-IP data set. Previous studies examining cGMP at mitochondria have shown that there is indeed a mitochondrial pool of cGMP[157], which is responsible for activating cardiomyocyte apoptosis via release of cytochrome C in a mitochondrial permeability transition-independent fashion[158]. cGMP has also been shown to promote ATP synthesis and mitochondrial biogenesis by several different groups[159, 160]. However, these studies were performed using NO-pathway targeting reagents, so the role of natriuretic peptide-derived cGMP at mitochondria is unclear. However, in one of these studies, it was determined that a pool of PKG was present at the mitochondria which mediated the apoptotic effects of cGMP in a Ca^{2+} dependent manner[161]. It is possible that PDE9 acts to regulate this pool of cGMP and subsequently PKG activity, thereby preventing cardiomyocyte apoptosis and a shift towards increased ATP synthesis and mitochondrial biogenesis under high cGMP conditions.

Natriuretic peptide protective signaling has been linked to mitochondria in the diseased heart, where it blocks the mitochondrial calcium uniporter[162], inhibits mitochondrial ROS production and subsequent Ca^{2+} leak from the SR[163], and prevents the mitochondrial permeability transition pore from opening[164]. How PDE9 fits in to these protective benefits is unknown, and remains to be determined.

Table 3.1: Proteins significantly enriched in adPDE9-FLAG as compared to adFLAG mass spectrometry samples.

Mass spectrometry samples were analyzed using LIMMA, comparing adFLAG to adPDE9-FLAG. All proteins with $p<0.05$ are shown.

Gene Name	Protein Name	P Value	Ratio PDE9-FLAG/FLAG
UQCR10	Cytochrome b-c1 complex subunit 9	2.01E-05	4.91
NDUFS3	NADH dehydrogenase [ubiquinone] iron-sulfur protein 3, mitochondrial	2.35E-05	2.76
NDUFA5	NADH dehydrogenase [ubiquinone] 1 alpha subcomplex subunit 5	3.51E-05	2.40
NDUFS1	NADH-ubiquinone oxidoreductase 75 kDa subunit, mitochondrial	3.81E-05	2.33
NDUFA4	Cytochrome c oxidase subunit NDUFA4	5.01E-05	4.10
ATP5F1C	ATP synthase subunit gamma, mitochondrial	5.94E-05	3.28
UQCRQ	Cytochrome b-c1 complex subunit 8	6.71E-05	2.82
NDUFB4	NADH dehydrogenase [ubiquinone] 1 beta subcomplex subunit 4	6.96E-05	2.13
LOC100352363	Cytochrome c oxidase subunit 6C	7.03E-05	2.04
NDUFA9	NADH dehydrogenase [ubiquinone] 1 alpha subcomplex subunit 9, mitochondrial	7.38E-05	2.82
NDUFA6	NADH dehydrogenase [ubiquinone] 1 alpha subcomplex subunit 6	7.81E-05	2.15
LOC100346096	ATP synthase subunit f, mitochondrial	8.50E-05	2.63
NDUFS2	NADH dehydrogenase [ubiquinone] iron-sulfur protein 2, mitochondrial	0.00011	2.24
SLC25A11	Mitochondrial 2-oxoglutarate/malate carrier protein	0.00018	3.30
MTCH2	Mitochondrial carrier homolog 2	0.00023	3.36
MGST3	Microsomal glutathione S-transferase 3	0.00024	3.07
NDUFA7	NADH dehydrogenase [ubiquinone] 1 alpha subcomplex subunit 7	0.00025	1.91
IMMT	MICOS complex subunit MIC60	0.00028	5.72
NDUFA13	NADH dehydrogenase [ubiquinone] 1 alpha subcomplex subunit 13	0.00031	2.00
ATP5A1	ATP synthase subunit alpha, mitochondrial	0.00034	2.05
ATP5PB	ATP synthase F(0) complex subunit B1, mitochondrial-like	0.00056	2.90

SLC25A4	ADP/ATP translocase 1	0.00058	5.40
ACSL5	long-chain-fatty-acid--CoA ligase 5	0.00060	2.41
NDUFA12	NADH dehydrogenase [ubiquinone] 1 alpha subcomplex subunit 12	0.00062	2.54
POPDC2	Popeye domain-containing protein 2	0.00064	2.48
CHCHD3	MICOS complex subunit MIC19	0.00064	2.76
NDUFA2	NADH dehydrogenase [ubiquinone] 1 alpha subcomplex subunit 2	0.00073	2.24
COX4	Cytochrome c oxidase subunit 4 isoform 1, mitochondrial precursor	0.00073	1.69
PDE9A	High affinity cGMP-specific 3',5'-cyclic phosphodiesterase 9A	0.00082	3.92
VDAC2	Voltage-dependent anion-selective channel protein 2	0.00090	3.78
CISD1	CDGSH iron-sulfur domain-containing protein 1	0.00113	1.93
NDUFA8	NADH dehydrogenase [ubiquinone] 1 alpha subcomplex subunit 8	0.00113	1.53
NDUFV2	NADH dehydrogenase [ubiquinone] flavoprotein 2, mitochondrial	0.00123	1.80
UBB	Polyubiquitin-B	0.00124	1.60
SLC25A12	Calcium-binding mitochondrial carrier protein Aralar1	0.00132	2.77
MICOS10	MICOS complex subunit MIC10	0.00139	1.78
AIFM1	Apoptosis-inducing factor 1, mitochondrial	0.00141	1.62
PHB	Prohibitin	0.00145	1.65
NDUFA10	NADH dehydrogenase [ubiquinone] 1 alpha subcomplex subunit 10, mitochondrial	0.00152	2.14
COX15	Cytochrome c oxidase assembly protein COX15 homolog	0.00157	2.09
TUFM	Elongation factor Tu, mitochondrial-like | elongation factor Tu, mitochondrial	0.00162	1.88
APOOL	MICOS complex subunit MIC27	0.00164	2.11
NNT	NAD(P) transhydrogenase, mitochondrial	0.00168	2.78
ATP5H	ATP synthase subunit d, mitochondrial	0.00170	1.61
MYH4	Myosin heavy chain 4	0.00176	5.30
LOC100343982	Cytochrome b-c1 complex subunit 6, mitochondrial	0.00205	1.71
STK38L	Serine/threonine-protein kinase 38-like	0.00214	2.22
MPC2	Mitochondrial pyruvate carrier 2	0.00224	2.69

ATP2A2	Sarcoplasmic/endoplasmic reticulum calcium ATPase 2	0.00239	3.00
SAMM50	Sorting and assembly machinery component 50 homolog	0.00245	1.93
PDK4	Pyruvate dehydrogenase kinase, isozyme 4	0.00249	2.01
ACADM	Medium-chain specific acyl-CoA dehydrogenase, mitochondrial	0.00252	1.57
CASQ2	Calsequestrin-2 precursor	0.00260	2.99
PCMT1	Protein-L-isoaspartate(D-aspartate) O-methyltransferase	0.00263	1.47
COX2	Cytochrome c oxidase subunit II (mitochondrion)	0.00271	1.81
SLC25A3	Phosphate carrier protein, mitochondrial	0.00277	3.10
MYH6	Myosin heavy chain 6	0.00288	2.09
TUBA8	Tubulin alpha-8 chain	0.00288	1.58
ATP5F1B	ATP synthase subunit beta, mitochondrial	0.00296	1.48
HSPA9	Stress-70 protein, mitochondrial	0.00306	1.53
MT-ATP8	ATP synthase F0 subunit 8 (mitochondrion)	0.00316	2.14
IDH2	Isocitrate dehydrogenase [NADP], mitochondrial	0.00364	1.50
FAM210A	Protein FAM210A	0.00367	1.94
SRL	Sarcalumenin precursor	0.00371	2.29
CCT7	T-complex protein 1 subunit eta	0.00397	2.30
PRKAR2A	cAMP-dependent protein kinase type II-alpha regulatory subunit	0.00410	1.51
MT-ATP6	ATP synthase F0 subunit 6, partial (mitochondrion)	0.00437	2.01
PLN	Cardiac phospholamban	0.00455	2.61
CPT1B	Carnitine O-palmitoyltransferase 1, muscle isoform, partial	0.00461	2.18
PC	Pyruvate carboxylase, mitochondrial	0.00468	1.77
PDK2	Pyruvate dehydrogenase kinase, isozyme 2	0.00473	1.37
MTX2	Metaxin-2	0.00479	1.75
COX7A1	Cytochrome c oxidase subunit 7A1, mitochondrial, partial	0.00497	2.62
BAG2	BAG family molecular chaperone regulator 2	0.00603	1.72
UQCRFS1	Cytochrome b-c1 complex subunit Rieske, mitochondrial	0.00621	1.80

HSDL2	Hydroxysteroid dehydrogenase-like protein 2 isoform X2	0.00739	2.13
FAM162A	Protein FAM162A	0.00757	1.68
SLC8A2	Sodium/calcium exchanger 2	0.00767	1.99
ATP5ME	ATP synthase subunit e, mitochondrial	0.00772	1.43
ATP1A1	Sodium/potassium-transporting ATPase subunit alpha-1	0.00785	2.00
PYGM	Glycogen phosphorylase, muscle form	0.00808	1.33
TLN1	Talin-1	0.00834	1.64
MOB2	MOB kinase activator 2	0.00838	1.41
HGD	Homogentisate 1,2-dioxygenase	0.00876	3.28
PDP1	Pyruvate dehyrogenase phosphatase catalytic subunit 1	0.00882	1.65
UQCRC2	Cytochrome b-c1 complex subunit 2, mitochondrial	0.00905	1.58
SLC25A5	ADP/ATP translocase 2	0.00910	2.50
ACSL1	Long-chain-fatty-acid--CoA ligase 1	0.00960	1.59
SLC25A20	Mitochondrial carnitine/acylcarnitine carrier protein	0.01001	2.40
PFKM	ATP-dependent 6-phosphofructokinase, muscle type	0.01017	1.55
VAPA	Vesicle-associated membrane protein-associated protein A	0.01020	1.64
MYOM2	Myomesin-2	0.01033	1.54
IDH1	Isocitrate dehydrogenase [NADP] cytoplasmic	0.01052	2.62
EHHADH	Peroxisomal bifunctional enzyme	0.01063	2.43
SDHB	Succinate dehydrogenase [ubiquinone] iron-sulfur subunit, mitochondrial	0.01101	1.60
COX14	Cytochrome c oxidase assembly protein COX14	0.01115	1.66
NIPSNAP2	Protein NipSnap homolog 2	0.01144	1.42
COQ8A	Atypical kinase ADCK3, mitochondrial	0.01175	1.55
BDH1	D-beta-hydroxybutyrate dehydrogenase, mitochondrial	0.01213	2.16
NDUFV3	NADH dehydrogenase [ubiquinone] flavoprotein 3, mitochondrial	0.01319	2.12
EIF4A1	Eukaryotic initiation factor 4A-I	0.01331	2.04
MTFP1	Mitochondrial fission process protein 1	0.01343	1.82
NDRG2	Protein NDRG2	0.01447	1.64
LOC100353846	Alpha-2-macroglobulin	0.01470	2.29
AKT2	RAC-beta serine/threonine-protein kinase	0.01561	1.73

AK3	GTP:AMP phosphotransferase AK3, mitochondrial	0.01570	1.39
ACAA2	3-ketoacyl-CoA thiolase, mitochondrial	0.01588	1.31
ALDH5A1	Methylmalonate-semialdehyde dehydrogenase [acylating], mitochondrial	0.01694	1.38
VDAC1	Voltage-dependent anion-selective channel protein 1	0.01752	1.76
OPA1	Dynamin-like 120 kDa protein, mitochondrial	0.01782	1.55
TRIM72	Tripartite motif-containing protein 72	0.01833	1.28
LOC100353320	Cytochrome c oxidase subunit 7B, mitochondrial	0.01847	1.98
PPA2	Inorganic pyrophosphatase 2, mitochondrial	0.01865	1.54
NDUFAB1	Acyl carrier protein, mitochondrial	0.01893	1.34
HOGA1	4-hydroxy-2-oxoglutarate aldolase, mitochondrial	0.02009	2.14
CLTC	Clathrin heavy chain 1	0.02079	2.11
ATP5MPL	6.8 kDa mitochondrial proteolipid	0.02101	1.48
SUCLA2	Succinyl-CoA ligase [ADP-forming] subunit beta, mitochondrial	0.02123	1.51
PABPC1	Polyadenylate-binding protein 1	0.02196	2.75
PHB2	Prohibitin-2	0.02201	1.53
LNPEP	Leucyl-cystinyl aminopeptidase	0.02213	2.02
BVES	Blood vessel epicardial substance	0.02385	2.12
ALDH4A1	Delta-1-pyrroline-5-carboxylate dehydrogenase, mitochondrial	0.02422	1.43
COX5A	Cytochrome c oxidase subunit 5A, mitochondrial	0.02424	1.47
RPL4	60S ribosomal protein L4	0.02438	1.47
COX6A2	Cytochrome c oxidase subunit 6A2, mitochondrial	0.02521	1.60
PPM1B	Protein phosphatase 1B	0.02570	1.41
TIMM50	Mitochondrial import inner membrane translocase subunit TIM50	0.02775	1.51
FBP1	Fructose-1,6-bisphosphatase 1	0.02809	2.07
NDUFS6	NADH dehydrogenase [ubiquinone] iron-sulfur protein 6, mitochondrial	0.02909	1.49
ACOX1	Peroxisomal acyl-coenzyme A oxidase 1	0.02946	1.85
PCK1	Phosphoenolpyruvate carboxykinase, cytosolic [GTP]	0.03063	2.03
IDH3B	Isocitrate dehydrogenase [NAD] subunit beta, mitochondrial	0.03149	1.42

ATAD1	ATPase family AAA domain-containing protein 1	0.03189	1.41
RHOT1	Mitochondrial Rho GTPase 1	0.03228	1.41
MYBPC3	Myosin-binding protein C, cardiac-type	0.03342	1.78
VDAC3	Voltage-dependent anion-selective channel protein 3	0.03477	1.92
AFG3L2	AFG3-like protein 2	0.03485	1.49
HIST1H2AA	Histone H2A type 1-A	0.03509	2.04
SLC25A10	Mitochondrial dicarboxylate carrier	0.03513	1.43
ATP6V1E1	V-type proton ATPase subunit E 1	0.03539	1.53
COX7A2L	Cytochrome c oxidase subunit 7A-related protein, mitochondrial	0.03565	1.67
BCKDHA	2-oxoisovalerate dehydrogenase subunit alpha, mitochondrial	0.03607	1.36
DTNA	Dystrobrevin alpha	0.03893	1.55
PDK1	Pyruvate dehydrogenase (acetyl-transferring) kinase isozyme 1, mitochondrial	0.04277	1.40
RPN1	Dolichyl-diphosphooligosaccharide--protein glycosyltransferase subunit 1	0.04341	1.36
RRAS2	Ras-related protein R-Ras2	0.04568	1.38
RBM10	RNA-binding protein 10 isoform X4	0.04647	1.34
ALDOB	Fructose-bisphosphate aldolase B	0.04678	1.43
HADHB	Trifunctional enzyme subunit beta, mitochondrial	0.04678	1.34
LPP	Lipoma-preferred partner	0.04694	1.52
SLC25A13	Calcium-binding mitochondrial carrier protein Aralar2	0.04740	1.81
MYOM1	Myomesin-1	0.04768	1.44
RPS4X	40S ribosomal protein S4, X isoform	0.04774	2.19
TGM2	Protein-glutamine gamma-glutamyltransferase 2	0.04831	1.26

Table 3.2: DAVID pathways analysis of proteins significantly enriched in adPDE9-FLAG samples.

Proteins significantly enriched in adPDE9-FLAG samples as compared to adFLAG samples (see Table 1) underwent pathways analysis using the DAVID database. All pathways with $p<0.05$ are shown.

KEGG Pathway	P Value	Genes	Fold Enrichment
Oxidative phosphorylation	1.18E-26	NDUFB4, NDUFAB1, LOC100352363, LOC100353320, UQCRQ, NDUFS6, LOC100343982, NDUFS3, ATP5H, NDUFS2, NDUFS1, NDUFA4, NDUFA5, NDUFA2, NDUFA8, NDUFA9, NDUFA6, NDUFA7, NDUFA13, NDUFA10, LOC100346096, NDUFA12, PPA2, SDHB, COX2, ATP6V1E1, NDUFV2, ATP5A1	17.07
Metabolic pathways	1.29E-18	ACOX1, EHHADH, NDUFAB1, LOC100352363, UQCRQ, LOC100353320, NDUFS6, RPN1, SUCLA2, NDUFS3, NDUFS2, ATP5H, NDUFS1, ACAA2, ACADM, ALDH5A1, FBP1, NDUFA13, PFKM, NDUFA10, NDUFA12, LOC100346096, NNT, NDUFB4, ALDOB, HADHB, LOC100343982, ACSL1, IDH2, ALDH4A1, IDH1, BDH1, ACSL5, NDUFA4, BCKDHA, NDUFA5, NDUFA2, NDUFA8, NDUFA9, NDUFA6, HOGA1, NDUFA7, HGD, IDH3B, PCK1, SDHB, PYGM, COX2, ATP6V1E1, NDUFV2, ATP5A1, PC	3.45
Biosynthesis of antibiotics	3.28E-07	BCKDHA, ACAA2, ACADM, EHHADH, ALDOB, FBP1, AK3, IDH3B, PFKM, PCK1, HADHB, SDHB, IDH2, IDH1, SUCLA2	5.54
Carbon metabolism	8.07E-07	ACOX1, ACAA2, CPT1B, ACADM, ACSL1, EHHADH, HADHB, ACSL5	14.85
Fatty acid degradation	1.21E-06	SDHB, ACADM, EHHADH, ALDOB, IDH2, FBP1, IDH3B, IDH1, PFKM, SUCLA2, PC	7.70
Fatty acid metabolism	3.18E-06	ACOX1, ACAA2, CPT1B, ACADM, ACSL1, EHHADH, HADHB, ACSL5	12.20

Citrate cycle (TCA cycle)	4.84E-06	SDHB, IDH2, IDH3B, IDH1, SUCLA2, PC, PCK1	15.32
Cardiac muscle contraction	1.71E-04	ACOX1, CPT1B, ACADM, ACSL1, EHHADH, PCK1, ACSL5	8.30
PPAR signaling pathway	3.05E-04	LOC100343982, COX2, ATP1A1, MYH6, LOC100352363, LOC100353320, UQCRQ	7.47
cGMP-PKG signaling pathway	6.08E-04	ATP2A2, SLC25A4, SLC25A5, PLN, ATP1A1, VDAC2, VDAC3, VDAC1, AKT2	4.66
Biosynthesis of amino acids	0.0015	ALDOB, IDH2, IDH3B, IDH1, PFKM, PC	7.02
Peroxisome	0.0041	ACOX1, ACSL1, EHHADH, IDH2, IDH1, ACSL5	5.57
Valine, leucine and isoleucine degradation	0.0044	BCKDHA, ACAA2, ACADM, EHHADH, HADHB	7.36
Adipocytokine signaling pathway	0.0074	CPT1B, ACSL1, AKT2, PCK1, ACSL5	6.37
2-Oxocarboxylic acid metabolism	0.0161	IDH2, IDH3B, IDH1	15.07
Calcium signaling pathway	0.0177	ATP2A2, SLC25A4, SLC25A5, PLN, VDAC2, VDAC3, VDAC1	3.32
Glycolysis / Gluconeogenesis	0.0454	ALDOB, FBP1, PFKM, PCK1	4.95
Propanoate metabolism	0.0467	ALDH5A1, EHHADH, BDH1	8.54
Butanoate metabolism	0.0467	ACADM, EHHADH, SUCLA2	8.54
Pentose phosphate pathway	0.0467	ALDOB, FBP1, PFKM	8.54

Table 3.3: Proteins significantly less associated with PDE9 following ET-1 treatment. adPDE9-FLAG samples were compared to adPDE9-FLAG+ET-1 samples using LIMMA. All proteins with p<0.05 and a ratio for PDE9+ET-1 to PDE9 less than 1 are shown.

Gene Name	Protein Name	P Value	Ratio PDE9+ET1/PDE9
NDUFB4	NADH dehydrogenase [ubiquinone] 1 beta subcomplex subunit 4	0.0011	0.60
NDUFA7	NADH dehydrogenase [ubiquinone] 1 alpha subcomplex subunit 7	0.0018	0.63
COX6C	Cytochrome c oxidase subunit 6C	0.0024	0.51
NDUFS2	NADH dehydrogenase [ubiquinone] iron-sulfur protein 2, mitochondrial	0.0028	0.62
NDUFS3	NADH dehydrogenase [ubiquinone] iron-sulfur protein 3, mitochondrial	0.0043	0.57
NDUFA13	NADH dehydrogenase [ubiquinone] 1 alpha subcomplex subunit 13	0.0056	0.62
COX14	Cytochrome c oxidase assembly protein COX14	0.0062	0.57
ATP5MF	ATP synthase subunit f, mitochondrial	0.0073	0.58
MGST3	Microsomal glutathione S-transferase 3	0.0089	0.49
NDUFS4	NADH dehydrogenase [ubiquinone] iron-sulfur protein 4, mitochondrial	0.0090	0.61
NDUFA8	NADH dehydrogenase [ubiquinone] 1 alpha subcomplex subunit 8	0.0095	0.55
NDUFA6	NADH dehydrogenase [ubiquinone] 1 alpha subcomplex subunit 6	0.0137	0.64
MTCH2	Mitochondrial carrier homolog 2	0.0160	0.40
SLC25A11	Mitochondrial 2-oxoglutarate/malate carrier protein	0.0160	0.52
NDUFA9	NADH dehydrogenase [ubiquinone] 1 alpha subcomplex subunit 9, mitochondrial	0.0169	0.52
IDH2	Isocitrate dehydrogenase [NADP], mitochondrial	0.0202	0.74
CBR4	Carbonyl reductase family member 4	0.0206	0.65
NDUFA12	NADH dehydrogenase [ubiquinone] 1 alpha subcomplex subunit 12	0.0214	0.57
UQCR10	Cytochrome b-c1 complex subunit 9	0.0222	0.35
ACSL5	Long-chain-fatty-acid--CoA ligase 5	0.0239	0.56
ATP5PB	ATP synthase F(0) complex subunit B1, mitochondrial-like	0.0240	0.47

MPC2	Mitochondrial pyruvate carrier 2	0.0243	0.48
NDRG2	Protein NDRG2	0.0254	0.68
COX7A2	Cytochrome c oxidase subunit 7A2, mitochondrial	0.0261	0.63
MT-ATP8	ATP synthase F0 subunit 8 (mitochondrion)	0.0287	0.62
TUFM	Elongation factor Tu, mitochondrial	0.0292	0.70
NDUFA5	NADH dehydrogenase [ubiquinone] 1 alpha subcomplex subunit 5	0.0299	0.62
PDK4	Pyruvate dehydrogenase kinase, isozyme 4	0.0300	0.70
GTF3C4	General transcription factor 3C polypeptide 4	0.0300	0.59
COX2	Cytochrome c oxidase subunit II (mitochondrion)	0.0314	0.71
UBB	Polyubiquitin-B	0.0324	0.68
PHB	Prohibitin	0.0332	0.74
COX5A	Cytochrome c oxidase subunit 5A, mitochondrial	0.0339	0.66
UQCRFS1	Cytochrome b-c1 complex subunit Rieske, mitochondrial	0.0353	0.73
SAMM50	Sorting and assembly machinery component 50 homolog	0.0365	0.69
MICOS10	MICOS complex subunit MIC10	0.0376	0.64
ATP5F1C	ATP synthase subunit gamma, mitochondrial	0.0376	0.50
COX7A1	Cytochrome c oxidase subunit 7A1, mitochondrial	0.0390	0.47
COX7B	Cytochrome c oxidase subunit 7B, mitochondrial	0.0394	0.39
RAN	GTP-binding nuclear protein Ran	0.0410	0.71
FAM162A	Protein FAM162A	0.0433	0.71
COX6A2	Cytochrome c oxidase subunit 6A2, mitochondrial	0.0435	0.34
APOOL	MICOS complex subunit MIC27	0.0461	0.64
UQCRQ	Cytochrome b-c1 complex subunit 8	0.0468	0.54
COX4	Cytochrome c oxidase subunit 4 isoform 1, mitochondrial precursor	0.0482	0.72
ATAD1	ATPase family AAA domain-containing protein 1	0.0487	0.73

Table 3.4: Proteins significantly more associated with PDE9 following ET-1 treatment.

adPDE9-FLAG samples were compared to adPDE9-FLAG+ET-1 samples using LIMMA. All proteins with p<0.05 and a ratio for PDE9+ET-1 to PDE9 greater than 1 are shown.

Gene Name	Protein Name	P Value	Ratio PDE9+ET1/PDE9
KRT5	Keratin, type II cytoskeletal 5 isoform X2	0.0005	2.93
NCCRP1	F-box only protein 50	0.0013	3.75
KRT16	Keratin, type I cytoskeletal 16	0.0020	2.31
AKR7A3	Aflatoxin B1 aldehyde reductase member 3	0.0042	1.97
KLHL41	Kelch-like protein 41	0.0045	1.65
CLU	Clusterin precursor	0.0057	1.98
NID1	Nidogen-1	0.0083	1.37
S100A14	Protein S100-A14	0.0087	2.01
CAPZA1	F-actin-capping protein subunit alpha-1	0.0102	2.35
ANXA1	Annexin A1	0.0103	1.67
HSPB7	Heat shock protein beta-7	0.0109	1.34
ACOT13	Acyl-coenzyme A thioesterase 13	0.0116	1.78
KRT71	Keratin, type II cytoskeletal 71	0.0118	2.17
AASS	Alpha-aminoadipic semialdehyde synthase, mitochondrial	0.0123	1.33
IDE	Insulin-degrading enzyme	0.0127	1.78
CHRDL2	Chordin-like protein 2	0.0128	8.83
XIRP1	Xin actin-binding repeat-containing protein 1	0.0134	1.62
KRT5	Keratin, type II cytoskeletal 5 isoform X1	0.0139	1.61
KRT14	Keratin, type I cytoskeletal 14	0.0143	1.81
ANKRD33	Ankyrin repeat domain-containing protein 33	0.0174	1.78
KRT80	Keratin, type II cytoskeletal 80	0.0183	1.53
MAP4	Microtubule-associated protein 4	0.0184	1.54
KRT17	Keratin, type I cytoskeletal 17	0.0193	2.28
AAMDC	Mth938 domain-containing protein	0.0196	1.40
CHMP5	Charged multivesicular body protein 5	0.0197	1.74

OBSCN	Obscurin	0.0227	1.52
PPP2CA	Serine/threonine-protein phosphatase 2A catalytic subunit alpha isoform	0.0231	1.77
KRT1	Keratin, type II cytoskeletal 1	0.0239	1.52
KRT13	Keratin, type I cytoskeletal 13	0.0239	1.81
KARS	Lysine--tRNA ligase	0.0241	1.32
PACSIN3	Protein kinase C and casein kinase substrate in neurons protein 3	0.0276	1.49
GSN	Gelsolin	0.0279	2.30
NRAP	Nebulin-related-anchoring protein	0.0294	1.65
PRSS2	Trypsin-2	0.0335	1.89
EZR	Ezrin	0.0344	1.24
EIF3H	Eukaryotic translation initiation factor 3 subunit H	0.0355	1.45
PGER1	Prostaglandin-E(2) 9-reductase-like	0.0360	1.31
YWHAE	14-3-3 protein epsilon	0.0373	1.45
FABP5	Fatty acid-binding protein, epidermal	0.0376	1.44
ENO2	Gamma-enolase	0.0386	2.13
GIMD1	GTPase IMAP family member GIMD1	0.0397	1.74
SERPINB12	Serpin B12	0.0413	1.82
AMY2A	Pancreatic alpha-amylase	0.0437	1.70
MAP1B	Microtubule-associated protein 1B	0.0441	1.23
ARG1	Arginase-1	0.0444	1.46
EIF4H	Eukaryotic translation initiation factor 4H	0.0460	1.22
LTBP1	Latent-transforming growth factor beta-binding protein 1	0.0462	1.60
SPRR1A	Cornifin alpha-like	0.0468	1.79
SERPINA12	Serpin A12	0.0486	1.62
SYNCRIP	Heterogeneous nuclear ribonucleoprotein Q	0.0486	1.47
SNRPA	U1 small nuclear ribonucleoprotein A	0.0490	1.38

CHAPTER 4: Generation and testing of novel molecular tools to study PDE5 and PDE9 compartmentation

INTRODUCTION

To date, few studies have been performed examining the precise cellular compartments within which PDE5 and PDE9 reside in cardiac myocytes. This is likely due in part to a lack of prior molecular tools with which to identify these small, complex domains within the cell. A previous study within the Kass lab (Manling Zhang, unpublished) examined the proteome associated with pulldown of PDE5 from adult mouse cardiac myocytes, but no comparable study has been performed for PDE9 due to the lack of a mouse expressing tagged PDE9 protein (although in Chapter 2 of this thesis we now present pulldown data for FLAG-tagged PDE9 overexpressed in adult rabbit cardiomyocytes). While pulldown identifies direct binding partners (or binding complexes) of the protein of interest, the broader environment within which the protein of interest resides is not fully identified by this approach. Furthermore, there can even be difficulties identifying binding partners depending on the conditions used for cell lysis. If a strong detergent is used, protein interactions are interrupted, and binding partners cannot be identified. Good identification of binding partners and complexes is also dependent on efficient pulldown of the protein of interest. If not done well, this may lead to identification of fewer binding partners due to low protein abundance that cannot be detected by a mass spectrometer. Therefore, to fully identify PDE compartments, a novel molecular approach was needed to concisely examine its cellular nanodomain.

In 2012, the lab of Alice Ting first premiered the APEX tag by showing its utility as a genetically-encodable tag that allows for electron microscopic imaging of a protein of interest without the need for an antibody[165]. They then expanded upon this the following year, where they described an elegant use of APEX for spatially restricted proteomic mapping[57]. Since this time, the lab has further optimized these methods and introduced APEX2, an improved version of APEX with higher catalytic activity, allowing for studies in cellular microdomains that are particularly sensitive to protein overexpression, such as the endoplasmic reticulum and mitochondrial outer membrane[166].

APEX2 is an ascorbate peroxidase derived from the soybean that carries several mutations allowing the protein to be monomeric as well as giving it higher catalytic activity. It converts various phenol derivatives into phenoxyl radicals, which can then tag nearby electron-rich amino acids, namely cysteine, histidine, tryptophan, and tyrosine. This particular function of APEX2 allows for proteomic mapping, as when cells overexpressing an APEX2 fusion protein are provided with biotin-phenol and H_2O_2, proteins within a 20 nm radius of the fusion protein are tagged by biotin-phenoxyl radicals, facilitating streptavidin pulldown of tagged proteins and subsequent identification by mass spectrometry. Notably, this tagging reaction occurs very quickly, with labeling taking only one minute, allowing for monitoring of highly dynamic cellular processes. APEX2 also catalyzes H_2O_2-dependent polymerization of diaminobenzidine (DAB), which can subsequently react with the staining reagent osmium to generate contrast that can be visualized by electron microscopy to provide high-resolution images of protein sub-cellular localization.

Several other similar tags exist, including BioID[54], BioID2[55], TurboID, and miniTurbo[56]. These four tags are all variants of biotin ligase, which directly transfers the biotin moiety to proteins (unlike the biotin-phenoxyl radical produced by APEX2). BioID and BioID2 were developed by the Roux lab at the University of South Dakota, with the creation of BioID2 evolving from a desire for a smaller and more efficient ligase. These enzymes require only biotin to perform labeling experiments, but need approximately 24 hours to complete labeling. This time frame limits their application to static cellular systems, as dynamic cell responses to stimuli will be lost. TurboID and miniTurbo were developed by the Ting lab as improvements upon the BioID enzymes, namely improving the labeling time by decreasing it to only 10 minutes as compared to the 24 hours needed for BioID. These enzymes are also biotin ligases, like BioID and BioID2, but underwent directed evolution to be highly efficient. These new tags from the Ting lab appear promising for future studies of dynamic cellular systems, as they have relatively fast labeling time and only require biotin.

METHODS

Generation of GFP-APEX2-tagged PDE Constructs and Adenoviruses: PDE5, PDE9, and GFP-APEX2 were subcloned into pcDNA3.1+ (Thermo Fisher Scientific) utilizing New England BioLabs HiFi cloning. Briefly, pcDNA3.1+ was digested with NheI and XhoI (New England BioLabs) and gel purified. The PDE5, PDE9, and GFP-APEX2 inserts were amplified with primers designed using the NEBuilder design tool (New England BioLabs) and synthesized by Integrated DNA Technologies. GFP-APEX2 was amplified from pcDNA3 Connexin43-GFP-APEX2, which was a gift from Alice Ting (Addgene plasmid #49385; http://n2t.net/addgene:49385; RRID:Addgene_49385). A short linker was included between the PDE and GFP-APEX2 fragments consisting of the peptide sequence GGSGGT. Q5 high fidelity polymerase (New England BioLabs) was used for PCR amplification. PCR fragments were gel purified, and assembly and bacterial transformation was then performed according to NEB HiFi protocol. Sequencing primers were designed using the GenScript sequencing primer design tool (https://www.genscript.com/tools/dna-sequencing-primer-design). All cloning and sequencing primer sequences can be found in **Table 4.1 and** 4.2, respectively. Adenoviruses for GFP-APEX2, PDE5-GFP-APEX2, and PDE9-GFP-APEX2 were generated by Welgen, Inc (Worcester, MA).

Neonatal rat myocyte isolation and transfection: Neonatal rat myocytes were isolated as previously described[65]. NRCMs were cultured for 24 hours in high glucose (4.5 g/L) DMEM with 10% FBS, L-glutamine (4 mM), and penicillin/streptomycin (100 U/mL) prior to study. For plasmid transfection, NRCMs were transfected overnight using Lipofectamine 3000 (Thermo Fisher Scientific) according to manufacturer protocol. For adenovirus infection, NRCMs were infected with adenovirus (10 MOI) in plain DMEM for 3-4 hours. Media was then changed back to high glucose DMEM containing 10% FBS, penicillin-streptomycin, and glutamine after both transfection and infection. Cells were given at least 48 hours to express the fusion constructs prior to sample collection or fixation.

Adult rabbit myocyte isolation and infection: Adult rabbit myocytes were isolated as previously described[149]. Myocytes were infected with adenovirus (10 MOI) at the time of plating in Medium 199 (Sigma). After 3-4 hours, media was changed to Medium 199 containing 2% FBS, penicillin-streptomycin (100 U/mL), L-glutamine (0.1 mg/mL), creatine (5 mM), taurine (5 mM), and L-carnitine (2 mM). After overnight incubation, cells were stimulated with endothelin-1 (100 nM, Sigma) or vehicle for 24 hours in Medium 199 containing penicillin-streptomycin, L-glutamine (0.1 mg/mL), creatine (5 mM), taurine (5 mM), and L-carnitine (2 mM).

Biotinylation protocol: Biotinylation was performed according to the published protocol from Hung et al[167], with several deviations. Modifications to the published protocol were addition of N-acetyl-cysteine (to increase biotinylation) and cycloheximide (to reduce non-compartment specific biotinylation). N-acetyl-cysteine (500 µM, Sigma) and cycloheximide (100 µM, Sigma) were added 2 hours prior to addition of H_2O_2. All other parts of the protocol were performed as recommended.

Assessment of cGMP levels in neonatal myocytes: For cGMP assay samples, neonatal rat myocytes were first transfected with plasmid or infected with virus. Cells were then treated the following day with an sGC activator, BAY 60-2770 (10 nM, Bayer Healthcare Pharmaceuticals), atrial natriuretic peptide (1 µM, Sigma A1663), and/or endothelin-1 (100 nM, Sigma E7764) for 48 hours prior to the assay. Cyclic GMP levels were measured using the cGMP Direct BioTrak EIA kit (GE Healthcare) according to manufacturer protocol. Plates were read at both 450 and 630 nm using a Molecular Devices SpectraMax M5 microplate reader. For back-calculation of cGMP levels for the 450 nm read, a semi-log fit was used. For back-calculation of cGMP levels for the 630 nm read, a 4-parameter fit was used. Normalization was performed as recommended by the manufacturer. Statistical analysis was performed using GraphPad Prism version 7, with comparisons done using a one-way ANOVA or Kruskal-Wallis test with post-hoc Dunnett's tests. A non-parametric Kruskal-Wallis test was used if the Brown-Forsythe test returned a value less than 0.05.

Immunofluorescence: Cells were transfected or transduced as described. After 48 hours of fusion construct expression, cells were fixed in 10% formalin in PBS, permeabilized with 0.5% saponin in PBS, and blocked with 3% BSA in PBS. Cells were then stained overnight in 3% BSA with 0.5% saponin in PBS at 4°C for biotinylated proteins with Alexa 555-coupled streptavidin (#S32355, Thermo Fisher Scientific, 1:1000), PDE5 (antibody #2395, Cell Signaling Technology, 1:200), or PDE9 (custom antibody, ProSci Inc, 1:200). Cells were then counterstained with anti-rabbit Alexa 568-coupled secondary antibody (ThermoFisher) at a 1:500 dilution for PDE5 and PDE9 if necessary. Hard-mount Vectashield with DAPI (Vector Labs) was used to preserve fluorescence after staining was complete. Imaging was performed on a Leica TCS SPE confocal microscope using a 40X oil-immersion objective. GFP was imaged as a marker for the fusion protein.

Immunoprecipitation of biotinylated proteins: Adult rabbit cardiomyocytes were infected and biotinylated as described. After samples were collected, they were sonicated to disrupt cell membranes and spun down. Protein concentration was measured using the Pierce 660-nm protein assay (ThermoFisher). For immunoprecipitation, 100 µL of MyOne Streptavidin C1 DynaBeads (ThermoFisher) were pre-washed twice with RIPA buffer (Sigma), and then incubated with 275 µg of protein. Beads were rotated with lysate for two hours at room temperature. Following incubation, beads were washed twice with RIPA buffer, once with 1M KCl, once with 0.1M Na_2CO_3, once with 2M urea in 10 mM Tris-HCl, and twice again with RIPA buffer. Elution was performed by boiling the beads four times in 2X Novex Tris-Glycine SDS sample buffer containing 2 mM biotin (Sigma) and 20 mM DTT (Sigma).

Western blotting: Samples were run under reducing and denaturing conditions on precast 4-20% Mini-PROTEAN Tris-Glycine TGX gels (Bio-Rad). For immunoprecipitation samples, both input and eluate samples were run. Following semi-dry transfer to nitrocellulose membranes, blotting was performed for biotinylated proteins using a LI-COR streptavidin coupled antibody (LI-COR 926-32230). Total protein staining for normalization was performed using the LI-COR REVERT staining kit. Membranes were imaged on a LI-COR Odyssey using Image Studio v5.0 software.

Mass spectrometry experimental design: Adult rabbit cardiomyocytes were isolated and cells were infected with one of three viruses: adGFP-APEX2, adPDE5-GFP-APEX2, or adPDE9-GFP-APEX2. All samples were treated with biotin-phenol (Sigma). Within each virus group, samples were either with ET-1 (100 nM, Sigma) or vehicle and with H_2O_2 (1 mM, Sigma) or vehicle for a total of four samples per virus group. The experiment was repeated with n=3 rabbits for a total of three independent experiments. Tandem mass tag labels were shuffled between samples in different multiplexes to minimize peptide labeling bias (see below).

Mass spectrometry peptide preparation: Following sample elution from streptavidin magnetic beads, methanol-chloroform extraction was performed for all samples according to the methods of Wessel and Flugge[150]. After extraction was complete, samples were resuspended in 9M urea containing 10 mM Tris-HCl, and subsequently diluted 1:6 in 60 mM HEPES pH 7.5, and 0.6 mM DTT, to yield a final digestion buffer containing 50 mM HEPES, pH 7.5 1.5M urea, and 0.5 mM DTT. 1 μg of trypsin/Lys-C (Promega V5073) was added to each sample, and peptide digest proceeded overnight at 25°C (to reduce lysine carbamylation) with samples shaking at 1050 RPM. The next day, another 0.5 µg of trypsin was added along with 5 mM DTT, and digest continued for another 2 hours. 20 mM iodoacetamide was then added to alkylate the samples for 1 hour in the dark. 0.5% v/v TFA was added to acidify the peptides, which were then purified on C18 spin columns (Pierce) according to manufacturer's instructions and eluted using 0.1% formic acid in 60% acetonitrile. Finally, samples were evaporated to dryness in an Eppendorf Vacufuge. Distilled deionized H_2O was added after the first spin and samples were subjected to a second round of evaporation to remove trace levels of formic acid and acetonitrile.

Peptide labeling and 2-dimensional liquid chromatography coupled to tandem mass spectrometry (2D-LC-MS/MS): Samples were then resuspended in triethylammonium bicarbonate pH 8.5. Peptides were labeled with TMT (tandem mass tag) reagents (ThermoFisher), with labels shuffled between samples on different multiplexes to minimize labeling bias. TMT labeling was done with samples brought up in 100 µl TEAB and labels brought up in 41 µL anhydrous acetonitrile. Each label was added to its corresponding sample for 1 hour before being quenched with 8 µL of 5% hydroxyl amine for 15 minutes. Samples were then mixed and dried down and subsequently brought up in 2 mL of 10 mM TEAB and injected onto an Agilent LC running a 2.1 x 100 mm Waters BEH C18 column with 1.7 µM particles at 250 µL/minute. The first 12 fractions were flow-through, with the next 84 samples collected on an 85-minute gradient from 0-90% acetonitrile containing 10 mM TEAB. These 84 fractions were concatenated into 12 fractions for LC-MS/MS analysis.

LC-MS/MS was performed on an Orbitrap Fusion Lumos Tribrid Mass Spectrometer (ThermoFisher). Liquid chromatography was performed prior to MS/MS by bringing samples up in buffer A (2% acetonitrile, 0.1% formic acid 98% deionized water), and then injecting the sample onto a trapping column in buffer A for 5 minutes at 5 µL/min before switching to the analytical column (Reprosil C18 3 µM particles with 100 angstrom pore size, packed approximately 20 cm with 75 µM internal diameter fused silica PicoFrits from New Objective (Woburn, MA)) at 300 nL/min. The solution was then switched to 10% buffer B (90% acetonitrile/10% deionized water and 0.1% formic acid). The gradient then went from 10% to 20% buffer B over 45 minutes and then to 35% at 77 minutes before jumping to 100% buffer B at 80 minutes, holding for 2 minutes, then returning to 2% buffer B in another 2 minutes before the liquid chromatography run ended at 90 minutes. The fractions were injected consecutively following this gradient scheme.

MS was conducted with the following instrument settings. MS1 resolution was set to 120,000 with a target ion count of 400,000. The precursor ion isolation width was 0.7 Daltons. For MS2, resolution was set to 50,000 with a target ion count of 100,000. Collision energy was set to 38. Easy IC internal calibration was used on the precursors which uses the ETD ion for mass correction on-the-fly for MS.

Protein identification: Peak list files (.RAW) were searched against a rabbit database of predicted protein sequences (NCBI RefSeq, taxonomy: Oryctolagus cuniculus, 2018, FASTA format, 38559 sequences; RefSeq83_Oryctolagus_cuniculus_180413_1.fasta;), using Mascot Version: 2.2.0 (Matrix Science) interfaced through Proteome Discoverer 1.4 (Thermo). Peaks were filtered at a signal to noise ratio of 1.5, deisotoped, and searched with a parent ion mass tolerance of 10 ppm and an MS2 mass tolerance of 0.02 Da. Trypsin was specified as the enzyme and 1 missed cleavage was allowed. Cysteine carbamidomethylation and N-terminal amine labeling with TMT 10-plex reagent were specified as fixed modifications for the database search. Dynamic modifications included N-pyroglutamine, oxidized methionine, phosphorylation of serine, threonine, and tyrosine, and TMT labeling of lysine. All searches were conducted with the reversed database search mode engaged. Percolator software was used for peptide FDR (q-value) calculations. Mascot output files (.dat) tabulated were in Proteome Discoverer. Of the high confidence peptides (q< 0.01), 2% of unique spectra had intensities missing from one or more channels, indicative of efficient TMT labeling and fragmentation. Spectra for which peptide co-isolation interference was >51% were omitted from analysis. Proteins identified by single spectra were likewise omitted.

Protein quantification by TMT and statistical analysis: TMT reporter ion intensities were integrated over 30 ppm using the most confident centroid method and corrected for purity in Proteome Discoverer 1.4 (Thermo). Missing labeled channel intensities (<2% of spectra) were inversely proportional to the untransformed median ion intensities across the channels. For individual spectra for which missing data was <50%, the missing value was replaced by the median value of the lowest intensities in each channel. Following missing value imputation, these signals were quantified using the median sweep algorithm originally described by Herbrich et al[151] essentially as implemented recently by Foster et al[152] with a minor modification. TMT reporter ion intensities were 1) logarithmically-transformed (base 2), 2) quantile-normalized for each channel, 3) median-centered for each individual spectrum across channels, 4) protein abundance determined by taking the median value of the logarithmically-transformed median-centered intensities for all spectra belonging to that protein in a given channel, and finally, 5) re-centered for each channel by subtracting the median protein abundance. Following the median sweep, differential protein abundance between experimental groups was assessed by means of an empirical Bayesian method, specifically, linear modeling of microarrays (LIMMA)[153, 154] with multi-group comparison, as implemented in Omics Explorer (Qlucore, Lund, Sweden). Resulting p-values were corrected for multiple comparisons using the false discovery rate (q-value) method of Benjamini-Hochberg[155].

Table 4.1: Primers used for assembly of PDE5 and PDE9 GFP-APEX2 fusion constructs.

All sequences are listed in the 5' → 3' orientation.

Primer Sequence	Amplicon	Plasmid
Forward: tatagggagacccaagctggctagcATGGAACGAGCGGGCCCC **Reverse:** cgccgctgccgccGTCCCGCTTGCCCTGGCT	PDE5	PDE5-GFP-APEX2
Forward: caagcgggacggcggcagcggcggcaccATGGTGAGCAAGGGCGAG **Reverse:** tttaaacgggccctctagactcgagTTAGGCATCAGCAAACCCAAG	GFP-APEX2	PDE5-GFP-APEX2
Forward: tatagggagacccaagctggctagcATGGGATCCGGCTCCTCC **Reverse:** cgccgctgccgccGGCACAGTCTCCTTCACTG	PDE9	PDE9-GFP-APEX2
Forward: agactgtgccggcggcagcggcggcaccATGGTGAGCAAGGGCGAG **Reverse:** tttaaacgggccctctagactcgagTTAGGCATCAGCAAACCCAAG	GFP-APEX2	PDE9-GFP-APEX2

Table 4.2: Gene-specific primers used for sequencing of PDE5 and PDE9 GFP-APEX2 fusion constructs.

All sequences are listed in the 5’ → 3’ orientation.

Primer Sequence	Gene
TCTTTTACTAGCTCCAAGAGCC	Mouse PDE5
TCCCACCATTTCCTGATTTC	Mouse PDE5
TGGGATATTAAGTGGCTCCATC	Mouse PDE5
CGGTAATTTTAAGGGTTTGGG	Mouse PDE5
CAAGCACTGGTCAAAATGATG	Mouse PDE5
AAAAGAACTTAACATGGAGCCG	Mouse PDE5
TGGCATCTATGAACCCAACTT	Mouse PDE5
TCCTGGTAGCAGCCCTGG	Human PDE9
CTCAGCATCTCATTGGGCTC	Human PDE9
ATCAGGTGGGATGTTGGAGA	Human PDE9
TGCAGCATGATCTCCTCAAC	Human PDE9
TATATCATGGCCGACAAGCA	GFP
CTGGTAGTGGTCGGCGAG	GFP
CGCTAACAACGGTCTTGACA	APEX2
AGAAATCGGCGTAGCTCAAA	APEX2

RESULTS

Generation of the PDE-GFP-APEX2 fusion constructs

Due to the dual functions of APEX2, we decided to employ this novel tag in order to explore the cardiac nanodomains of PDE5 and PDE9. Fusion constructs were generated in the pcDNA3.1+ backbone in which GFP and APEX2 were fused to the C-terminus of either PDE5 or PDE9. A short linker was included between the PDE and the tags to allow for separation and flexibility between the different moieties of the fusion protein (**Figure 4.1A**). Following completion of the pcDNA3.1+ constructs, adenoviruses were made for further use in cardiomyocyte studies, as expression levels are much higher with adenoviral transduction than plasmid transfection for both neonatal and adult cardiomyocytes. The viruses were shown to express well in neonatal cardiomyocytes, with GFP signal clearly visible upon live-cell epifluorescent imaging (**Figure 4.1B**). Cell lysates were also probed by Western blotting, which showed all viruses to be expressing proteins of the expected molecular weights (**Figure 4.1C**).

Figure 4.1: PDE-GFP-APEX2 fusion constructs express in neonatal cardiac myocytes.

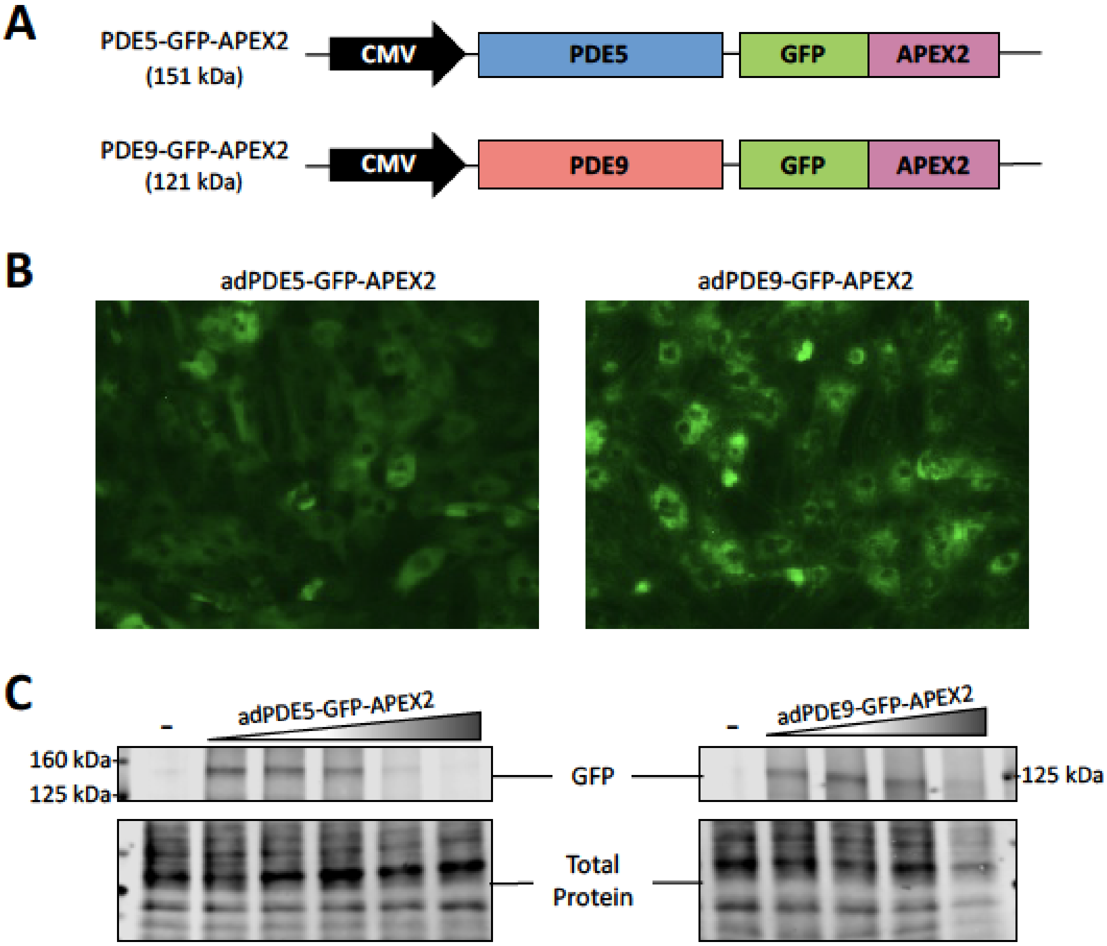

Figure 4.1: PDE-GFP-APEX2 fusion constructs express well in neonatal cardiac myocytes.

A) Design of the fusion constructs, with expected molecular weights. B) Live cell GFP imaging of neonatal myocytes transduced with adPDE5 or adPDE-GFP-APEX2. C) SDS-PAGE blotting for GFP in neonatal myocytes expressing either adPDE5 or adPDE9-GFP-APEX2. Cells were transduced with increasing amounts of virus, and after 48 hours samples were collected and subjected to SDS-PAGE and subsequent blotting for GFP to identify fusion proteins. Both adPDE5-GFP-APEX2 (left) and adPDE9-GFP-APEX2 (right) appear at the correct molecular weight. Notably, as the amount of virus increases so does cell death, causing the decrease in fusion protein expression seen at higher amounts of virus.

Fusion of the GFP-APEX2 moiety does not inhibit PDE-catalyzed cGMP hydrolysis

The primary function of phosphodiesterases is to catalyze hydrolysis of cyclic nucleotides into their non-cyclic forms. PDE5 and PDE9 preferentially hydrolyze cyclic GMP, generated either by soluble or receptor-coupled guanylyl cyclases that are stimulated by nitric oxide and natriuretic peptide, respectively. As the GFP and APEX2 moieties were fused to the C-terminal end next to the catalytic domain of each PDE, it was critical to ensure that cyclic nucleotide hydrolysis was unimpeded by the addition of these relatively bulky tags. In order to determine whether the PDE fusion constructs were functional, neonatal rat myocytes were transfected or transduced with either a control GFP-APEX2 construct, or PDE5 or PDE9-GFP-APEX2. Cells were subsequently stimulated for 48 hours with a soluble guanylyl cyclase activator, BAY 60-2770, and atrial natriuretic peptide (ANP) to maximize cGMP levels in the cell. After this, cGMP assays were performed to assess whether PDE overexpression reduced cGMP levels. cGMP levels were significantly reduced by overexpression of PDE9, and border-line significantly reduced by PDE5 overexpression, but were unaffected by the control GFP-APEX2, indicating that the catalytic domain of both PDE5 and PDE9 is unaffected by the addition of the GFP and APEX2 tags (**Figure 4.2**).

Figure 4.2: GFP-APEX2-tagging of PDE5 and PDE9 near the catalytic domain does not inhibit cGMP hydrolysis

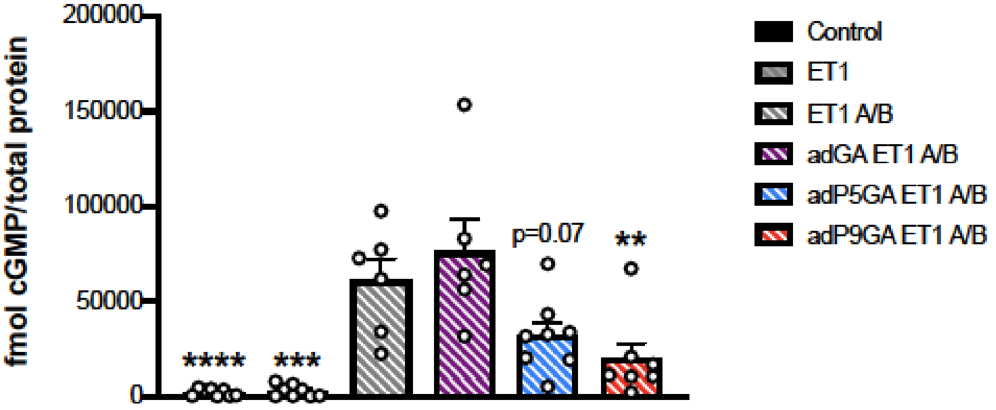

Figure 4.2: PDE5 and PDE9 tagged with GFP-APEX2 retain catalytic activity Neonatal rat myocytes were transfected or transduced with a GFP-APEX2, PDE5-GFP-APEX2, or PDE9-GFP-APEX2. Cells were then stimulated with ET-1 (100 nM), atrial natriuretic peptide (ANP, 1 µM), and an sGC activator (BAY 60-2770, 10 nM). ANP and BAY treatment was used to stimulate cGMP production by both the NP and NO pathways, and is denoted in the figure legend by "A/B." cGMP levels were assayed by ELISA, and normalized to total protein. Data shown represent combined transfection and transduction samples (2 independent experiments), with an n of 2-4 per experiment, per group. Data is presented as mean ± SEM. Data were analyzed by Kruskal-Wallis test with post hoc Dunn's multiple comparison testing. ** $p<0.01$, *** $p<0.001$, **** $p<0.0001$ versus ET1 A/B group. Abbreviations: ET-1, endothelin-1; A/B, ANP/BAY 60-2770; GA, GFP-APEX2; P5, PDE5; P9, PDE9.

PDE5 and PDE9 GFP-APEX2 fusion constructs co-localize with their corresponding endogenous PDE in isolated neonatal and adult cardiac myocytes

Correct cellular sublocalization of the fusion constructs was critical for the proposed labeling and pulldown experiments with APEX2, as without the correct localization, the resulting proteome would provide inaccurate information. In order to assess whether the fusion constructs localize correctly within the cell, immunofluorescent staining and confocal imaging was employed. Neonatal rat or adult rabbit cardiomyocytes were isolated and transduced with virus, and subsequently stained for either PDE5 or PDE9. Upon confocal imaging, colocalization was seen between GFP (marker for the fusion protein) and the appropriate PDE for both PDE5 and PDE9 in neonatal and adult myocytes (**Figure 4.3, A and B** respectively).

Figure 4.3: GFP-APEX2 signal colocalizes with respective PDE in neonatal and adult cardiomyocytes

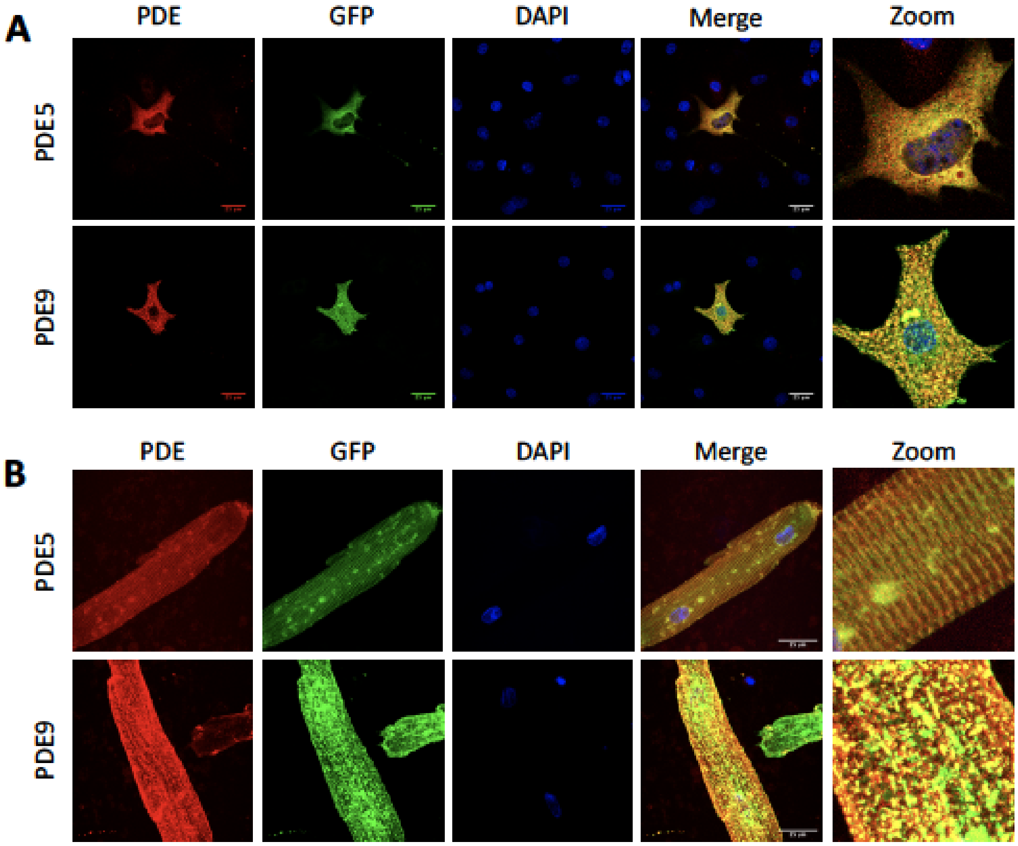

Figure 4.3: PDE and GFP signal colocalize in myocytes expressing the GFP-APEX2 fusion proteins

Cells were transduced with adenovirus expressing PDE5 or PDE9-GFP-APEX2. After 48 hours, cells were fixed and stained for either PDE5 or PDE9. Confocal imaging was performed, with images processed in Fiji. Scale bars represent 25 µM. A) Neonatal myocytes and B) adult myocytes expressing PDE5-GFP-APEX2 (top of each panel) and PDE9-GFP-APEX2 (bottom of each panel).

Biotinylation by the PDE fusion constructs is improved by the addition of N-acetyl cysteine, and unaffected by cycloheximide

Initial test studies of the APEX2 fusion constructs showed some background biotinylation in the absence of H_2O_2, indicating basal activity of APEX2. We hypothesized that addition of an antioxidant may lower background biotinylation by reducing oxidation and generation of free radicals (particularly the biotin-phenoxyl radical) in the cell. We therefore employed a common antioxidant, N-acetyl cysteine (NAC), and compared overall biotinylation levels via Western blot for the recommended biotinylation protocol versus the adapted protocol with the addition of NAC. Western blotting showed a dramatically increased level of biotinylation with addition of NAC as compared to the published protocol. While there was also increased background biotinylation in the absence of H_2O_2, the overall increase in amount of biotinylated proteins outweighed this background increase (**Figure 4.4A and B**, left side).

We furthermore wanted to optimize the biotinylation protocol to reduce non-compartment-specific biotinylation. Due to the nature of protein synthesis and transport within the cell, transport proteins and ribosomal machinery will inevitably be labeled by APEX2 as the fusion proteins are synthesized and transported to their final cellular location. We hypothesized that addition of cycloheximide (CHX), a protein synthesis inhibitor, would reduce this non-specific labeling, hence giving cleaner and therefore more accurate mass spectrometry results. Western blotting for biotinylated proteins showed that CHX had no impact on overall amounts of biotinylation, unlike the addition of NAC, and that this was the same whether CHX was employed in the published protocol for biotinylation, or the modified protocol with the addition of NAC (**Figure 4.4A and B**, right side).

Figure 4.4: N-acetylcysteine (NAC) increases overall biotinylation by APEX2, while cycloheximide has no impact

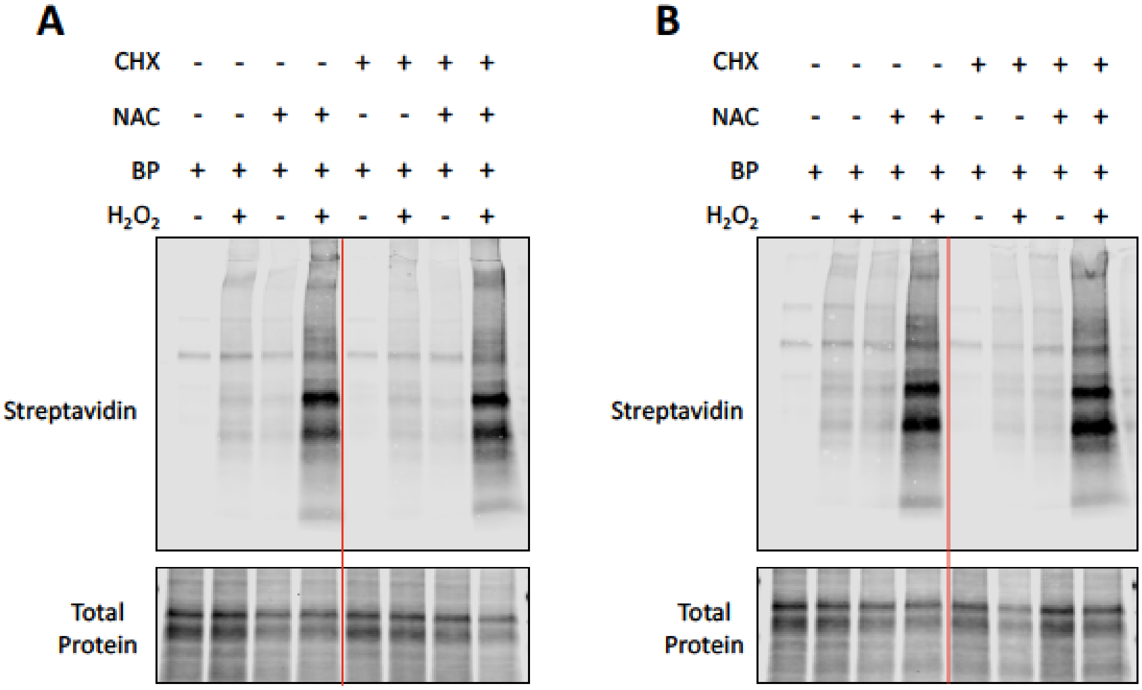

Figure 4.4: NAC increases biotinylation by GFP-APEX2-tagged PDE5 and PDE9. Neonatal rat myocytes were transduced with adPDE5 or adPDE9-GFP-APEX2. After 48 hours, a modified biotinylation protocol was performed in which cells were treated with N-acetylcysteine (NAC, 500 μM) and/or cycloheximide (CHX, 100 μM) two hours prior to addition of H_2O_2. Samples were then collected and run on an SDS-PAGE gel, and subsequently blotted for streptavidin (to detect biotinylated proteins) and total protein. A) adPDE5-GFP-APEX2 transduced cells and B) adPDE9-GFP-APEX2 transduced cells. Left of the red line on each panel are samples that were not treated with CHX, while right of the right line are samples that were treated with CHX. Abbreviations: CHX, cycloheximide; NAC, N-acetylcysteine; BP, biotin phenol.

Biotinylated proteins remain locally constrained within appropriate cellular nanodomains

The biotin-phenoxyl radicals generated by APEX2 during the biotinylation protocol have a short half-life, hence limiting the labeling radius to approximately 20 nm from the fusion protein. In order to determine whether the biotinylation was indeed remaining locally constrained within the PDE compartment, transduced adult rabbit cardiomyocytes were stained for biotinylated proteins with an Alexa fluor-streptavidin fusion antibody, and subsequently imaged via confocal microscopy. Colocalization was seen between GFP (marking the fusion protein) and biotinylated proteins for both PDE5 and PDE9 (**Figure 4.5**). This indicates that biotinylation is remaining within the compartment local to the fusion protein, which is critical for accurately identifying resident proteins of these compartments.

Figure 4.5: Biotinylated proteins remain constrained to the local PDE compartments in adult cardiomyocytes

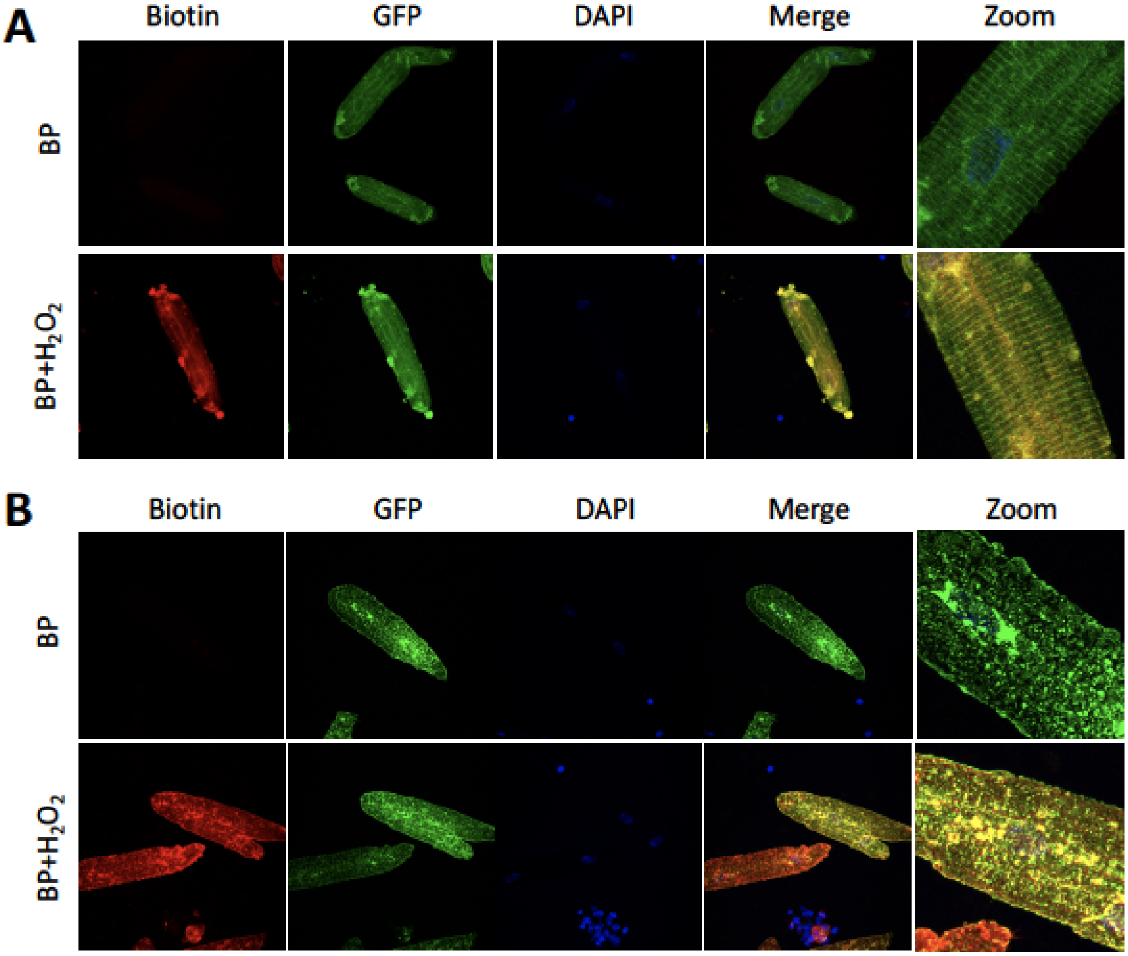

Figure 4.5: Biotinylated proteins colocalize with the GFP-APEX2-tagged PDEs

Adult rabbit cardiomyocytes were transduced with either A) PDE5-GFP-APEX2 or B) PDE9-GFP-APEX2. 48 hours later, biotinylation was performed and cells were fixed and stained for biotinylated proteins using an Alexa Fluor-tagged streptavidin. Cells were imaged by confocal, and images processed in Fiji. Abbreviations: BP, biotin-phenol.

Mass spectrometry of biotinylated proteins for both PDE5 and PDE9-APEX2 fusion constructs identifies few proteins

Rabbit myocytes were transduced with either adGFP-APEX2 or adPDE5 or PDE9-GFP-APEX2, and subjected to the modified biotinylation protocol including NAC and CHX. Immunoprecipitation was performed to isolate biotinylated proteins, which then underwent purification, digestion, labeling, and fractionation for LC-MS/MS. Statistical analysis of the subsequent identified peptides that were of high-confidence was performed in which a sample with biotin phenol and H_2O_2 was compared to a sample with only biotin phenol (i.e. adPDE5-GFP-APEX2+biotin phenol+H_2O_2 versus adPDE5-GFP-APEX2+ biotin phenol). This analysis identified few peptides as significant and had a high false discovery rate, indicating low confidence in the findings. This was true for both PDE5 and PDE9 results, with 24 proteins identified for PDE5 (**Table 4.3**) and 57 proteins identified for PDE9 (**Table 4.4**), both at $p<0.1$. Pathways analysis for proteins identified with PDE5-GFP-APEX2 found carbon metabolism, antibiotic synthesis, and glycine, serine, and threonine metabolism pathways were enriched (**Table 4.5**). For PDE9-GFP-APEX2, mitochondrial pathways were expected to be enriched, but were not (**Table 4.6**).

Further analysis was performed to determine potential reasons for the low confidence findings. In one analysis, the relative effect size of H_2O_2 was examined to determine if the expected effects (i.e. increased biotinylation) were actually occurring in the sample set (**Figure 4.6A-C**). These analyses showed that H_2O_2 was having a smaller effect size than anticipated, although it was seen to have a greater effect in the PDE5 and PDE9 data sets than the control GFP-APEX2 data set (mean F ratios of 1.22, 1.37, and 0.96 for PDE5, PDE9, and GFP-APEX2 control respectively). However, examination of the samples sent for mass spectrometry by Western blotting showed adequate increases in biotinylation between biotin phenol and biotin phenol with H_2O_2 groups, so it is uncertain why this effect appeared minimal after analysis of the mass spec data. ET-1 treatment was shown to have the largest effect size for all data sets (**Figure 4.6A-C**). Additional analyses of the data set examined sample clustering, which indicated that samples were forming unique clusters. Some sample groups clustered together, such as adPDE9-GFP-APEX2+biotin phenol+H_2O_2 and adPDE9-GFP-APEX2+ET-1+biotin phenol (**Figure 4.6D and E**).

Figure 4.6: Between-group analysis shows H_2O_2 does not contribute to variance as much as expected

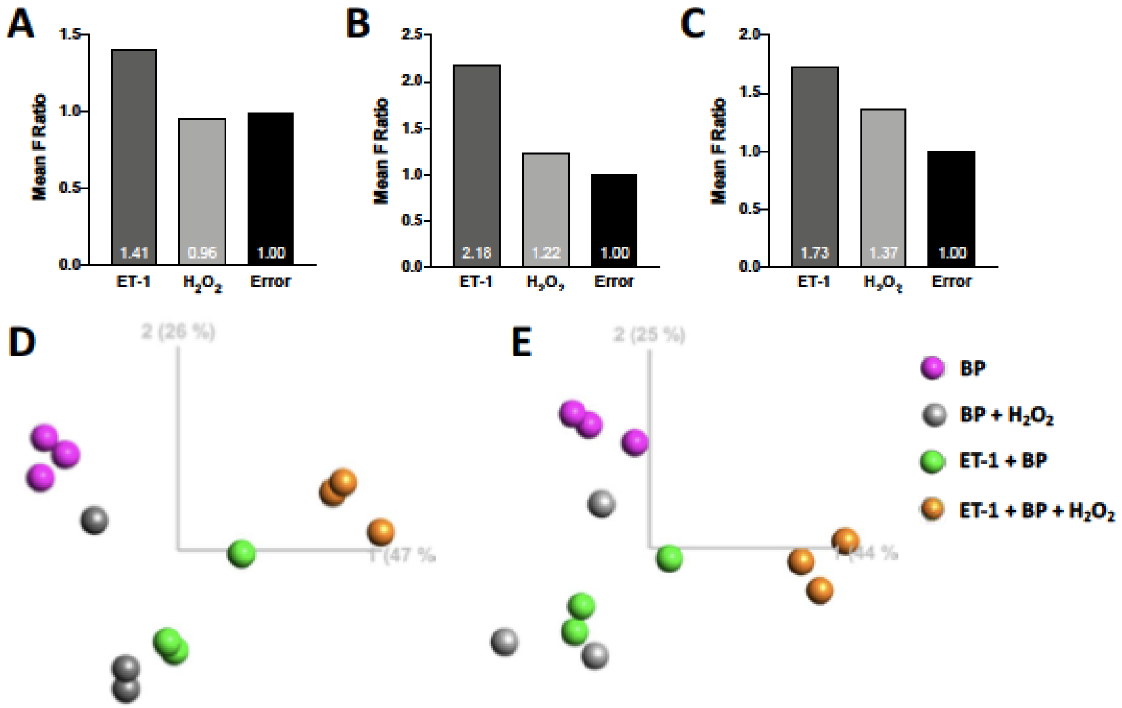

Figure 4.6: H_2O_2 is not the primary contributor to variance between groups

Mass spec sample groups were analyzed using LIMMA for factors contributing to variance, which showed that ET-1 was the primary contributor to variance between sample groups, while H_2O_2 had a relatively modest effect. This was true for A) GFP-APEX2, B) PDE5-GFP-APEX2, C) PDE9-GFP-APEX2, although GFP-APEX2 showed no impact of H_2O_2. Samples were also analyzed by principle components analysis, which showed samples within groups were generally clustered together for both D) PDE5-GFP-APEX2 and E) PDE9-GFP-APEX2. N=3 per sample group for panels D and E. Abbreviations: ET-1, endothelin-1; BP, biotin phenol.

Comparison of PDE9-FLAG co-immunoprecipitation data to PDE9-GFP-APEX2 mass spectrometry data shows little overlap

We next wanted to determine whether or not the APEX2 mass spectrometry data would overlap with our previously collected co-immunoprecipitation data for PDE9. The co-immunoprecipitation data showed PDE9 localizes at the mitochondria-sarcoplasmic reticulum interface, pulling down many mitochondrial energetics proteins as well as some SR proteins (Chapter 2 of this thesis). When this data set was compared to the APEX2 data set, only 6 proteins were found that overlapped between the two, one of which was PDE9 (**Figure 4.7**). The remaining five proteins were COX4, EIF4A1, MIC10, TLN1, and VDAC1. Three of these proteins (COX4, MIC10, and VDAC1) are mitochondrial, while EIF4A1 is involved in initiation of protein translation, and TLN1 is part of the costamere in cardiomyocytes.

Figure 4.7: Comparison of PDE9 APEX2 data to PDE9 co-immunoprecipitation data shows little overlap

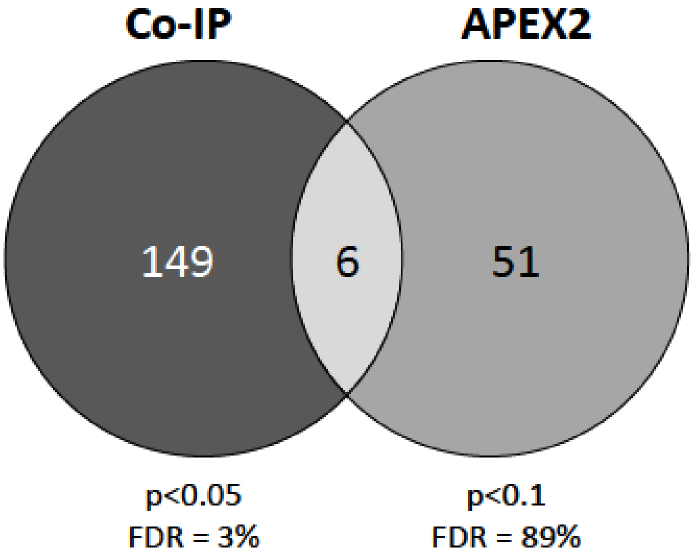

Figure 4.7: Minimal overlap between APEX2 and co-IP data sets for PDE9

After data analysis of the PDE9-GFP-APEX2 data set, significant proteins ($p<0.1$) were compared to significant proteins from the PDE9-FLAG co-immunoprecipitation experiment ($p<0.05$). Only 6 proteins overlapped between the data sets, indicating little congruence between experimental approaches. Abbreviations: FDR, false discovery rate.

DISCUSSION

This study is the first time that a proximity proteomics approach has been tested to examine PDE compartments. While this idea still holds merit and could be highly informative, modifications are clearly needed. APEX2-tagged PDE5 and PDE9 initially looked promising, as they appear to actively degrade cGMP, localize correctly, and biotinylate well. However, the mass spectrometry data did not provide much insight, with relatively few proteins identified as significant and a high false discovery rate amongst these few. Furthermore, among the proteins identified in the PDE9-GFP-APEX2 data set, only six overlapped with the PDE9-FLAG co-immunoprecipitation data set. The reasons for these results are unknown, as samples showed adequate increases in biotinylation by Western blotting. It is possible that the protocol modifications that we introduced (the addition of NAC and CHX) may have caused unforeseen difficulties with mass spec, but this is unknown without further testing. Sample processing and data analysis proceeded identically to the workflow used for the PDE9-FLAG co-immunoprecipitation experiment, which yielded high quality data with a low false discovery rate, so these are not the likely culprits. If APEX2 were to be tested again for studies of PDE compartmentation, one modification that could be made is to utilize a more lipid-soluble form of H_2O_2 such as tert-butyl peroxide to increase the amount of peroxide within the cell that can activate biotinylation, as membrane permeability of H_2O_2 is limited[168]. We would also recommend searching the data for the specific biotinylation modifications in order to get more informative results. This process is currently underway for the current data set, and may alter the results presented here.

For any future studies using proximity labeling techniques to examine PDE compartmentation, we would recommend that a different tag be used – for example, TurboID or miniTurbo, as these do not require the high dose of H_2O_2 for activation and subsequent labeling, yet still have relatively short labeling times. Additionally, the modified biotinylation protocol used here in which NAC was included would no longer be needed, since H_2O_2 is not used for either of these biotin ligases. Although the ability to perform electron microscopy studies is lost with these tags, the proximity proteomics workflow is simpler. We would also recommend adding cycloheximide to the samples (similar to what was done here). By adding cycloheximide, labeling of proteins near newly synthesized fusion proteins (either at the ribosome as it's being synthesized, or in vesicles as it's being transported) is avoided, providing cleaner mass spec data sets. However, it is unknown whether cycloheximide would significantly alter the catalytic efficiency of tags other than APEX2, so this would need to be tested.

Table 4.3: Significant proteins in PDE5-GFP-APEX2 analysis.

Mass spectrometry data was analyzed by LIMMA, comparing biotin-phenol to biotin-phenol with H_2O_2 samples. All proteins with a $p<0.1$ are shown, although the highest p value was 0.0464.

Gene Name	Protein Name	Fold Change with H2O2	P Value
ANXA1	Annexin A1	2.41	0.0017
DPYSL2	Dihydropyrimidinase-related protein 2	1.83	0.0060
DLST	Dihydrolipoyllysine-residue succinyltransferase component of 2-oxoglutarate dehydrogenase complex, mitochondrial	1.63	0.0089
PGAM2	Phosphoglycerate mutase 2	1.39	0.0095
FUS	RNA-binding protein FUS	1.70	0.0099
RABEP1	Rab GTPase-binding effector protein 1	3.03	0.0113
DIRAS2	GTP-binding protein Di-Ras2	3.04	0.0169
PPIA	Peptidyl-prolyl cis-trans isomerase A	1.88	0.0230
CTNNA1	Catenin alpha-1	1.77	0.0265
RSU1	Ras suppressor protein 1	1.50	0.0267
AK2	Adenylate kinase 2, mitochondrial	1.57	0.0274
RTCB	tRNA-splicing ligase RtcB homolog	1.61	0.0275
CFL1	Cofilin-1	1.95	0.0282
ANXA2	Annexin A2	1.72	0.0316
SEPT10	Septin-10	1.50	0.0344
PSMD4	26S proteasome non-ATPase regulatory subunit 4	1.51	0.0350
MSN	Moesin	1.46	0.0355
TLN1	Talin-1	1.54	0.0355
CDC37	Hsp90 co-chaperone Cdc37	1.83	0.0390
PGAM1	Phosphoglycerate mutase 1	1.29	0.0396
ESD	S-formylglutathione hydrolase	1.41	0.0444
CKAP4	Cytoskeleton-associated protein 4, partial	1.26	0.0447
TFG	Protein TFG	2.45	0.0452
LNPEP	Leucyl-cystinyl aminopeptidase	1.61	0.0464

Table 4.4: Significant proteins in PDE9-GFP-APEX2 analysis.

Mass spectrometry data was analyzed by LIMMA, comparing biotin-phenol to biotin-phenol with H_2O_2 samples. Rows highlighted in gray indicate proteins that overlapped with the PDE9-FLAG co-immunoprecipitation data set. All proteins with $p<0.1$ are shown.

Gene Name	Protein Name	Fold Change with H2O2	P Value
SLC25A1	Tricarboxylate transport protein, mitochondrial	1.50	0.0064
UBE2M	NEDD8-conjugating enzyme Ubc12	1.40	0.0131
EIF4A1	**Eukaryotic initiation factor 4A-I**	**1.40**	**0.0182**
KPNA3	Importin subunit alpha-4	1.51	0.0233
CYFIP1	Cytoplasmic FMR1-interacting protein 1	1.66	0.0235
ATPAF1	ATP synthase mitochondrial F1 complex assembly factor 1	1.58	0.0317
SDPR	Serum deprivation-response protein	1.92	0.0358
AKR7A3	Aflatoxin B1 aldehyde reductase member 3	1.36	0.0374
AKR1C5	Prostaglandin-E(2) 9-reductase-like	1.63	0.0380
HNRNPAB	Heterogeneous nuclear ribonucleoprotein A/B	1.52	0.0436
TMEM126A	Transmembrane protein 126A	1.34	0.0441
MSN	Moesin	1.58	0.0451
NARS	Asparagine--tRNA ligase, cytoplasmic	1.56	0.0455
L2HGDH	L-2-hydroxyglutarate dehydrogenase, mitochondrial	1.29	0.0486
FLNB	Filamin-B	1.38	0.0494
GSTM3	Glutathione S-transferase Mu 3	1.65	0.0513
ALDH1A1	Retinal dehydrogenase 1	1.78	0.0532
MRPS10	28S ribosomal protein S10, mitochondrial	1.31	0.0574
GSPT1	Eukaryotic peptide chain release factor GTP-binding subunit ERF3A	1.36	0.0575
THYN1	Thymocyte nuclear protein 1	1.51	0.0596
MICOS10	**MICOS complex subunit MIC10**	**1.28**	**0.0600**

D2HGDH	D-2-hydroxyglutarate dehydrogenase, mitochondrial	1.54	0.0607
CAMK2B	Calcium/calmodulin-dependent protein kinase type II subunit beta	1.26	0.0627
COX4	**Cytochrome c oxidase subunit 4 isoform 1, mitochondrial precursor**	**3.91**	**0.0634**
FAM120A	Constitutive coactivator of PPAR-gamma-like protein 1	1.63	0.0648
IDE	Insulin-degrading enzyme	1.39	0.0654
EIF5A2	Eukaryotic translation initiation factor 5A-2	1.44	0.0655
GNAI2	Guanine nucleotide-binding protein G(i) subunit alpha-2	1.67	0.0682
CAPRIN1	Caprin-1	1.60	0.0720
TLN1	**Talin-1**	**1.40**	**0.0767**
PRMT1	Protein arginine N-methyltransferase 1	1.31	0.0769
PTGES2	Prostaglandin E synthase 2	1.30	0.0771
RPS12	40S ribosomal protein S12	1.22	0.0779
PRKAA2	5'-AMP-activated protein kinase catalytic subunit alpha-2	1.36	0.0782
ARHGAP1	Rho GTPase-activating protein 1	1.24	0.0798
WARS	Tryptophan--tRNA ligase, cytoplasmic	1.26	0.0803
HSD17B10	3-hydroxyacyl-CoA dehydrogenase type-2	1.38	0.0816
RPL10A	60S ribosomal protein L10a	1.33	0.0842
NFKB2	Nuclear factor NF-kappa-B p100 subunit	1.49	0.0848
DHX15	Pre-mRNA-splicing factor ATP-dependent RNA helicase DHX15	1.33	0.0878
UBE2O	(E3-independent) E2 ubiquitin-conjugating enzyme	1.44	0.0893
GNAI1	Guanine nucleotide-binding protein G(i) subunit alpha-1	1.54	0.0901
FAM98A	Protein FAM98A	1.58	0.0902
MRPL16	39S ribosomal protein L16, mitochondrial	1.43	0.0912
CFL1	Cofilin-1	1.35	0.0913
STAT3	Signal transducer and activator of transcription 3	1.28	0.0915

GFM1	Elongation factor G, mitochondrial	1.25	0.0921
CBR1	Carbonyl reductase [NADPH] 1	1.34	0.0939
MIC26	MICOS complex subunit MIC26	1.30	0.0956
PDE9A	**High affinity cGMP-specific 3',5'-cyclic phosphodiesterase 9A**	**1.88**	**0.0966**
DPYSL2	Dihydropyrimidinase-related protein 2	1.30	0.0966
MPP1	55 kDa erythrocyte membrane protein	1.93	0.0967
VDAC1	**Voltage-dependent anion-selective channel protein 1**	**1.26**	**0.0972**
EIF3B	Eukaryotic translation initiation factor 3 subunit B	1.25	0.0973
RSU1	Ras suppressor protein 1	1.56	0.0975
CDC42	Cell division control protein 42 homolog	1.62	0.0988
DCTN3	Dynactin subunit 3	1.41	0.0991

Table 4.5: Pathways analysis for significant proteins from PDE5-GFP-APEX2 analysis.

Proteins from Table 1 were subjected to KEGG pathways analysis utilizing the DAVID database.

Term	P Value	Genes	Fold Enrichment
Carbon metabolism	0.0021	DLST, ESD, PGAM1, PGAM2	14.16
Biosynthesis of antibiotics	0.0127	DLST, PGAM1, PGAM2, AK2	7.48
Glycine, serine and threonine metabolism	0.0977	PGAM1, PGAM2	18.38

Table 4.6: Pathways analysis for significant proteins from PDE9-GFP-APEX2 analysis.

Proteins from Table 2 were subjected to KEGG pathways analysis utilizing the DAVID database.

Term	P Value	Genes	Fold Enrichment
Axon guidance	0.0025	CDC42, GNAI2, GNAI1, CFL1, DPYSL2	8.39
Proteoglycans in cancer	0.0133	CDC42, CAMK2B, MSN, FLNB, STAT3	5.22
Leukocyte transendothelial migration	0.0154	CDC42, GNAI2, GNAI1, MSN	7.36
Oxytocin signaling pathway	0.0315	GNAI2, GNAI1, CAMK2B, PRKAA2	5.59
Chemokine signaling pathway	0.0413	CDC42, GNAI2, GNAI1, STAT3	5.02
Pertussis	0.0446	GNAI2, GNAI1, CFL1	8.62
Gastric acid secretion	0.0457	GNAI2, GNAI1, CAMK2B	8.50
Circadian entrainment	0.0610	GNAI2, GNAI1, CAMK2B	7.23
Regulation of actin cytoskeleton	0.0706	CDC42, CFL1, CYFIP1, MSN	4.03
Melanogenesis	0.0711	GNAI2, GNAI1, CAMK2B	6.62
Glucagon signaling pathway	0.0738	PRMT1, CAMK2B, PRKAA2	6.49
Cholinergic synapse	0.0738	GNAI2, GNAI1, CAMK2B	6.49
Ribosome	0.0738	MRPL16, MRPS10, RPS12, RPL10A	3.96
Rap1 signaling pathway	0.0831	CDC42, TLN1, GNAI2, GNAI1	3.76

CHAPTER 5: General Discussion and Conclusions

In this dissertation, I studied the compartmentation of PDE5 and PDE9 in the heart. First, I examined transcriptomic regulation in the heart under pressure-overload stress by each of these two different cGMP-selective PDEs, testing their differential impact on both overall gene expression and on microRNA expression. I then examined the localized nanodomains in isolated cardiac myocytes using co-immunoprecipitation and biotinylation strategies coupled with mass spectrometry.

In chapter two, I tested the hypothesis that inhibition of either PDE5 or PDE9 in a mouse pressure-overload model of heart failure would lead to miRNA and mRNA changes that were specific to nanodomain control by PDE5 and PDE9. In this study, I demonstrated that despite similar phenotypic improvement following PDE5 and PDE9 inhibition in the mouse pressure overload model, there is a virtually binary difference in their impact on miRNA expression. PDE5 inhibition broadly downregulated miRNAs, reversing most that are enhanced by pressure-overload stress and lowering many others that were not themselves increased by the disease stress. By contrast, PDE9 inhibition altered almost no miRNAs when compared to the pressure-overload heart treated with vehicle. Despite this striking difference, RNA-seq analysis of mRNA expression revealed both treatments targeted many genes that converged on similar signaling pathways. However, the genes themselves were largely different, further revealing underlying disparities in the signaling impact from the two different methods to stimulate the cGMP/PKG signalosome. With respect to miRNA expression, I found the phenotype arises at the level of mature miRNAs, as earlier forms of miRNAs generated within the nucleus were similar between PDE-inhibitor treatment groups. The difference in processing was not ascribable to changes in expression of miRNA processing genes, though other mechanisms including post-translational changes in their activity remain to be determined. Furthermore, by demonstrating that the striking cardiac miRNA profile change following PDE5 inhibition was both organ and disease specific, it is unlikely that its impact requires a general alteration of fundamental miRNA processing. I further showed that targeting cGMP/PKG activation even within the same pathway - NO-sGC-PDE5 – but by different means does not translate to identical changes in miRNA expression. Specifically, activating sGC results in downregulation of miRNAs that were increased by pressure-overload stress (pro-hypertrophic), similar to changes with PDE5 inhibition. By contrast, miRNAs that declined with pressure-overload (anti-hypertrophic) were further reduced by PDE5 inhibition, but broadly unchanged by sGC stimulation. This speaks further to the critical role of compartmentalization even of different components within the same signaling pathway, and how this can alter downstream transcriptional changes. The results suggest that using miRNAs as a biomarker for phenotypic improvement following therapy, as tested here for pathological cardiac hypertrophy, can be misleading, as I demonstrate that several different treatments that confer nearly identical phenotypic improvement of the diseased heart do so with dramatically different miRNA expression profiles.

In chapter three, I defined the nanodomain of PDE9 in cardiac myocytes by co-immunoprecipitation and mass spectrometry to identify binding partners of PDE9 under both normal and hypertrophic conditions. I determined that PDE9 resides primarily at the mitochondria, and that it also interacts with proteins in the sarcoplasmic reticulum. This likely places PDE9 at the dyadic cleft, where the SR and mitochondrial membranes are physically close. This region plays a key role in calcium-sensing and ATP homeostasis. Pathways analysis of significant proteins identified metabolic pathways associated with mitochondria such as oxidative phosphorylation, citric acid cycle, and fatty acid oxidation, as well as calcium signaling pathways associated with the sarcoplasmic reticulum. No significant alterations were seen with endothelin treatment to stimulate hypertrophy, indicating that PDE9 does not relocalize under hypertrophic conditions.

In chapter four, I developed novel reagents to study PDE5 and PDE9 nanodomains in adult cardiomyocytes utilizing the proximity proteomics approach of APEX2 tagging. Constructs were generated expressing GFP-APEX2-tagged PDE5 and PDE9, which were determined to actively hydrolyze cGMP, localize to their correct subcellular domain, and biotinylate nearby proteins. The biotinylation protocol was optimized by the addition of the antioxidant N-acetylcysteine and the protein synthesis inhibitor cycloheximide, to increase overall biotinylation and decrease off-target biotinylation, respectively. Despite the clear success of the underlying experiment to produce a substantial increase in biotinylated proteins upon APEX2 activation, the mass spectrometry and subsequent bioinformatics were not optimized to detect residues that were modified by biotin. This needs to be corrected to detect those proteins that were truly altered, and ongoing efforts aim to do this. The data I did obtain is more consistent with the total protein gels for these experiments after the biotin pull-down, which showed approximately equal protein across the various samples, regardless of biotinylation levels. I hypothesize that non-biotinylated proteins that were bound to the specifically biotinylated proteins were also pulled down, and therefore I was unable to determine which were truly biotinylated. This likely led to a very high false discovery rate, few hits, and little overlap with the FLAG-pulldown data. This will require further bioinformatics modifications, which are underway. Another feature of APEX2 is its ability to provide electron microscopic detection without the need for an antibody. This work remains to be performed, but can also provide nanodomain localization data.

In summary, I have shown that inhibition of PDE5 and PDE9 have highly differential impacts on miRNA regulation in a mouse heart failure model despite similar phenotypic improvement, indicating that compartmentation of enzymes is critical for their downstream signaling effects. This study further demonstrated that miRNAs are not a reliable biomarker readout for treatment efficacy in heart failure. I have also shown that PDE9 is localized to mitochondria in cardiomyocytes, where it interacts with many metabolic proteins. It also interfaces with the sarcoplasmic reticulum to potentially regulate calcium signaling. This data indicates that therapeutically targeting PDE9 may be of benefit in metabolically-linked diseases.

REFERENCES

1. Maurice DH, Ke H, Ahmad F, Wang Y, Chung J and Manganiello VC. Advances in targeting cyclic nucleotide phosphodiesterases. *Nature Reviews Drug Discovery*. 2014;13:290-314.

2. Francis SH, Blount MA and Corbin JD. Mammalian cyclic nucleotide phosphodiesterases: molecular mechanisms and physiological functions. *Physiol Rev*. 2011;91:651-90.

3. Bender AT and Beavo JA. Cyclic nucleotide phosphodiesterases: molecular regulation to clinical use. *Pharmacological reviews*. 2006;58:488-520.

4. Ke H and Wang H. Crystal Structures of Phosphodiesterases and Implications on Substrate Specificity and Inhibitor Selectivity. *Current Topics in Medicinal Chemistry*. 2007;7:391-403.

5. Card GL, England BP, Suzuki Y, Fong D, Powell B, Lee B, Luu C, Tabrizizad M, Gillette S, Ibrahim PN, Artis DR, Bollag G, Milburn MV, Kim S-H, Schlessinger J and Zhang KYJ. Structural Basis for the Activity of Drugs that Inhibit Phosphodiesterases. *Structure*. 2004;12:2233-2247.

6. Meng F, Hou J, Shao Y-X, Wu P-Y, Huang M, Zhu X, Cai Y, Li Z, Xu J, Liu P, Luo H-B, Wan Y and Ke H. Structure-Based Discovery of Highly Selective Phosphodiesterase-9A Inhibitors and Implications for Inhibitor Design. *Journal of Medicinal Chemistry*. 2012;55:8549-8558.

7. Claffey MM, Helal CJ, Verhoest PR, Kang Z, Fors KS, Jung S, Zhong J, Bundesmann MW, Hou X, Lui S, Kleiman RJ, Vanase-Frawley M, Schmidt AW, Menniti F, Schmidt CJ, Hoffman WE, Hajos M, McDowell L, O'Connor RE, MacDougall-Murphy M,

Fonseca KR, Becker SL, Nelson FR and Liras S. Application of Structure-Based Drug Design and Parallel Chemistry to Identify Selective, Brain Penetrant, In Vivo Active Phosphodiesterase 9A Inhibitors. *Journal of Medicinal Chemistry*. 2012;55:9055-9068.

8. Pandit J, Forman MD, Fennell KF, Dillman KS and Menniti FS. Mechanism for the allosteric regulation of phosphodiesterase 2A deduced from the X-ray structure of a near full-length construct. *Proc Natl Acad Sci U S A*. 2009;106:18225-30.

9. Houslay MD. Underpinning compartmentalised cAMP signalling through targeted cAMP breakdown. *Trends Biochem Sci*. 2010;35:91-100.

10. Reeves ML, Leigh BK and England PJ. The identification of a new cyclic nucleotide phosphodiesterase activity in human and guinea-pig cardiac ventricle. Implications for the mechanism of action of selective phosphodiesterase inhibitors. *Biochem J*. 1987;241:535-41.

11. Conti M and Beavo J. Biochemistry and physiology of cyclic nucleotide phosphodiesterases: essential components in cyclic nucleotide signaling. *Annu Rev Biochem*. 2007;76:481-511.

12. Mattick P, Parrington J, Odia E, Simpson A, Collins T and Terrar D. Ca2+-stimulated adenylyl cyclase isoform AC1 is preferentially expressed in guinea-pig sino-atrial node cells and modulates the I(f) pacemaker current. *J Physiol*. 2007;582:1195-203.

13. Zaccolo M. cAMP signal transduction in the heart: understanding spatial control for the development of novel therapeutic strategies. *British Journal of Pharmacology*. 2009;158:50-60.

14. Ruiz-Hurtado G, Morel E, Domínguez-Rodríguez A, Llach A, Lezoualc'h F, Benitah J-P and Gomez AM. Epac in cardiac calcium signaling. *Journal of Molecular and Cellular Cardiology*. 2013;58:162-171.

15. Mayr B and Montminy M. Transcriptional regulation by the phosphorylation-dependent factor CREB. *Nat Rev Mol Cell Biol*. 2001;2:599-609.

16. Lolicato M, Bucchi A, Arrigoni C, Zucca S, Nardini M, Schroeder I, Simmons K, Aquila M, DiFrancesco D, Bolognesi M, Schwede F, Kashin D, Fishwick CW, Johnson AP, Thiel G and Moroni A. Cyclic dinucleotides bind the C-linker of HCN4 to control channel cAMP responsiveness. *Nat Chem Biol*. 2014;10:457-62.

17. Baruscotti M, Bucchi A, Viscomi C, Mandelli G, Consalez G, Gnecchi-Rusconi T, Montano N, Casali KR, Micheloni S, Barbuti A and DiFrancesco D. Deep bradycardia and heart block caused by inducible cardiac-specific knockout of the pacemaker channel gene Hcn4. *Proc Natl Acad Sci U S A*. 2011;108:1705-10.

18. Alig J, Marger L, Mesirca P, Ehmke H, Mangoni ME and Isbrandt D. Control of heart rate by cAMP sensitivity of HCN channels. *Proc Natl Acad Sci U S A*. 2009;106:12189-94.

19. Liao Z, Lockhead D, Larson ED and Proenza C. Phosphorylation and modulation of hyperpolarization-activated HCN4 channels by protein kinase A in the mouse sinoatrial node. *J Gen Physiol*. 2010;136:247-58.

20. Tsai EJ and Kass DA. Cyclic GMP signaling in cardiovascular pathophysiology and therapeutics. *Pharmacology & therapeutics*. 2009;122:216-238.

21. Tsai EJ, Liu Y, Koitabashi N, Bedja D, Danner T, Jasmin JF, Lisanti MP, Friebe A, Takimoto E and Kass DA. Pressure-overload-induced subcellular relocalization/oxidation of soluble guanylyl cyclase in the heart modulates enzyme stimulation. *Circ Res*. 2012;110:295-303.

22. Zabel U, Kleinschnitz C, Oh P, Nedvetsky P, Smolenski A, Muller H, Kronich P, Kugler P, Walter U, Schnitzer JE and Schmidt HH. Calcium-dependent membrane association sensitizes soluble guanylyl cyclase to nitric oxide. *Nat Cell Biol*. 2002;4:307-11.

23. Balligand JL. Beta3-adrenoreceptors in cardiovasular diseases: new roles for an "old" receptor. *Curr Drug Deliv*. 2013;10:64-6.

24. Belge C, Hammond J, Dubois-Deruy E, Manoury B, Hamelet J, Beauloye C, Markl A, Pouleur AC, Bertrand L, Esfahani H, Jnaoui K, Gotz KR, Nikolaev VO, Vanderper A, Herijgers P, Lobysheva I, Iaccarino G, Hilfiker-Kleiner D, Tavernier G, Langin D, Dessy C and Balligand JL. Enhanced expression of beta3-adrenoceptors in cardiac myocytes attenuates neurohormone-induced hypertrophic remodeling through nitric oxide synthase. *Circulation*. 2014;129:451-62.

25. Lee DI, Vahebi S, Tocchetti CG, Barouch LA, Solaro RJ, Takimoto E and Kass DA. PDE5A suppression of acute beta-adrenergic activation requires modulation of myocyte beta-3 signaling coupled to PKG-mediated troponin I phosphorylation. *Basic Res Cardiol*. 2010;105:337-47.

26. Kinoshita H, Kuwahara K, Nishida M, Jian Z, Rong X, Kiyonaka S, Kuwabara Y, Kurose H, Inoue R, Mori Y, Li Y, Nakagawa Y, Usami S, Fujiwara M, Yamada Y, Minami T, Ueshima K and Nakao K. Inhibition of TRPC6 channel activity contributes to the antihypertrophic effects of natriuretic peptides-guanylyl cyclase-A signaling in the heart. *Circ Res*. 2010;106:1849-60.

27. Koitabashi N, Aiba T, Hesketh GG, Rowell J, Zhang M, Takimoto E, Tomaselli GF and Kass DA. Cyclic GMP/PKG-dependent inhibition of TRPC6 channel activity and expression negatively regulates cardiomyocyte NFAT activation: Novel mechanism of

cardiac stress modulation by PDE5 inhibition. *Journal of Molecular and Cellular Cardiology*. 2010;48:713-724.

28. Takimoto E, Koitabashi N, Hsu S, Ketner EA, Zhang M, Nagayama T, Bedja D, Gabrielson KL, Blanton R, Siderovski DP, Mendelsohn ME and Kass DA. Regulator of G protein signaling 2 mediates cardiac compensation to pressure overload and antihypertrophic effects of PDE5 inhibition in mice. *J Clin Invest*. 2009;119:408-20.

29. Tang KM, Wang GR, Lu P, Karas RH, Aronovitz M, Heximer SP, Kaltenbronn KM, Blumer KJ, Siderovski DP, Zhu Y and Mendelsohn ME. Regulator of G-protein signaling-2 mediates vascular smooth muscle relaxation and blood pressure. *Nat Med*. 2003;9:1506-12.

30. Tokudome T, Kishimoto I, Horio T, Arai Y, Schwenke DO, Hino J, Okano I, Kawano Y, Kohno M, Miyazato M, Nakao K and Kangawa K. Regulator of G-protein signaling subtype 4 mediates antihypertrophic effect of locally secreted natriuretic peptides in the heart. *Circulation*. 2008;117:2329-39.

31. Layland J, Solaro RJ and Shah AM. Regulation of cardiac contractile function by troponin I phosphorylation. *Cardiovasc Res*. 2005;66:12-21.

32. Thoonen R, Giovanni S, Govindan S, Lee DI, Wang GR, Calamaras TD, Takimoto E, Kass DA, Sadayappan S and Blanton RM. Molecular Screen Identifies Cardiac Myosin-Binding Protein-C as a Protein Kinase G-Ialpha Substrate. *Circ Heart Fail*. 2015;8:1115-22.

33. Corbin JD, Turko IV, Beasley A and Francis SH. Phosphorylation of phosphodiesterase-5 by cyclic nucleotide-dependent protein kinase alters its catalytic and allosteric cGMP-binding activities. *Eur J Biochem*. 2000;267:2760-7.

34. Ranek MJ, Terpstra EJM, Li J, Kass DA and Wang X. Protein Kinase G Positively Regulates Proteasome-Mediated Degradation of Misfolded Proteins. *Circulation*. 2013;128:365-376.

35. Lee DI and Kass DA. Phosphodiesterases and Cyclic GMP Regulation in Heart Muscle. *Physiology*. 2012;27:248-258.

36. McConnachie G, Langeberg LK and Scott JD. AKAP signaling complexes: getting to the heart of the matter. *Trends Mol Med*. 2006;12:317-23.

37. Reger AS, Yang MP, Koide-Yoshida S, Guo E, Mehta S, Yuasa K, Liu A, Casteel DE and Kim C. Crystal structure of the cGMP-dependent protein kinase II leucine zipper and Rab11b protein complex reveals molecular details of G-kinase-specific interactions. *J Biol Chem*. 2014;289:25393-403.

38. Kato M, Blanton R, Wang GR, Judson TJ, Abe Y, Myoishi M, Karas RH and Mendelsohn ME. Direct binding and regulation of RhoA protein by cyclic GMP-dependent protein kinase Ialpha. *J Biol Chem*. 2012;287:41342-51.

39. Lee E, Hayes DB, Langsetmo K, Sundberg EJ and Tao TC. Interactions between the leucine-zipper motif of cGMP-dependent protein kinase and the C-terminal region of the targeting subunit of myosin light chain phosphatase. *J Mol Biol*. 2007;373:1198-212.

40. Sprenger JU, Perera RK, Steinbrecher JH, Lehnart SE, Maier LS, Hasenfuss G and Nikolaev VO. In vivo model with targeted cAMP biosensor reveals changes in receptor-microdomain communication in cardiac disease. *Nat Commun*. 2015;6.

41. Götz KR, Sprenger JU, Perera RK, Steinbrecher JH, Lehnart SE, Kuhn M, Gorelik J, Balligand J-L and Nikolaev VO. Transgenic Mice for Real-Time Visualization of cGMP in Intact Adult Cardiomyocytes. *Circulation Research*. 2014;114:1235-1245.

42. Thunemann M, Wen L, Hillenbrand M, Vachaviolos A, Feil S, Ott T, Han X, Fukumura D, Jain RK, Russwurm M, de Wit C and Feil R. Transgenic mice for cGMP imaging. *Circ Res*. 2013;113:365-71.

43. Perera RK, Sprenger JU, Steinbrecher JH, Hubscher D, Lehnart SE, Abesser M, Schuh K, El-Armouche A and Nikolaev VO. Microdomain switch of cGMP-regulated phosphodiesterases leads to ANP-induced augmentation of beta-adrenoceptor-stimulated contractility in early cardiac hypertrophy. *Circ Res*. 2015;116:1304-11.

44. Götz KR and Nikolaev VO. Advances and Techniques to Measure cGMP in Intact Cardiomyocytes. In: T. Krieg and R. Lukowski, eds. *Guanylate Cyclase and Cyclic GMP: Methods and Protocols* Totowa, NJ: Humana Press; 2013: 121-129.

45. Niino Y, Hotta K and Oka K. Simultaneous Live Cell Imaging Using Dual FRET Sensors with a Single Excitation Light. *PLoS ONE*. 2009;4:e6036.

46. Calamera G, Ulsund AH, Manfra O, Kim JJ, Kim C, Levy FO and Andressen KW. Construction of novel cGMP FRET-sensors based on PKG from Plasmodium falciparum. *BMC Pharmacology & Toxicology*. 2015;16:A34-A34.

47. Nausch LWM, Ledoux J, Bonev AD, Nelson MT and Dostmann WR. Differential patterning of cGMP in vascular smooth muscle cells revealed by single GFP-linked biosensors. *Proceedings of the National Academy of Sciences*. 2008;105:365-370.

48. Lee DI, Zhu G, Sasaki T, Cho G-S, Hamdani N, Holewinski R, Jo S-H, Danner T, Zhang M and Rainer PP. Phosphodiesterase 9A controls nitric-oxide-independent cGMP and hypertrophic heart disease. *Nature*. 2015.

49. Bhargava Y, Hampden-Smith K, Chachlaki K, Wood K, Vernon J, Allerston CK, Batchelor AM and Garthwaite J. Improved genetically-encoded, FlincG-type fluorescent biosensors for neural cGMP imaging. *Frontiers in Molecular Neuroscience*. 2013;6.

50. Di Benedetto G, Zoccarato A, Lissandron V, Terrin A, Li X, Houslay MD, Baillie GS and Zaccolo M. Protein Kinase A Type I and Type II Define Distinct Intracellular Signaling Compartments. *Circulation Research*. 2008;103:836-844.

51. Stangherlin A, Gesellchen F, Zoccarato A, Terrin A, Fields LA, Berrera M, Surdo NC, Craig MA, Smith G, Hamilton G and Zaccolo M. cGMP Signals Modulate cAMP Levels in a Compartment-Specific Manner to Regulate Catecholamine-Dependent Signaling in Cardiac Myocytes. *Circulation Research*. 2011;108:929-939.

52. Sroubek J and McDonald TV. Protein Kinase A Activity at the Endoplasmic Reticulum Surface Is Responsible for Augmentation of Human ether-a-go-go-related Gene Product (HERG). *Journal of Biological Chemistry*. 2011;286:21927-21936.

53. Castro LRV, Verde I, Cooper DMF and Fischmeister R. Cyclic Guanosine Monophosphate Compartmentation in Rat Cardiac Myocytes. *Circulation*. 2006;113:2221-2228.

54. Roux KJ, Kim DI, Raida M and Burke B. A promiscuous biotin ligase fusion protein identifies proximal and interacting proteins in mammalian cells. *J Cell Biol*. 2012;196:801-10.

55. Kim DI, Jensen SC, Noble KA, Kc B, Roux KH, Motamedchaboki K and Roux KJ. An improved smaller biotin ligase for BioID proximity labeling. *Mol Biol Cell*. 2016;27:1188-96.

56. Branon TC, Bosch JA, Sanchez AD, Udeshi ND, Svinkina T, Carr SA, Feldman JL, Perrimon N and Ting AY. Efficient proximity labeling in living cells and organisms with TurboID. *Nat Biotechnol*. 2018;36:880-887.

57. Rhee HW, Zou P, Udeshi ND, Martell JD, Mootha VK, Carr SA and Ting AY. Proteomic mapping of mitochondria in living cells via spatially restricted enzymatic tagging. *Science (New York, NY)*. 2013;339:1328-1331.

58. Lam SS, Martell JD, Kamer KJ, Deerinck TJ, Ellisman MH, Mootha VK and Ting AY. Directed evolution of APEX2 for electron microscopy and proximity labeling. *Nat Methods*. 2015;12:51-4.

59. Martell JD, Deerinck TJ, Sancak Y, Poulos TL, Mootha VK, Sosinsky GE, Ellisman MH and Ting AY. Engineered ascorbate peroxidase as a genetically encoded reporter for electron microscopy. *Nat Biotechnol.* 2012;30:1143-8.

60. Lin CS, Lau A, Tu R and Lue TF. Expression of three isoforms of cGMP-binding cGMP-specific phosphodiesterase (PDE5) in human penile cavernosum. *Biochem Biophys Res Commun.* 2000;268:628-35.

61. Thomas MK, Francis SH and Corbin JD. Characterization of a purified bovine lung cGMP-binding cGMP phosphodiesterase. *Journal of Biological Chemistry.* 1990;265:14964-14970.

62. Kass D. Cardiac Role of Cyclic-GMP Hydrolyzing Phosphodiesterase Type 5: From Experimental Models to Clinical Trials. *Current Heart Failure Reports.* 2012;9:192-199.

63. Takimoto E, Belardi D, Tocchetti CG, Vahebi S, Cormaci G, Ketner EA, Moens AL, Champion HC and Kass DA. Compartmentalization of Cardiac β-Adrenergic Inotropy Modulation by Phosphodiesterase Type 5. *Circulation.* 2007;115:2159-2167.

64. Takimoto E, Champion HC, Belardi D, Moslehi J, Mongillo M, Mergia E, Montrose DC, Isoda T, Aufiero K, Zaccolo M, Dostmann WR, Smith CJ and Kass DA. cGMP catabolism by phosphodiesterase 5A regulates cardiac adrenergic stimulation by NOS3-dependent mechanism. *Circulation research.* 2005;96:100-109.

65. Takimoto E, Champion HC, Li M, Belardi D, Ren S, Rodriguez ER, Bedja D, Gabrielson KL, Wang Y and Kass DA. Chronic inhibition of cyclic GMP phosphodiesterase 5A prevents and reverses cardiac hypertrophy. *Nature medicine.* 2005;11:214-222.

66. Salloum FN, Abbate A, Das A, Houser J-E, Mudrick CA, Qureshi IZ, Hoke NN, Roy SK, Brown WR, Prabhakar S and Kukreja RC. Sildenafil (Viagra) attenuates ischemic

cardiomyopathy and improves left ventricular function in mice. *American Journal of Physiology - Heart and Circulatory Physiology*. 2008;294:H1398-H1406.

67. Kass DA, Champion HC and Beavo JA. Phosphodiesterase Type 5: Expanding Roles in Cardiovascular Regulation. *Circulation Research*. 2007;101:1084-1095.

68. Ockaili R, Salloum F, Hawkins J and Kukreja RC. Sildenafil (Viagra) induces powerful cardioprotective effect via opening of mitochondrial KATP channels in rabbits. *American Journal of Physiology - Heart and Circulatory Physiology*. 2002;283:H1263-H1269.

69. Salloum FN, Ockaili RA, Wittkamp M, Marwaha VR and Kukreja RC. Vardenafil: a novel type 5 phosphodiesterase inhibitor reduces myocardial infarct size following ischemia/reperfusion injury via opening of mitochondrial KATP channels in rabbits. *Journal of Molecular and Cellular Cardiology*. 2006;40:405-411.

70. Das A, Smolenski A, Lohmann SM and Kukreja RC. Cyclic GMP-dependent Protein Kinase Ia Attenuates Necrosis and Apoptosis Following Ischemia/Reoxygenation in Adult Cardiomyocyte. *Journal of Biological Chemistry*. 2006;281:38644-38652.

71. Zhang M, Koitabashi N, Nagayama T, Rambaran R, Feng N, Takimoto E, Koenke T, O'Rourke B, Champion HC, Crow MT and Kass DA. Expression, activity, and pro-hypertrophic effects of PDE5A in cardiac myocytes. *Cellular Signalling*. 2008;20:2231-2236.

72. Senzaki H, Smith CJ, Juang GJ, Isoda T, Mayer SP, Ohler A, Paolocci N, Tomaselli GF, Hare JM and Kass DA. Cardiac phosphodiesterase 5 (cGMP-specific) modulates β-adrenergic signaling in vivo and is down-regulated in heart failure. *The FASEB Journal*. 2001;15:1718-1726.

73. Zhang M, Takimoto E, Lee DI, Santos CX, Nakamura T, Hsu S, Jiang A, Nagayama T, Bedja D, Yuan Y, Eaton P, Shah AM and Kass DA. Pathological cardiac hypertrophy

alters intracellular targeting of phosphodiesterase type 5 from nitric oxide synthase-3 to natriuretic peptide signaling. *Circulation*. 2012;126:942-51.

74. Koka S, Das A, Zhu SG, Durrant D, Xi L and Kukreja RC. Long-acting phosphodiesterase-5 inhibitor tadalafil attenuates doxorubicin-induced cardiomyopathy without interfering with chemotherapeutic effect. *J Pharmacol Exp Ther*. 2010;334:1023-30.

75. Guazzi M, Vicenzi M and Arena R. Phosphodiesterase 5 inhibition with sildenafil reverses exercise oscillatory breathing in chronic heart failure: a long-term cardiopulmonary exercise testing placebo-controlled study. *Eur J Heart Fail*. 2012;14:82-90.

76. Guazzi M, Vicenzi M, Arena R and Guazzi MD. PDE5 inhibition with sildenafil improves left ventricular diastolic function, cardiac geometry, and clinical status in patients with stable systolic heart failure: results of a 1-year, prospective, randomized, placebo-controlled study. *Circ Heart Fail*. 2011;4:8-17.

77. Redfield MM, Chen HH, Borlaug BA, Semigran MJ, Lee KL, Lewis G, LeWinter MM, Rouleau JL, Bull DA and Mann DL. Effect of phosphodiesterase-5 inhibition on exercise capacity and clinical status in heart failure with preserved ejection fraction: a randomized clinical trial. *Jama*. 2013;309:1268-1277.

78. Moens AL, Takimoto E, Tocchetti CG, Chakir K, Bedja D, Cormaci G, Ketner EA, Majmudar M, Gabrielson K, Halushka MK, Mitchell JB, Biswal S, Channon KM, Wolin MS, Alp NJ, Paolocci N, Champion HC and Kass DA. Reversal of cardiac hypertrophy and fibrosis from pressure overload by tetrahydrobiopterin: efficacy of recoupling nitric oxide synthase as a therapeutic strategy. *Circulation*. 2008;117:2626-36.

79. Takimoto E, Champion HC, Li M, Ren S, Rodriguez ER, Tavazzi B, Lazzarino G, Paolocci N, Gabrielson KL, Wang Y and Kass DA. Oxidant stress from nitric oxide

synthase-3 uncoupling stimulates cardiac pathologic remodeling from chronic pressure load. *J Clin Invest*. 2005;115:1221-31.

80. Neo BH, Kandhi S and Wolin MS. Roles for redox mechanisms controlling protein kinase G in pulmonary and coronary artery responses to hypoxia. *Am J Physiol Heart Circ Physiol*. 2011;301:H2295-304.

81. Karbach S, Wenzel P, Waisman A, Munzel T and Daiber A. eNOS uncoupling in cardiovascular diseases--the role of oxidative stress and inflammation. *Curr Pharm Des*. 2014;20:3579-94.

82. Carnicer R, Crabtree MJ, Sivakumaran V, Casadei B and Kass DA. Nitric oxide synthases in heart failure. *Antioxidants & redox signaling*. 2013;18:1078-1099.

83. Sasaki H, Nagayama T, Blanton RM, Seo K, Zhang M, Zhu G, Lee DI, Bedja D, Hsu S, Tsukamoto O, Takashima S, Kitakaze M, Mendelsohn ME, Karas RH, Kass DA and Takimoto E. PDE5 inhibitor efficacy is estrogen dependent in female heart disease. *J Clin Invest*. 2014;124:2464-71.

84. van Veldhuisen DJ, Linssen GCM, Jaarsma T, van Gilst WH, Hoes AW, Tijssen JGP, Paulus WJ, Voors AA and Hillege HL. B-Type Natriuretic Peptide and Prognosis in Heart Failure Patients With Preserved and Reduced Ejection Fraction. *Journal of the American College of Cardiology*. 2013;61:1498-1506.

85. van Heerebeek L, Hamdani N, Falcão-Pires I, Leite-Moreira AF, Begieneman MPV, Bronzwaer JGF, van der Velden J, Stienen GJM, Laarman GJ, Somsen A, Verheugt FWA, Niessen HWM and Paulus WJ. Low Myocardial Protein Kinase G Activity in Heart Failure With Preserved Ejection Fraction. *Circulation*. 2012;126:830-839.

86. Fisher DA, Smith JF, Pillar JS, Denis SHS and Cheng JB. Isolation and Characterization of PDE9A, a Novel Human cGMP-specific Phosphodiesterase. *Journal of Biological Chemistry*. 1998;273:15559-15564.

87. Soderling SH, Bayuga SJ and Beavo JA. Identification and characterization of a novel family of cyclic nucleotide phosphodiesterases. *J Biol Chem*. 1998;273:15553-8.

88. Hoendermis ES, Liu LC, Hummel YM, van der Meer P, de Boer RA, Berger RM, van Veldhuisen DJ and Voors AA. Effects of sildenafil on invasive haemodynamics and exercise capacity in heart failure patients with preserved ejection fraction and pulmonary hypertension: a randomized controlled trial. *European heart journal*. 2015:ehv336.

89. Heineke J, Auger-Messier M, Xu J, Oka T, Sargent MA, York A, Klevitsky R, Vaikunth S, Duncan SA, Aronow BJ, Robbins J, Crombleholme TM and Molkentin JD. Cardiomyocyte GATA4 functions as a stress-responsive regulator of angiogenesis in the murine heart. *J Clin Invest*. 2007;117:3198-210.

90. Su T, Zhang T, Xie S, Yan J, Wu Y, Li X, Huang L and Luo H-B. Discovery of novel PDE9 inhibitors capable of inhibiting Aβ aggregation as potential candidates for the treatment of Alzheimer's disease. *Scientific Reports*. 2016;6:21826.

91. Heckman PRA, Wouters C and Prickaerts J. Phosphodiesterase Inhibitors as a Target for Cognition Enhancement in Aging and Alzheimer's Disease: A Translational Overview. *Current pharmaceutical design*. 2015;21:317-331.

92. Reneerkens OA, Rutten K, Steinbusch HW, Blokland A and Prickaerts J. Selective phosphodiesterase inhibitors: a promising target for cognition enhancement. *Psychopharmacology (Berl)*. 2009;202:419-43.

93. Hutson PH, Finger EN, Magliaro BC, Smith SM, Converso A, Sanderson PE, Mullins D, Hyde LA, Eschle BK, Turnbull Z, Sloan H, Guzzi M, Zhang X, Wang A,

Rindgen D, Mazzola R, Vivian JA, Eddins D, Uslaner JM, Bednar R, Gambone C, Le-Mair W, Marino MJ, Sachs N, Xu G and Parmentier-Batteur S. The selective phosphodiesterase 9 (PDE9) inhibitor PF-04447943 (6-[(3S,4S)-4-methyl-1-(pyrimidin-2-ylmethyl)pyrrolidin-3-yl]-1-(tetrahydro-2H-pyran-4-yl)-1,5-dihydro-4H-pyrazolo[3,4-d]pyrimidin-4-one) enhances synaptic plasticity and cognitive function in rodents. *Neuropharmacology*. 2011;61:665-676.

94. Vardigan JD, Converso A, Hutson PH and Uslaner JM. The Selective Phosphodiesterase 9 (PDE9) Inhibitor PF-04447943 Attenuates a Scopolamine-Induced Deficit in a Novel Rodent Attention Task. *Journal of Neurogenetics*. 2011;25:120-126.

95. Frolich L, Wunderlich G, Thamer C, Roehrle M, Garcia M, Jr. and Dubois B. Evaluation of the efficacy, safety and tolerability of orally administered BI 409306, a novel phosphodiesterase type 9 inhibitor, in two randomised controlled phase II studies in patients with prodromal and mild Alzheimer's disease. *Alzheimers Res Ther*. 2019;11:18.

96. McMurray JJ, Packer M, Desai AS, Gong J, Lefkowitz MP, Rizkala AR, Rouleau JL, Shi VC, Solomon SD, Swedberg K, Zile MR, Investigators P-H and Committees. Angiotensin-neprilysin inhibition versus enalapril in heart failure. *N Engl J Med*. 2014;371:993-1004.

97. Fawcett L, Baxendale R, Stacey P, McGrouther C, Harrow I, Soderling S, Hetman J, Beavo JA and Phillips SC. Molecular cloning and characterization of a distinct human phosphodiesterase gene family: PDE11A. *Proc Natl Acad Sci U S A*. 2000;97:3702-7.

98. Ha M and Kim VN. Regulation of microRNA biogenesis. *Nat Rev Mol Cell Biol*. 2014;15:509-24.

99. Olson EN. MicroRNAs as therapeutic targets and biomarkers of cardiovascular disease. *Science translational medicine*. 2014;6:239ps3.

100. Shah R, Ziegler O, Yeri A, Liu X, Murthy V, Rabideau D, Xiao CY, Hanspers K, Belcher A, Tackett M, Rosenzweig A, Pico AR, Januzzi JL and Das S. MicroRNAs Associated With Reverse Left Ventricular Remodeling in Humans Identify Pathways of Heart Failure Progression. *Circ Heart Fail.* 2018;11:e004278.

101. Castro-Villegas C, Perez-Sanchez C, Escudero A, Filipescu I, Verdu M, Ruiz-Limon P, Aguirre MA, Jimenez-Gomez Y, Font P, Rodriguez-Ariza A, Peinado JR, Collantes-Estevez E, Gonzalez-Conejero R, Martinez C, Barbarroja N and Lopez-Pedrera C. Circulating miRNAs as potential biomarkers of therapy effectiveness in rheumatoid arthritis patients treated with anti-TNFalpha. *Arthritis research & therapy.* 2015;17:49.

102. Lopez JP, Kos A and Turecki G. Major depression and its treatment: microRNAs as peripheral biomarkers of diagnosis and treatment response. *Current opinion in psychiatry.* 2018;31:7-16.

103. Dangwal S, Schimmel K, Foinquinos A, Xiao K and Thum T. Noncoding RNAs in Heart Failure. *Handbook of experimental pharmacology.* 2017;243:423-445.

104. van Rooij E, Sutherland LB, Qi X, Richardson JA, Hill J and Olson EN. Control of stress-dependent cardiac growth and gene expression by a microRNA. *Science.* 2007;316:575-9.

105. van Rooij E, Sutherland LB, Liu N, Williams AH, McAnally J, Gerard RD, Richardson JA and Olson EN. A signature pattern of stress-responsive microRNAs that can evoke cardiac hypertrophy and heart failure. *Proc Natl Acad Sci U S A.* 2006;103:18255-60.

106. Care A, Catalucci D, Felicetti F, Bonci D, Addario A, Gallo P, Bang ML, Segnalini P, Gu Y, Dalton ND, Elia L, Latronico MV, Hoydal M, Autore C, Russo MA, Dorn GW, 2nd, Ellingsen O, Ruiz-Lozano P, Peterson KL, Croce CM, Peschle C and Condorelli G. MicroRNA-133 controls cardiac hypertrophy. *Nat Med.* 2007;13:613-8.

107. Karakikes I, Chaanine AH, Kang S, Mukete BN, Jeong D, Zhang S, Hajjar RJ and Lebeche D. Therapeutic cardiac-targeted delivery of miR-1 reverses pressure overload-induced cardiac hypertrophy and attenuates pathological remodeling. *J Am Heart Assoc.* 2013;2:e000078.

108. Ucar A, Gupta SK, Fiedler J, Erikci E, Kardasinski M, Batkai S, Dangwal S, Kumarswamy R, Bang C, Holzmann A, Remke J, Caprio M, Jentzsch C, Engelhardt S, Geisendorf S, Glas C, Hofmann TG, Nessling M, Richter K, Schiffer M, Carrier L, Napp LC, Bauersachs J, Chowdhury K and Thum T. The miRNA-212/132 family regulates both cardiac hypertrophy and cardiomyocyte autophagy. *Nat Commun.* 2012;3:1078.

109. Montgomery RL, Hullinger TG, Semus HM, Dickinson BA, Seto AG, Lynch JM, Stack C, Latimer PA, Olson EN and van Rooij E. Therapeutic inhibition of miR-208a improves cardiac function and survival during heart failure. *Circulation.* 2011;124:1537-47.

110. Vegter EL, van der Meer P, de Windt LJ, Pinto YM and Voors AA. MicroRNAs in heart failure: from biomarker to target for therapy. *Eur J Heart Fail.* 2016;18:457-68.

111. Wong LL, Wang J, Liew OW, Richards AM and Chen YT. MicroRNA and Heart Failure. *Int J Mol Sci.* 2016;17:502.

112. Marfella R, Di Filippo C, Potenza N, Sardu C, Rizzo MR, Siniscalchi M, Musacchio E, Barbieri M, Mauro C, Mosca N, Solimene F, Mottola MT, Russo A, Rossi F, Paolisso G and D'Amico M. Circulating microRNA changes in heart failure patients treated with cardiac resynchronization therapy: responders vs. non-responders. *Eur J Heart Fail.* 2013;15:1277-88.

113. Sucharov CC, Kao DP, Port JD, Karimpour-Fard A, Quaife RA, Minobe W, Nunley K, Lowes BD, Gilbert EM and Bristow MR. Myocardial microRNAs associated with reverse remodeling in human heart failure. *JCI Insight.* 2017;2:e89169.

114. Lee DI, Zhu G, Sasaki T, Cho GS, Hamdani N, Holewinski R, Jo SH, Danner T, Zhang M, Rainer PP, Bedja D, Kirk JA, Ranek MJ, Dostmann WR, Kwon C, Margulies KB, Van Eyk JE, Paulus WJ, Takimoto E and Kass DA. Phosphodiesterase 9A controls nitric-oxide-independent cGMP and hypertrophic heart disease. *Nature*. 2015;519:472-6.

115. Kishimoto I, Rossi K and Garbers DL. A genetic model provides evidence that the receptor for atrial natriuretic peptide (guanylyl cyclase-A) inhibits cardiac ventricular myocyte hypertrophy. *Proc Natl Acad Sci U S A*. 2001;98:2703-6.

116. Baras AS, Mitchell CJ, Myers JR, Gupta S, Weng LC, Ashton JM, Cornish TC, Pandey A and Halushka MK. miRge - A Multiplexed Method of Processing Small RNA-Seq Data to Determine MicroRNA Entropy. *PLoS One*. 2015;10:e0143066.

117. Anders S and Huber W. Differential expression analysis for sequence count data. *Genome Biol*. 2010;11:R106.

118. Fromm B, Billipp T, Peck LE, Johansen M, Tarver JE, King BL, Newcomb JM, Sempere LF, Flatmark K, Hovig E and Peterson KJ. A Uniform System for the Annotation of Vertebrate microRNA Genes and the Evolution of the Human microRNAome. *Annu Rev Genet*. 2015;49:213-42.

119. Edgar R, Domrachev M and Lash AE. Gene Expression Omnibus: NCBI gene expression and hybridization array data repository. *Nucleic Acids Res*. 2002;30:207-10.

120. Kim D, Langmead B and Salzberg SL. HISAT: a fast spliced aligner with low memory requirements. *Nat Methods*. 2015;12:357-60.

121. Li B and Dewey CN. RSEM: accurate transcript quantification from RNA-Seq data with or without a reference genome. *BMC Bioinformatics*. 2011;12:323.

122. Love MI, Huber W and Anders S. Moderated estimation of fold change and dispersion for RNA-seq data with DESeq2. *Genome Biol*. 2014;15:550.

123. KEGG.db: A set of annotation maps for KEGG [computer program]. Version R package version 3.2.3; 2016.

124. Shen J and Hung MC. Signaling-mediated regulation of MicroRNA processing. *Cancer research*. 2015;75:783-91.

125. Sempere LF, Freemantle S, Pitha-Rowe I, Moss E, Dmitrovsky E and Ambros V. Expression profiling of mammalian microRNAs uncovers a subset of brain-expressed microRNAs with possible roles in murine and human neuronal differentiation. *Genome Biol*. 2004;5:R13.

126. Laine SK, Alm JJ, Virtanen SP, Aro HT and Laitala-Leinonen TK. MicroRNAs miR-96, miR-124, and miR-199a regulate gene expression in human bone marrow-derived mesenchymal stem cells. *J Cell Biochem*. 2012;113:2687-95.

127. Nakamura T, Zhu G, Ranek MJ, Kokkonen-Simon K, Zhang M, Kim GE, Tsujita K and Kass DA. Prevention of PKG-1alpha Oxidation Suppresses Antihypertrophic/Antifibrotic Effects From PDE5 Inhibition but not sGC Stimulation. *Circ Heart Fail*. 2018;11:e004740.

128. Li Q, Song XW, Zou J, Wang GK, Kremneva E, Li XQ, Zhu N, Sun T, Lappalainen P, Yuan WJ, Qin YW and Jing Q. Attenuation of microRNA-1 derepresses the cytoskeleton regulatory protein twinfilin-1 to provoke cardiac hypertrophy. *J Cell Sci*. 2010;123:2444-52.

129. Li R, Yan G, Zhang Q, Jiang Y, Sun H, Hu Y, Sun J and Xu B. miR-145 inhibits isoproterenol-induced cardiomyocyte hypertrophy by targeting the expression and localization of GATA6. *FEBS Lett*. 2013;587:1754-61.

130. Li Z, Song Y, Liu L, Hou N, An X, Zhan D, Li Y, Zhou L, Li P, Yu L, Xia J, Zhang Y, Wang J and Yang X. miR-199a impairs autophagy and induces cardiac hypertrophy through mTOR activation. *Cell Death Differ*. 2017;24:1205-1213.

131. Wei L, Yuan M, Zhou R, Bai Q, Zhang W, Zhang M, Huang Y and Shi L. MicroRNA-101 inhibits rat cardiac hypertrophy by targeting Rab1a. *J Cardiovasc Pharmacol.* 2015;65:357-63.

132. Callis TE, Pandya K, Seok HY, Tang RH, Tatsuguchi M, Huang ZP, Chen JF, Deng Z, Gunn B, Shumate J, Willis MS, Selzman CH and Wang DZ. MicroRNA-208a is a regulator of cardiac hypertrophy and conduction in mice. *J Clin Invest.* 2009;119:2772-86.

133. Cheng Y and Zhang C. MicroRNA-21 in cardiovascular disease. *J Cardiovasc Transl Res.* 2010;3:251-5.

134. Han M, Yang Z, Sayed D, He M, Gao S, Lin L, Yoon S and Abdellatif M. GATA4 expression is primarily regulated via a miR-26b-dependent post-transcriptional mechanism during cardiac hypertrophy. *Cardiovasc Res.* 2012;93:645-54.

135. Wang J, Song Y, Zhang Y, Xiao H, Sun Q, Hou N, Guo S, Wang Y, Fan K, Zhan D, Zha L, Cao Y, Li Z, Cheng X, Zhang Y and Yang X. Cardiomyocyte overexpression of miR-27b induces cardiac hypertrophy and dysfunction in mice. *Cell Res.* 2012;22:516-27.

136. Yang T, Zhang GF, Chen XF, Gu HH, Fu SZ, Xu HF, Feng Q and Ni YM. MicroRNA-214 provokes cardiac hypertrophy via repression of EZH2. *Biochem Biophys Res Commun.* 2013;436:578-84.

137. Bernardo BC, Gao XM, Winbanks CE, Boey EJ, Tham YK, Kiriazis H, Gregorevic P, Obad S, Kauppinen S, Du XJ, Lin RC and McMullen JR. Therapeutic inhibition of the miR-34 family attenuates pathological cardiac remodeling and improves heart function. *Proc Natl Acad Sci U S A.* 2012;109:17615-20.

138. He J, Jiang S, Li FL, Zhao XJ, Chu EF, Sun MN, Chen MZ and Li H. MicroRNA-30b-5p is involved in the regulation of cardiac hypertrophy by targeting CaMKIIdelta. *Journal*

of investigative medicine : the official publication of the American Federation for Clinical Research. 2013;61:604-12.

139. Song L, Su M, Wang S, Zou Y, Wang X, Wang Y, Cui H, Zhao P, Hui R and Wang J. MiR-451 is decreased in hypertrophic cardiomyopathy and regulates autophagy by targeting TSC1. *J Cell Mol Med*. 2014;18:2266-74.

140. Lin CS, Lin G, Xin ZC and Lue TF. Expression, distribution and regulation of phosphodiesterase 5. *Curr Pharm Des*. 2006;12:3439-57.

141. Williams AE, Perry MM, Moschos SA and Lindsay MA. microRNA expression in the aging mouse lung. *BMC Genomics*. 2007;8:172.

142. Gao F, Liu P, Narayanan J, Yang M, Fish BL, Liu Y, Liang M, Jacobs ER and Medhora M. Changes in miRNA in the lung and whole blood after whole thorax irradiation in rats. *Sci Rep*. 2017;7:44132.

143. Davis J, Burr AR, Davis GF, Birnbaumer L and Molkentin JD. A TRPC6-dependent pathway for myofibroblast transdifferentiation and wound healing in vivo. *Dev Cell*. 2012;23:705-15.

144. Zhang Q, Wang G, Yuan W, Wu J, Wang M and Li C. The effects of phosphodiesterase-5 inhibitor sildenafil against post-resuscitation myocardial and intestinal microcirculatory dysfunction by attenuating apoptosis and regulating microRNAs expression: essential role of nitric oxide syntheses signaling. *J Transl Med*. 2015;13:177.

145. Fiore D, Gianfrilli D, Giannetta E, Galea N, Panio G, di Dato C, Pofi R, Pozza C, Sbardella E, Carbone I, Naro F, Lenzi A, Venneri MA and Isidori AM. PDE5 Inhibition Ameliorates Visceral Adiposity Targeting the miR-22/SIRT1 Pathway: Evidence From the CECSID Trial. *J Clin Endocrinol Metab*. 2016;101:1525-34.

146. Kokkonen K and Kass DA. Nanodomain Regulation of Cardiac Cyclic Nucleotide Signaling by Phosphodiesterases. *Annu Rev Pharmacol Toxicol.* 2017;57:455-479.

147. Golden RJ, Chen B, Li T, Braun J, Manjunath H, Chen X, Wu J, Schmid V, Chang TC, Kopp F, Ramirez-Martinez A, Tagliabracci VS, Chen ZJ, Xie Y and Mendell JT. An Argonaute phosphorylation cycle promotes microRNA-mediated silencing. *Nature.* 2017;542:197-202.

148. Kokkonen-Simon KM, Saberi A, Nakamura T, Ranek MJ, Zhu G, Bedja D, Kuhn M, Halushka MK, Lee DI and Kass DA. Marked disparity of microRNA modulation by cGMP-selective PDE5 versus PDE9 inhibitors in heart disease. *JCI Insight.* 2018;3.

149. Hashimoto T, Kim GE, Tunin RS, Adesiyun T, Hsu S, Nakagawa R, Zhu G, O'Brien JJ, Hendrick JP, Davis RE, Yao W, Beard D, Hoxie HR, Wennogle LP, Lee DI and Kass DA. Acute Enhancement of Cardiac Function by Phosphodiesterase Type 1 Inhibition. *Circulation.* 2018;138:1974-1987.

150. Wessel D and Flugge UI. A method for the quantitative recovery of protein in dilute solution in the presence of detergents and lipids. *Anal Biochem.* 1984;138:141-3.

151. Herbrich SM, Cole RN, West KP, Jr., Schulze K, Yager JD, Groopman JD, Christian P, Wu L, O'Meally RN, May DH, McIntosh MW and Ruczinski I. Statistical inference from multiple iTRAQ experiments without using common reference standards. *J Proteome Res.* 2013;12:594-604.

152. Foster DB, Liu T, Kammers K, O'Meally R, Yang N, Papanicolaou KN, Talbot CC, Jr., Cole RN and O'Rourke B. Integrated Omic Analysis of a Guinea Pig Model of Heart Failure and Sudden Cardiac Death. *J Proteome Res.* 2016;15:3009-28.

153. Smyth GK. Linear models and empirical bayes methods for assessing differential expression in microarray experiments. *Stat Appl Genet Mol Biol.* 2004;3:Article3.

154. Kammers K, Cole RN, Tiengwe C and Ruczinski I. Detecting Significant Changes in Protein Abundance. *EuPA Open Proteom*. 2015;7:11-19.

155. Benjamini Y and Hochberg Y. Controlling the False Discovery Rate: A Practical and Powerful Approach to Multiple Testing. *Journal of the Royal Statistical Society Series B (Methodological)*. 1995;57:289-300.

156. Huang da W, Sherman BT and Lempicki RA. Systematic and integrative analysis of large gene lists using DAVID bioinformatics resources. *Nat Protoc*. 2009;4:44-57.

157. Kimura H and Murad F. Evidence for two different forms of guanylate cyclase in rat heart. *J Biol Chem*. 1974;249:6910-6.

158. Seya K, Motomura S and Furukawa K. Cardiac mitochondrial cGMP stimulates cytochrome c release. *Clin Sci (Lond)*. 2007;112:113-21.

159. Mitsuishi M, Miyashita K and Itoh H. cGMP rescues mitochondrial dysfunction induced by glucose and insulin in myocytes. *Biochem Biophys Res Commun*. 2008;367:840-5.

160. Nisoli E, Falcone S, Tonello C, Cozzi V, Palomba L, Fiorani M, Pisconti A, Brunelli S, Cardile A, Francolini M, Cantoni O, Carruba MO, Moncada S and Clementi E. Mitochondrial biogenesis by NO yields functionally active mitochondria in mammals. *Proc Natl Acad Sci U S A*. 2004;101:16507-12.

161. Seya K, Ono K, Fujisawa S, Okumura K, Motomura S and Furukawa K. Cytosolic Ca2+-induced apoptosis in rat cardiomyocytes via mitochondrial NO-cGMP-protein kinase G pathway. *J Pharmacol Exp Ther*. 2013;344:77-84.

162. Sun Y, Deng T, Lu N, Yan M and Zheng X. B-type natriuretic peptide protects cardiomyocytes at reperfusion via mitochondrial calcium uniporter. *Biomed Pharmacother*. 2010;64:170-6.

163. Murakami W, Kobayashi S, Susa T, Nanno T, Ishiguchi H, Myoren T, Nishimura S, Kato T, Hino A, Oda T, Okuda S, Yamamoto T and Yano M. Recombinant Atrial Natriuretic Peptide Prevents Aberrant Ca2+ Leakage through the Ryanodine Receptor by Suppressing Mitochondrial Reactive Oxygen Species Production Induced by Isoproterenol in Failing Cardiomyocytes. *PLoS One*. 2016;11:e0163250.

164. Hong L, Xi J, Zhang Y, Tian W, Xu J, Cui X and Xu Z. Atrial natriuretic peptide prevents the mitochondrial permeability transition pore opening by inactivating glycogen synthase kinase 3beta via PKG and PI3K in cardiac H9c2 cells. *Eur J Pharmacol*. 2012;695:13-9.

165. Martell JD, Deerinck TJ, Sancak Y, Poulos TL, Mootha VK, Sosinsky GE, Ellisman MH and Ting AY. Engineered ascorbate peroxidase as a genetically encoded reporter for electron microscopy. *Nature biotechnology*. 2012;30:1143-1148.

166. Lam SS, Martell JD, Kamer KJ, Deerinck TJ, Ellisman MH, Mootha VK and Ting AY. Directed evolution of APEX2 for electron microscopy and proximity labeling. *Nature methods*. 2015;12:51-54.

167. Hung V, Udeshi ND, Lam SS, Loh KH, Cox KJ, Pedram K, Carr SA and Ting AY. Spatially resolved proteomic mapping in living cells with the engineered peroxidase APEX2. *Nat Protoc*. 2016;11:456-75.

168. Bienert GP, Schjoerring JK and Jahn TP. Membrane transport of hydrogen peroxide. *Biochim Biophys Acta*. 2006;1758:994-1003.

CURRICULUM VITAE

Kristen Kokkonen-Simon

720 Rutland Ave, Ross 858 • Baltimore, MD 21205 • kkokkon1@jhmi.edu • (719) 648-4432

Birth Date: April 22, 1991
Birth Place: San Jose, CA

EDUCATION

Johns Hopkins University Baltimore, MD
PhD, Cellular and Molecular Medicine May 2019

University of Colorado Boulder, CO
BA, Molecular, Cellular and Developmental Biology; Biochemistry May 2013
GPA: 3.91; Honors: summa cum laude

RESEARCH EXPERIENCE

Johns Hopkins University Baltimore, MD
Graduate student with Dr. David Kass August 2013 – Present

University of Colorado Boulder, CO
Undergraduate research assistant with Dr. Leslie Leinwand January 2011 – July 2013

TEACHING EXPERIENCE

Johns Hopkins University Baltimore, MD
Pollard Scholar for Graduate Student Genetics Course October 2014 – December 2014

University of Colorado Boulder, CO
Teaching Assistant, Molecular, Cellular and Developmental Biology August 2012 – December 2012

University of Colorado Boulder, CO
Learning Assistant, General Chemistry August 2010 – December 2010

GRANTS AND AWARDS

Ruth L. Kirschstein Pre-Doctoral National Research Service Award August 2016 - Present
National Heart, Lung, and Blood Institute, National Institutes of Health
Grant F31HL134196; total amount of $130,728

Keystone Symposia Future of Science Fund Scholarship January 2018
Travel Award from Keystone Symposia on Molecular and Cellular Biology

PUBLICATIONS

1. Ranek MJ, **Kokkonen-Simon KM**, Holewinski RJ, Lee DI, Chen A, Pinilla Vera M, Dunkerly-Eyring B, Patel C, Nakamura T, Zhu G, Bedja D, Sasaki M, Van Eyk JE, Powell JD, Kass DA (2019) PKG-Modified TSC2 Regulates mTORC1 Activity to Counter Adverse Cardiac Stress. Nature. 566(7743):264-269.
2. Zhang QJ, Tran TA, Wang M, Ranek MJ, **Kokkonen-Simon KM**, Gao J, Luo X, Tan W, Kyrychenko V, Liao L, Xu J (2018) Histone lysine dimethyl-demethylase KDM3A controls pathological cardiac hypertrophy and fibrosis. Nature Communications. 9(1):5230.
3. **Kokkonen-Simon KM**, Saberi A, Nakamura T, Ranek MJ, Zhu G, Bedja D, Kuhn M, Halushka MK, Lee DI, Kass DA (2018) Marked Disparity of microRNA Regulation by cGMP-selective PDE5 versus PDE9 Inhibitors in Heart Disease. JCI Insight. 3(15).
4. Hsu S, **Kokkonen-Simon KM**, Kirk JA, Kolb TM, Damico RL, Mathai SC, Mukherjee M, Shah AA, Wigley FM, Margulies KB, Hassoun PM (2018) Right Ventricular Myofilament Functional Differences in Humans With Systemic Sclerosis–Associated Versus Idiopathic Pulmonary Arterial Hypertension. Circulation. 137(22):2360-70.
5. Nakamura T, Zhu G, Ranek MJ, **Kokkonen-Simon K**, Zhang M, Kim GE, Tsujita K, Kass DA (2018) Prevention of PKG-1α Oxidation Suppresses Antihypertrophic/Antifibrotic Effects From PDE5 Inhibition but not sGC Stimulation. Circulation: Heart Failure. 11(3):e004740.
6. **Kokkonen K**, Kass DA (2017) Nanodomain Regulation of Cardiac Cyclic Nucleotide Signaling by Phosphodiesterases. Annual Review of Pharmacology and Toxicology. 57:455-79.

ABSTRACTS

1. **KM Kokkonen-Simon**, GE Kim, DB Foster, and DA Kass (2018) PDE5 and PDE9 Compartmentalization in Cardiac Myocytes. Abstracts of the Gordon Conference on Cyclic Nucleotide Phosphodiesterases.
2. **KM Kokkonen-Simon**, DI Lee, T Nakamura, G Zhu, D Bedja, and DA Kass. PDE5 and PDE9 inhibition differentially regulate microRNA expression during pressure-overload-induced heart failure (2018) Abstracts of the Keystone Symposia on Heart Failure: Crossing the Translational Divide.
3. MJ Ranek, **KM Kokkonen**, DI Lee, RJ Holewinski, V Agrawal, C Virus, DA Stevens, M Sasaki, H Zhang, MM Mannion, PP Rainer, RC Page, JC Schisler, JE Van Eyk, MS Willis, and DA Kass (2017) Novel Role of PKG in Protein Quality Control by Regulating Chip. Abstracts of 8th International Conference on cGMP Generators, Effectors and Therapeutic Implications.
4. MJ Ranek, **KM Kokkonen**, RJ Holewinski, DI Lee, T Nakamura, G Zhu, M Sasaki, JE Van Eyk, and DA Kass (2016) Protein Kinase G is a Redox Sensor that Controls Autophagic Flux by Phosphorylating Tuberin. Abstracts of the American Heart Association Scientific Sessions.

PATENTS

1. DA Kass, MJ Ranek, KM Kokkonen, JD Powell, C Patel. Engineered TSC2. US Appl. No.: 62/532,909. Filed 2017.
2. DA Kass, B Dunkerly-Eyring, KM Kokkonen, MJ Ranek. Targeting TSC2 S1366 (mouse, rat) S1365 (human) by gene engineering or phosphorylation to regulate mTOR signaling cascades for therapeutic indications. Filed 2018.